Growth and Characterisation of (In)GaAsN Alloys for Optoelectronic Applications

Qiang Gao

A thesis submitted for the degree of

Doctor of Philosophy

of

The Australian National University

April 2004

CERTIFICATE

This thesis, to the best of my knowledge and belief, does not contain any results previously published by another person or submitted for a degree or diploma at any university except where due reference is made in the text.

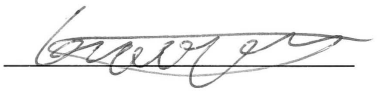

Qiang Gao

To my parents and my brothers

Acknowledgements

I would like to express my sincere appreciation and gratitude to my supervisors, Prof. Chennupati Jagadish and Dr. Hark Hoe Tan for their invaluable guidance and continuous support. They have been a constant source of inspiration. Their expertise, patience and encouragement have guided me through the ups and downs of my PhD work. Sincere thanks are also due to my advisor, Dr. Jennifer Wong-Leung, for her continuous support.

Many thanks to Dr. Manuela Buda for her unreserved help on the processing of my laser devices, and for many insightful talks leading me to understand the physics behind my experimental results. Without her guidance and participation, there would not be Chapter 7.

Sincere thanks to Dr. Lan Fu for her continuous support, in particular, for introducing me to many techniques at the early stage of my PhD project and for many fruitful discussions.

Special thanks to Dr. Sanju Deenapanray for his support and enthusiastic contributions to my understanding of defects and implantation-induced electrical isolation in semiconductors.

I would like to extend my sincere thanks to Prof. Mike Gal for fruitful discussions and granting me access to his laboratory at the School of Physics, University of New South Wales, for photoluminescence measurements. Special appreciation to Dr. Baoquan Sun (currently at Institute of Semiconductors, P. R. China) for his continuous help and assistance in the optical measurements, and the insightful understanding of optical properties in the semiconductor materials.

Special appreciation is due to Dr. Jin Zou (currently at the University of Queensland) and Dr. Liuzhang Ouyang (currently at South China University of Technology) at the Australian Key Centre for Microscopy and Microanalysis, the University of Sydney, for the Transmission Electron Microscopy (TEM) analysis on a number of my samples. Without their work, all the TEM images would not be available.

I am also grateful to Prof. Bengt Svensson for inviting and hosting me to visit his laboratory at the Royal Institute of Technology, Sweden. My appreciation is also ex-

tended to Prof. Henri Boudinov at Instituto de Fisica, Brazil, for his help on Hall measurements.

Grateful acknowledgement is due to Mr. Michael Aggett for his constant assistance in the MOCVD growth and for his extensive maintenance of the MOCVD reactors and other equipment.

Many thanks to Dr. Mladen Petravic for SIMS measurements, Dr. John Kennedy for PIXE measurements. Special thanks to Ms. Laura Walmsley and Ms Renee Vercoe for their efficient and pleasant administrative support.

I would also like to thank all the staff and fellow students at EME for providing a friendly and supportive working environment : Prof. Jim Williams, Prof. Rob Elliman, Dr. Mark Ridgway, Dr. Ying Chen, Prof. Neville Fletcher, Dr. Jodie Bradby, Dr. Craig Johnson, Dr. Stephanie Cheylan, Dr. Sergei Kucheyev, Dr. Annette Dowd, Dr. Tessica Weijers, Dr. Gustavo Azevedo, Dr. Chris Glover, Dr. Patrick Kluth, Dr. Susan Kluth, Tom Halstead, Alan Hayes, Tony Watt, David Llewellyn, Bernie King, Fred Johnson, Martin Conway, Bettina Wolpensinger, Penny Lever, Jillian Hay, Kallista Stewart, Victoria Coleman, Michael Fraser, Paulus Gareso, Suhda Mokkapati, Satyanarayan Barik, Marc Spencer, Nat Smith, David Brett, Andrew Wilkinson, Ali Khalil, Bernt Johannessen, Zohair Hussain, and Jun Yu.

The financial assistance provided by the Commonwealth Department of Education, Science and Training and the Australian National University is acknowledged.

This thesis is dedicated to my parents and my brothers, for their love, understanding and unquestioned support.

Finally I thank my girl friend, Yue Zhao, whose love and encouragement were so important throughout the duration of my PhD project.

Abstract

Incorporation of a few percent of N in GaAs or InGaAs surprisingly causes a huge negative bowing parameter and significantly decreases the bandgap, which makes InGaAsN a very promising candidate for long-wavelength optoelectronic devices for optical-fibre communication applications. However, a successful application of (In)GaAsN alloy system depends on many aspects, such as an understanding of fundamental properties, materials growth, and materials and device processing techniques. Hence, this thesis focuses on the epitaxial growth, optical and electrical properties, ion implantation, intermixing, and laser-device processing and characterisation.

Epitaxial growth is the first crucial step for all heterostructure semiconductor devices, which forms the first part of this work. Growth parameters of (In)GaAsN materials were carefully studied, in particular the parameters affecting the N incorporation in GaAsN. Growth temperature and fractional dimethylhydrazine (DMHy) molar flow in total group-V molar flow were identified as two most important factors controlling the N composition. To explain the GaAsN growth process, a kinetic growth model was proposed. It was also found that growing GaAsN directly on AlGaAs has a negative effect on the crystalline quality of the GaAsN layer. To compensate the large strain between the GaAsN quantum well (QW) and GaAs barriers, a new structure containing strain-compensating InAs monolayers was proposed and was found to significantly improve the PL properties. By choosing appropriate growth parameters, the high quality InGaAsN quantum dots (QDs) with 1.3 μm photoluminescence (PL) emission at RT were grown on the GaAs substrate.

Fundamental properties of GaAsN alloy system were then investigated, and some novel aspects of this system were also explored. The low-temperature (10 K) radiative recombination in GaAsN was found to be related to the localised electrons and the delocalised holes. The temperature dependence of PL spectra confirmed a N-composition dependent conduction-band structure for GaAsN alloys. Microstructural studies found micro-cracks and high density of dislocations in GaAsN epilayers when their thicknesses were beyond critical thickness. However, these facts do not necessarily cause a poor optical property. Surprisingly random lasing emissions were discovered from these GaAsN layers with such defects at low temperatures.

As an important step in the fabrication of various electrical and optical semiconductor devices, ion implantation was used in this work to study the damage buildup and electrical isolation processes of GaAsN epilayers. It was found that with increasing N content, the GaAsN epilayer becomes easier to amorphise at the liquid N_2 temperature, presumably due to the defect accumulation in the strain field caused by N atoms. However, increasing N content did not change the threshold fluence for electrical isolation in *p*-GaAsN layers if these layers had the same free hole concentration. The threshold fluence was found to depend almost linearly on the initial free carrier concentration and inversely on the density of displacements produced by the ion beam. As a critical parameter in device applications, the thermal stability of the implantation-induced electrical isolation is another important part of this study. It was found that the thermal stability primarily depends on the ratio of total ion fluence to the threshold fluence.

Another part of this work involved InGaAsN QD intermixing and laser devices. Large thermal interdiffusion in the QD structure has been efficiently suppressed by deposition of a thin TiO_2 film on the sample's surface. On the other hand, the interdiffusion can also be enhanced by deposition of a SiO_2 film with a high temperature annealing. Finally, a thin *p*-cladding layer InGaAsN QD laser structure was designed and fabricated into ridge-waveguide laser devices. The final laser devices were systematically characterised and compared with a reference InGaAs QW laser device. The QD transitions were probed in the absorption and electroluminescence spectra. It was evident that in the QD structure, transitions from the excited states were responsible for lasing emissions.

This work has covered a wide range of research related to (In)GaAsN semiconductor alloys. It has expanded our knowledge of this novel material system and demonstrated the InGaAsN QD laser devices, which may have a great significance in the fundamental studies and practical applications.

Contents

Publications related to this thesis

Journals

1. Q. Gao, H. H. Tan, C. Jagadish, B. Q. Sun, M. Gal, L. Ouyang, J. Zou, "*Enhanced optical properties of GaAsN/GaAs quantum-well structure by the insertion of InAs monolayers*", Appl. Phys. Lett. **84** (14): 2536-2538, 2004.

2. Q. Gao, H. H. Tan, C. Jagadish, B. Q. Sun, M. Gal, L. Ouyang, J. Zou, "*Metalorganic chemical vapor deposition of GaAsN epilayers: microstructures and optical properties*", J. Cryst. Growth **264** (1-3): 92–97, 2004.

3. Q. Gao, P. N. K. Deenapanray, H. H. Tan, C. Jagadish, "*Implantation-induced electrical isolation of GaAsN epilayers grown by metalorganic chemical vapour deposition*", Appl. Phys. Lett. **83** (16): 3386-3388, 2003.

4. Q. Gao, H. H. Tan, C. Jagadish, P. N. K. Deenapanray, "*Defect evolution in annealed p-type GaAsN epilayers grown by metalorganic chemical vapour deposition*", Jpn. J. Appl. Phys., Part 1 **42** (11), 6827-3832, 2003.

5. P. N. K. Deenapanray, Q. Gao, C. Jagadish, "Implant isolation of Zn-doped GaAs epilayers: effects of ion species, doping concentration, and implantation temperature", J. Appl. Phys. **93** (11): 9123-9129, 2003.

6. B. Q. Sun, M. Gal, Q. Gao, H. H. Tan, C. Jagadish, T. Puzzer, L. Ouyang, J. Zou, "*Epitaxially grown GaAsN random laser*", J. Appl. Phys. **93** (10): 5855-5858, 2003.

7. B. Q. Sun, M. Gal, Q. Gao, H. H. Tan, C. Jagadish, "*On the nature of radiative recombination in GaAsN*", Appl. Phys. Lett. **81** (23): 4368-4370, 2002.

8. Q. Gao, H. H. Tan, L. Fu, C. Jagadish, "*Effects of thermal stress on interdiffusion in InGaAsN/GaAs quantum dots*", submitted to Appl. Phys. Lett. (#L04-0017), 2004. (recommended for publication with two minor corrections in reviewer's report).

Conference proceedings

1. Q. Gao, J. Muller, P. N. K. Deenapanray, H. H. Tan, C. Jagadish, "*Electrical isolation of p-type GaAsN epitaxial layers by ion irradiation*", oral presentation, Proceedings of MRS (Materials Research Society) Fall meeting, Boston, USA, Vol. **744**: 659-664, Dec. 2002.

2. Q. Gao, H. H. Tan, C. Jagadish, B. Q. Sun, M. Gal, L. Ouyang, J. Zou, "*Growth and characterization of GaAsN epilayer and (In)GaAsN quantum-well structures*", oral presentation, Proceedings of Conference on Optoelectronic and Microelectronic Materials & Devices (Sydney), IEEE Publishing Co., Piscataway, NJ, USA, 247-250, Dec. 2002.

3. B. Q. Sun, M. Gal, Q. Gao, H. H. Tan, C. Jagadish, "*Properties of radiative recombination in GaAsN epilayers*", poster, Proceedings of Conference on Optoelectronic and Microelectronic Materials & Devices (Sydney), IEEE Publishing Co., Piscataway, NJ, USA, 483-486, Dec. 2002.

4. Q. Gao, P. N. K. Deenapanray, H. H. Tan, C. Jagadish, " Influence of *isochronal annealing on the evolution of hole traps in GaAsN epilayers grown by metalorganic chemical vapor deposition* ", poster, Proceedings of International Conference on Semiconducting & Insulating Materials (Bratislava), IEEE Publishing Co., Piscataway, NJ, USA, 80-83, June-July 2002.

CHAPTER 1

Introduction

The incredible growth of Internet and data transmission are pushing the bandwidth requirements for optical communications, particularly the expansion of metro area networks (MAN) and local area networks (LAN), at an unprecedented pace. Currently, nearly all of the optical fibre systems use the single-mode silica fibre, which has a chromatic dispersion minimum at a wavelength of 1.3 μm and an attenuation minimum at 1.55 μm. Therefore, low-cost and long-wavelength (1.3 or 1.55 μm) semiconductor laser devices are essential for this optical revolution. In particular, long-wavelength, single mode vertical cavity surface-emitting lasers (VCSELs), which can be directly modulated, operated uncooled in ambient environments, and easily packaged and coupled to fibre, are highly desirable. For example, for 850 nm VCSELs at a transmission bit-rate of 1 Gbps, the transmission distance is only about 50 m, not even useful for a small, intra-building LAN; whereas for 1.3 μm VCSELs, the transmission distance is more than 10 km.

Presently, almost all the long-wavelength communication lasers in use are fabricated from InGaAsP/InP system. However, their cost is simply far too high to meet the demands of tens of millions of lasers that might be utilised in each LAN and MAN in a modern network architecture. Moreover, it is almost impossible for InGaAsP/InP system to meet the requirements for growth of distributed Bragg reflector (DBR) mirrors for VCSELs. This is because the refractive index contrast of InGaAsP/InP is insufficient, and both thermal and electrical conductivities are too low to realise the required combination of high reflectivity and low thermal and electrical resistance. Thermal issues are particularly a problem for InGaAsP-based VCSELs because of their low characteristic temperature T_0, which results from the relatively small conduction band offset between InGaAsP and InP: $\Delta E_c = 0.4\ \Delta E_g$. This allows electrons to easily get enough thermal energy to escape from the quantum well during the operation. These limitations have pushed the worldwide investigation of alternative candidates. To lase in the 1.3–1.6 μm region, materials are required to have bandgaps between 0.95 and 0.78 eV. The potential candidate alloys are shown in Fig. 1-1.[1]

One promising candidate for the GaAs-based long-wavelength laser devices is the In(Ga)As quantum dot (QD) structure.[2] However, the commercial breakthrough has not occurred yet. Another potential alloy, InGaAsN, which can be grown lattice-matched to GaAs, was proposed by Kondow *et al.* in 1996.[1] Research on this novel quaternary alloy has revealed several advantages of this system over the InGaAsP/InP

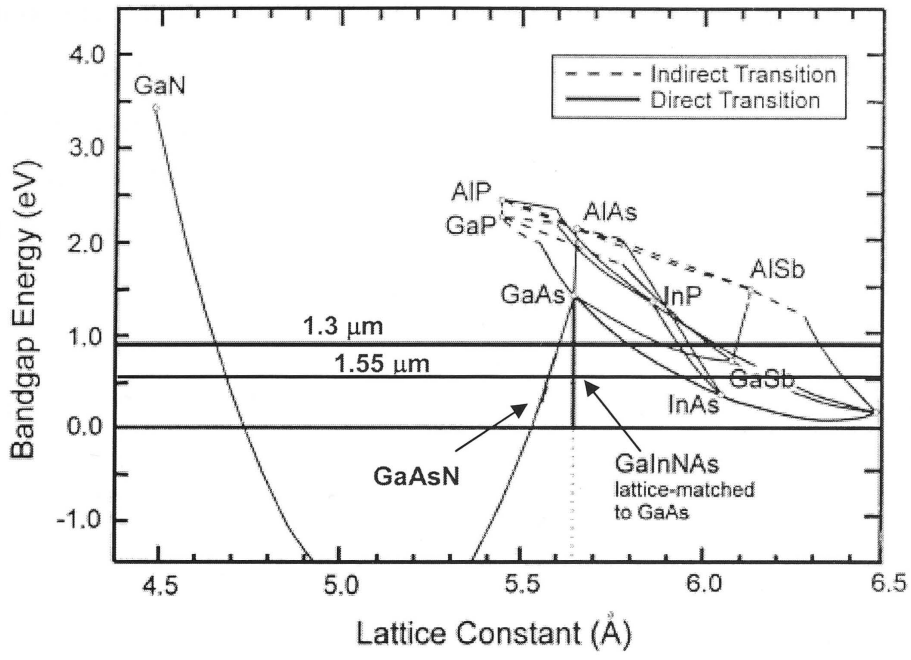

Fig. 1-1 Relationship between the lattice constant and bandgap energy of III-V alloy semiconductors. (From Ref. 1)

system, such as higher T_0,[3] easier fabrication of VCSELs using the mature GaAs/Al(Ga)As DBR growth technology,[4] and relatively cheaper and larger GaAs wafers. These properties have made InGaAsN a most attractive new material for long-wavelength laser devices. In addition to its applications in laser devices,[1,5,6] InGaAsN has also been demonstrated to be a promising candidate for high-efficiency multijunction solar cells[7,8] and heterojunction bipolar transistors.[9-11] In this thesis, the epitaxial growth, the fundamental properties, and device application of this novel material system, including GaAsN and InGaAsN, are investigated.

1.1 Fundamentals of GaAsN

Dilute III-V nitride alloys, such as InGaAsN and GaAsN, have been attracting intense experimental[1,5-17] and theoretical studies[18-23] in the past ten years or so, due to their intriguing physical properties and potential applications. As shown in Fig. 1-1, contrary to the general rules of III-V alloy semiconductors, such as AlGaAs, InGaAs, and InGaP, where a smaller lattice constant increases the bandgap, the large electro-

negativity and small covalent radius of N result in a huge bandgap bowing effect, leading to a significant decrease of bandgap as incorporation of a few percent of N in GaAs or InGaAs. The bandgap of GaAsN can even become negative when the N composition is high enough (≥ ~12%) from the theoretical calculations.[20,23] It has been demonstrated that substitution of 1% N for As in GaAs can reduce the bandgap energy by about 150-180 meV.[12,17,24] The bandgap energy (E_g) of GaAsN can be expressed as:

$$E_{g,GaAs_{1-x}N_x} = x \cdot E_{g,GaN} + (1-x)E_{g,GaAs} - b \cdot x \cdot (1-x) \quad (1.1)$$

where b is a bowing coefficient, which is N composition (x) dependent, being ~26 eV at x <1% and ~16 eV at $x > 1\%$,[25] and even going up to ~40 eV for dilute compositions ($x \sim 0.1\%$).[26]

GaAsN system is among the classic compound semiconductors studied in the N-dilute (~10^{17} cm^{-3}) form since the 1960s.[27,28] With the development of advanced epitaxial growth techniques, it became recently possible to dramatically increase the nitrogen content (to ~10^{20} cm^{-3}), thus observing the evolution of this system from the impurity limit to an alloy. This system distinguishes itself from the other more conventional isovalent III-V alloys (GaAsP, InGaAs, InGaP) in three N regimes:[19,29]

(i) In the ultradilute regime (N composition $x \leq 0.01\%$), localised, single-impurity level appears as a sharp resonance above the conduction-band minimum (CBM), as observed by photoluminescence (PL) under hydrostatic pressure.[30,31] However, in conventional alloys such as GaAs:P or GaAs:In the ensuing perturbation potential V_{As}-V_p or V_{Ga}-V_{In} is too weak to create a bound state. Moreover, these impurity levels in dilute GaAsN have an anomalously small pressure dependence compared with conventional III-V alloys.[30,31]

(ii) In the intermediate concentration regime ($0.01\% < x \leq 0.1\%$), the N-N pairs form discrete levels inside the bandgap extending in GaAs down to E_{CBM} -10 meV[30,31] or E_{CBM} -80 meV,[32,33] resulting in sharp photoluminescence (PL) lines. However, in conventional III-V alloys, such pairs give rise to broad resonances, within the valence and conduction continua, but no gap levels.[34,35]

(iii) As the N concentration increases further ($x > 0.1\%$), all the sharp PL lines of pairs or clusters disappear into a single line, additional unexpected effects are seen in GaAsN alloys, such as a huge bandgap bowing coefficient[12-15,24], an

anomalously increased conduction-band effective mass,[36,37] and a split of conduction band, etc.

In order to understand the physical origins of the unusual bandgap bowing in GaAsN alloys, much effort has been devoted to the study of the conduction band states in these alloys. The studies on electroreflectance [38] and photomodulated reflectance[21,39] spectra of (In)GaAsN alloys have discovered an additional feature (E_+) in addition to the fundamental bandgap transition (E_0[38] or E_-[21,39]) and the spin-orbit transition ($E_-+\Delta_0$). As shown in Fig. 1-2, with increasing N content, the E_+ transition shifts towards higher energies, and the E_- transition shifts towards lower energies resulting in the giant bandgap bowing effect.[21,38,39] To explain these experimental results, two major theoretical models have been proposed: band-anticrossing model[21,39-41] and empirical pseudopotential model,[19,22,42-46] which are discussed in the following sections:

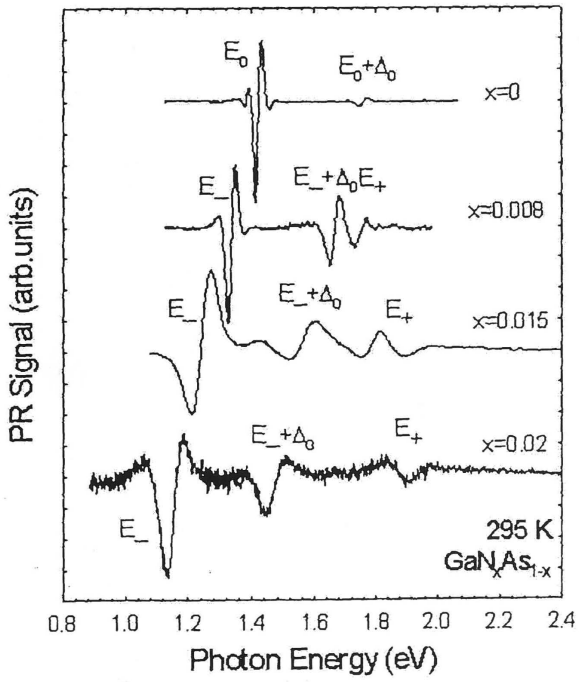

Fig. 1-2 Photomodulated reflectance spectra of $GaAs_{1-x}N_x$ samples with different N content x (from Ref. 39). The increase of N content pushes the E_- and $E_- + \Delta_0$ to lower energy and E_+ to higher energy.

Band-anticrossing model

The empirical band-anticrossing (BAC) model was introduced by Shan et al.[21] to explain the observed two-level repulsion[38] in InGaAsN alloy. As shown in Fig. 1–3, BAC model assumes that the conduction-band (CB) of the host splitting into the E_- and E_+ is caused by the interaction between the delocalised Γ minimum of the CB and the N-related level E_N ($E_N = E_V + 1.65$ eV). According to this model, the E_- subband has mainly delocalised CB-like character, whereas the E_+ subband is due to the localised E_N–like states. The strength of Γ–E_N interaction increases with increasing N content, leading to a stronger repulsion between the E_- and E_+ and thus the bandgap bowing accompanied with blueshift of the E_+ state, as observed in experiments.[38,39] Moreover, an increase of the electron effective mass and a strong non-parabolic CB have also been predicted by BAC model. The BAC model explains the conduction band splitting, and assumes that the valence band is unaffected by nitrogen.

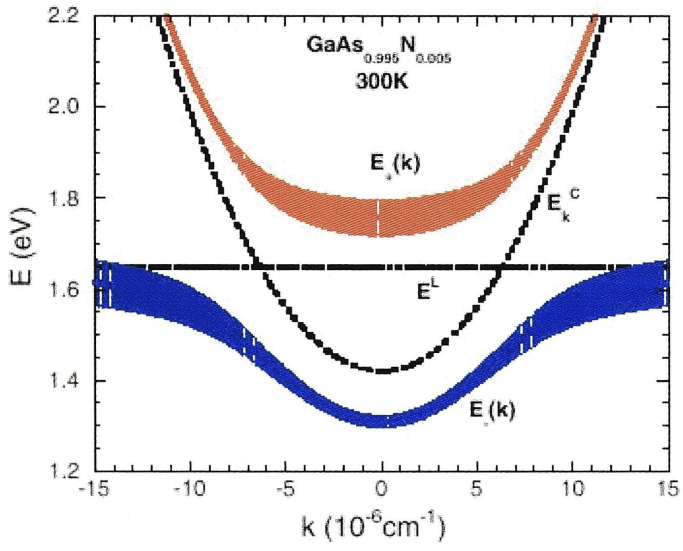

Fig. 1-3 Splitting of the conduction band to E_+ and E_- states according to the BAC model (from Ref. 47). E_k^c is the energy dispersion of the lowest conduction band of the host, and E^L is the energy of the localised states derived from the substitutional N atoms.

Empirical pseudopotential model

On the other hand, the uncorrected[42] and corrected[46] empirical pseudopotential models use a periodically repeated supercell to describe the atomic structure of the system under investigation. According to these calculations, N induces a resonant impurity state a_1(N), and induces such a strong perturbation that the host crystal states Γ_{1c}, L_{1c}, and X_{1c} mix thoroughly, forming new low-energy states. As shown in Fig. 1–4, the reduction of crystal symmetry modifies the Γ_{1c} state $a_1(\Gamma_{1c})$, splits the L_{1c} valley into $a_1(L_{1c})$, and $t_2(L_{1c})$, and splits the X_{1c} valley into $a_1(X_{1c})$ and $e(X_{1c})$. Mixing between the $a_1(\Gamma_{1c})$ and $a_1(L_{1c})$ conduction band states is responsible for the E_- subband formation, whereas the E_+ states are deduced to originate from a weighted average of the a_1(N) and $a_1(L_{1c})$ levels based on their Γ character.[46] With increasing N content, the E_+ level increases and E_- level decreases linearly with energy, respectively, resulting in the extraordinary bandgap bowing. In contrast to BAC model, the E_- states are suggested here to be localised in real space, which causes a decrease of electron mobility; and the

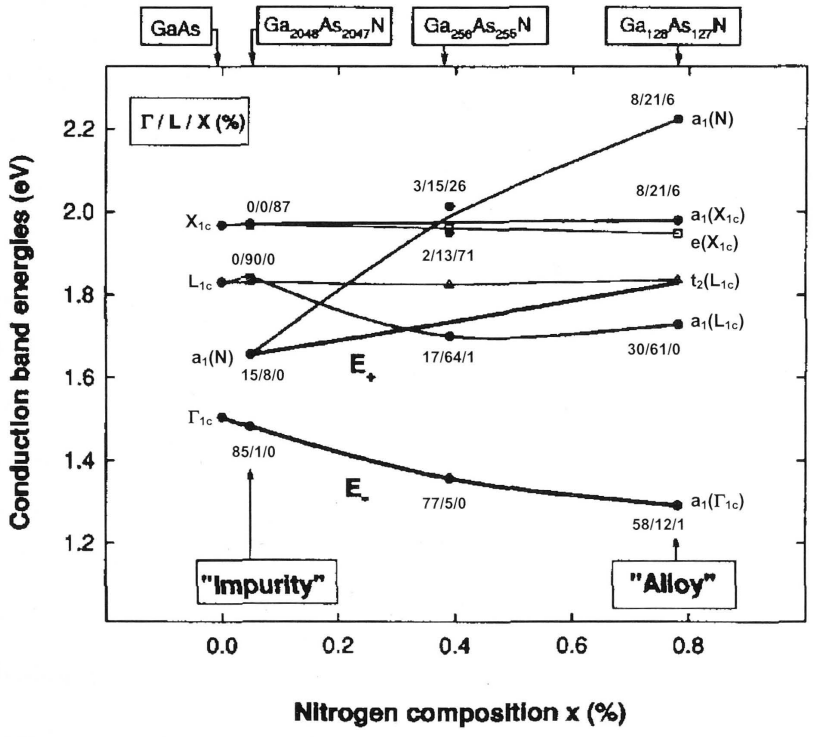

Fig. 1-4 The composition dependence of the energies of the lowest conduction band states in the dilute $GaAs_{1-x}N_x$ alloy (from Ref. 46). The percentage of Γ, L, and X character for each state is also shown, respectively.

interaction between the CB states and the resonant E_N level was also suggested to have only a minor contribution to the E_- formation.[46]

Both models provide good qualitative agreement with experimental data and can explain the compositional dependencies of E_- and E_+ levels. However, some basic parameters, such as N composition dependence of bandgap bowing coefficient, band offset and lattice constant of the (In)GaAsN alloys are still not well known and the results from different research groups are inconsistent,[12,13,25,26,48-53] probably due to the different growth conditions and the unusual physical properties of these alloys.

1.2 Thesis structure

In this thesis, metal organic chemical vapour deposition (MOCVD) is used to grow the (In)GaAsN alloy semiconductors. The major aims are to develop optimum growth conditions for different (In)GaAsN related structures, to address the key issues associated with this novel material system, such as optical properties, band structure, defects, and atomic interdiffusion, and to fabricate and test the laser devices based on InGaAsN QD structures. The structure of this thesis is as follows.

Chapter 2 presents a brief introduction to the various experimental techniques and equipment used in this thesis. MOCVD is the technique used in this work to grow various structures, such as GaAsN epilayers and quantum wells (QWs), InGaAsN QW and QDs, etc. Rapid thermal annealing (RTA), ion implantation, and dielectric film deposition are the main material processing techniques. After the processing step, a variety of techniques are used to analyse/characterise these materials. These techniques include double-crystal X-ray diffraction (DCXRD), photoluminescence (PL) and electroluminescence (EL), time resolved photoluminescence (TRPL), photocurrent, electrochemical capacitance-voltage (E-CV) profiling, sheet resistance measurements, Rutherford backscattering spectrometry–ion channeling (RBS-C), cross-sectional transmission microscopy (XTEM), and atomic force microscopy (AFM). Device processing and testing methods are also briefly described in Chapter 2.

The main body of this thesis begins with Chapter 3, in which a great amount of work on MOCVD growth of (In)GaAsN materials is presented. Much effort has been put into the calibration of growth rate and N composition of GaAsN epilayers. A number of growth parameters are systematically varied to investigate their effects on N in-

corporation and PL properties. A strain-compensating structure is proposed in Chapter 3 to dramatically improve PL properties of GaAsN QW structure. Growths of InGaAsN QW and QD structure are also presented in this chapter.

In Chapter 4, the microstructures, optical properties of InGaAsN materials are systematically studied. Based on the PL and TRPL studies, the low-temperature PL mechanism of GaAsN epilayers is proposed. A band structure model proposed by Kent *et al.*[19,45] is used to adequately explain the observed PL phenomenon. The observation of an unusual lasing phenomenon from GaAsN epilayer is also described in Chapter 4.

Chapter 5 examines the ion-implantation created defects in GaAsN epilayers by means of RBS-C and sheet resistance measurements. The ion beam-induced damage accumulation and amorphisation processes are investigated in thin GaAsN epilayers with three different N compositions under Si ion bombardment. Moreover, the implantation-induced electrical isolation is systematically studied as a function of the free carrier concentration, ion mass and the N content.

In Chapter 6, annealing with dielectric capping layers is used to investigate the atomic interdiffusion process in the InGaAsN QD structure. Deposition of a thin TiO_2 film on the sample's surface is found to be an effective approach to suppress the thermal interdiffusion in QDs. A controlled interdiffusion process has been achieved by varying the thickness of TiO_2 film.

In Chapter 7, the InGaAsN QD and a reference InGaAs QW based graded-index separate-confinement heterostructure (GRINSCH) ridge waveguide laser devices are fabricated, tested, and compared. In this chapter, a comprehensive characterisation of the laser performance, including the lasing spectrum, relationship between light output and current (*L-I*), quantum efficiency, photocurrent, absorption spectra, are examined and discussed.

Finally, a summary of this work is presented in Chapter 8.

References

1 M. Kondow, K. Uomi, A. Niwa, T. Kitatani, S. Watahiki, and Y. Yazawa, Jpn. J. Appl. Phys., Part 1 **35,** 1273 (1996).

2 D. L. Huffaker, G. Park, Z. Zou, O. B. Shchekin, and D. G. Deppe, Appl. Phys. Lett. **73,** 2564 (1998).

3 T. Kitatani, K. Nakahara, M. Kondow, K. Uomi, and T. Tanaka, Jpn. J. Appl. Phys., Part 2 **39,** L86 (2000).

4 H. Riechert, A. Ramakrishnan, and G. Steinle, Semicond. Sci. Technol. **17,** 892 (2002).

5 M. Fischer, D. Gollub, M. Reinhardt, M. Kamp, and A. Forchel, Journal of Crystal Growth **251,** 353 (2003).

6 N. Tansu, A. Quandt, M. Kanskar, W. Mulhearn, and L. J. Mawst, Appl. Phys. Lett. **83,** 18 (2003).

7 S. R. Kurtz, A. A. Allerman, E. D. Jones, J. M. Gee, J. J. Banas, and B. E. Hammons, Appl. Phys. Lett. **74,** 729 (1998).

8 D. J. Friedman, J. F. Geisz, S. R. Kurtz, and J. M. Olson, J. Cryst. Growth **195,** 409 (1998).

9 P. M. Asbeck, R. J. Welty, C. W. Tu, H. P. Xin, and R. E. Welser, Semiconductor Science & Technology **17,** 898 (2002).

10 P. C. Chang, A. G. Baca, N. Y. Li, P. R. Sharps, H. Q. Hou, J. R. Laroche, and F. Ren, Appl. Phys. Lett. **76,** 2788 (2000).

11 P. C. Chang, A. G. Baca, N. Y. Li, X. M. Xie, H. Q. Hou, and E. Armour, Appl. Phys. Lett. **76,** 2262 (2000).

12 R. Bhat, C. Caneau, L. Salamanca-Riba, W. Bi, and C. Tu, J. Cryst. Growth **195,** 427 (1998).

13 W. G. Bi and C. W. Tu, Appl. Phys. Lett. **70,** 1608 (1997).

14 S. Francoeur, G. Sivaraman, Y. Qiu, S. Nikishin, and H. Temkin, Applied Physics Letters **72,** 1857 (1998).

15 M. Kondow, K. Uomi, K. Hosomi, and T. Mozume, Jpn. J. Appl. Phys. Part 2 **33,** L1056 (1994).

16 A. Ougazzaden, Y. Lebellego, E. V. K. Rao, M. Juhel, L. Leprince, and G. Patriarche, Appl. Phys. Lett. **70,** 2861 (1997).

17 K. Uesugi, N. Morooka, and I. Suemune, Appl. Phys. Lett. **74,** 1254 (1999).

[18] S. H. Wei and A. Zunger, Phys. Rev. Lett. **76,** 664 (1996).

[19] P. R. C. Kent and A. Zunger, Phys. Rev. Lett. **86,** 2613 (2001).

[20] J. Neugebauer and C. G. V. d. Walle, Phys. Rev. B **51,** 10568 (1995).

[21] W. Shan, W. Walukiewicz, J. W. Ager, III, E. E. Haller, J. F. Geisz, D. J. Friedman, J. M. Olson, and S. R. Kurtz, Phys. Rev. Lett. **82,** 1221 (1999).

[22] L. Bellaiche, S. H. Wei, and A. Zunger, Phys. Rev. B **54,** 17568 (1996).

[23] S. Sakai, Y. Ueta, and Y. Terauchi, Jpn. J. Appl. Phys., Part 1 **32,** 4413 (1993).

[24] M. Weyers, M. Sato, and H. Ando, Jpn. J. Appl. Phys. Part 2 **31,** L853 (1992).

[25] J. Toivonen, T. Hakkarainen, M. Sopanen, and H. Lipsanen, J. Cryst. Growth **221,** 456 (2000).

[26] U. Tisch, E. Finkman, and J. Salzman, Appl. Phys. Lett. **81,** 463 (2002).

[27] D. G. Thomas and J. J. Hopfield, Phys. Rev. Lett. **150,** 680 (1966).

[28] D. G. Thomas, J. J. Hopfield, and C. J. Frosch, Phys. Rev. Lett. **15,** 857 (1965).

[29] P. R. C. Kent and A. Zunger, Phys. Rev. B **64,** 115208 (2001).

[30] X. Liu, M.-E. Pistol, and L. Samuelson, Phys. Rev. B **42,** 7504 (1990).

[31] X. Liu, M.-E. Pistol, L. Samuelson, S. Schwetlick, and W. Seifert, Appl. Phys. Lett. **56,** 1451 (1990).

[32] H. Saito, T. Makimoto, and N. Kobayashi, J. Cryst. Growth **170,** 372 (1997).

[33] T. Makimoto, H. Saito, T. Nishida, and N. Kobayashi, Appl. Phys. Lett. **70,** 2984 (1997).

[34] R. Magri, S. Froyen, and A. Zunger, Phys. Rev. B **44,** 7947 (1991).

[35] S. H. Wei and A. Zunger, Phys. Rev. B **43,** 1662 (1991).

[36] Y. Zhang, A. Mascarenhas, H. P. Xin, and C. W. Tu, Phys. Rev. B **61,** 7479 (2000).

[37] P. N. Hai, W. M. Chen, I. A. Buyanova, H. P. Xin, and C. W. Tu, Appl. Phys. Lett. **77,** 1843 (2000).

[38] J. D. Perkins, A. Mascarenhas, Y. Zhang, J. F. Geisz, D. J. Friedman, J. M. Olson, and S. R. Kurtz, Phys. Rev. Lett. **82,** 3312 (1999).

[39] W. Shan, W. Walukiewicz, J. W. Ager, E. E. Haller, J. F. Geisz, D. J. Friedman, J. M. Olson, and S. R. Kurtz, J. Appl. Phys. **86,** 2349 (1999).

[40] J. Wu, W. Shan, W. Walukiewicz, K. M. Yu, J. W. Ager, E. E. Haller, H. P. Xin, and C. W. Tu, Phys. Rev. B **6408,** 5320 (2001).

[41] W. Shan, W. Walukiewicz, K. M. Yu, J. W. Ager, E. E. Haller, J. F. Geisz, D. J. Friedman, J. M. Olson, S. R. Kurtz, and C. Nauka, Physical Review B **62,** 4211 (2000).

[42] E. D. Jones, N. A. Modine, A. A. Allerman, S. R. Kurtz, A. F. Wright, S. T. Tozer, and X. Wei, Phys. Rev. B **60,** 4430 (1999).

[43] L. Bellaiche, S. H. Wei, and A. Zunger, Appl. Phys. Lett. **70,** 3558 (1997).

[44] L. Bellaiche, S. H. Wei, and A. Zunger, Phys. Rev. B **56,** 10233 (1997).

[45] P. R. C. Kent, L. Bellaiche, and A. Zunger, Semicond. Sci. Technol. **17,** 851 (2002).

[46] T. Mattila, S. H. Wei, and A. Zunger, Phys. Rev. B **60,** R11245 (1999).

[47] J. Wu, W. Shan, and W. Walukiewicz, Semicond. Sci. Technol. **17,** 860 (2002).

[48] P. Krispin, S. G. Spruytte, J. S. Harris, and K. H. Ploog, J. Appl. Phys. **88,** 4153 (2000).

[49] P. Krispin, S. G. Spruytte, J. S. Harris, and K. H. Ploog, J. Appl. Phys. **90,** 2405 (2001).

[50] B. Q. Sun, D. S. Jiang, X. D. Luo, Z. Y. Xu, Z. Pan, L. H. Li, and R. H. Wu, Appl. Phys. Lett. **76,** 2862 (2000).

[51] B. Q. Sun, D. S. Jiang, Z. Pan, L. H. Li, and R. H. Wu, J. Cryst. Growth **227,** 501 (2001).

[52] T. Kitatani, M. Kondow, T. Kikawa, Y. Yazawa, M. Okai, and K. Uomi, Jpn. J. Appl. Phys. Part 1 **38,** 5003 (1999).

[53] W. Li and M. Pessa, Appl. Phys. Lett. **78,** 2864 (2001).

CHAPTER 2

Experimental techniques

2.1 Introduction

The main aim of this chapter is to provide an overview of the various experimental techniques used throughout this thesis. Since most of these techniques are complex and detailed explanation can be found in the references provided on each technique, descriptions are restricted to basic principles and issues involved in this work. The main techniques have been classified into four categories below:

- Epitaxial growth using metalorganic chemical vapour deposition.
- Materials processing (ion implantation, deposition of dielectric film and metal contact, and rapid thermal annealing).
- Materials characterisation (double crystal X-ray diffraction, optical and electrical techniques, ion beam analysis, transmission and scanning electron microscopy, and atomic force microscopy etc.).
- Device fabrication and testing.

2.2 Metal organic chemical vapour deposition

All the samples in this work were grown at the Australian National University (ANU) by metalorganic chemical vapour deposition (MOCVD), also often referred to as metal organic vapour phase epitaxy (MOVPE). MOCVD is a cold wall chemical vapour phase deposition process capable of producing very thin semiconductor layers with atomically abrupt interfaces. The deposition process utilises vapour phase reactions between metal alkyls, such as trimethylgallium (TMG), trimethylaluminium (TMA) and trimethylindium (TMI), with hydrides such as arsine (AsH_3) and/or non-metallic alkyls, such as dimethylhydrazine (DMHy) and tertiarybutylarsine (TBA). MOCVD technique was developed rapidly in early 1970s led by the pioneering work of Manasevit and coworkers in the late 1960s.[1,2] Nowadays, a number of obstacles related to MOCVD have been overcome and MOCVD has produced the highest-purity InP epilayers grown by any technique and GaAs as pure as by any other techniques.[3] The main advantage of MOCVD is its capability to grow a broad range of materials of high quality with a high growth rate, which is preferable for commercial production opera-

tions. However, most precursors used in MOCVD are extremely toxic, which requires scrubbing, strict monitoring and disposal of toxic waste. Comprehensive description of MOCVD process can be found in several textbooks and articles.[3-5]

In this work, all samples were grown in a modified MR Semicon MOCVD system with a Thomas Swan reactor except for parts of the laser structures which were grown in an AIXTRON AIX 200/4 horizontal flow reactor. Figure 2-1 shows the schematic of the MOCVD reactor used in this work.

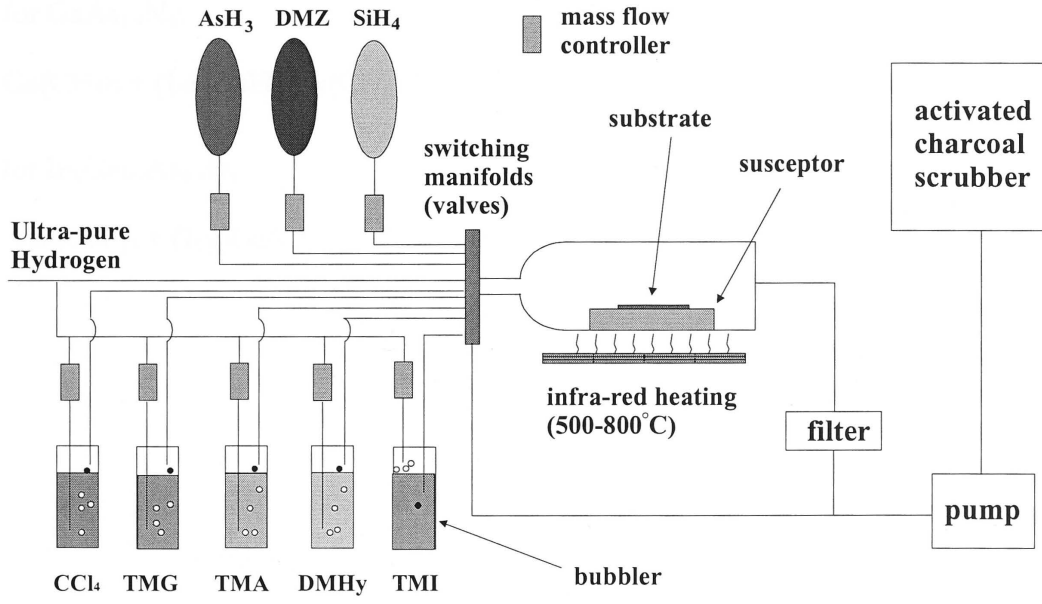

Fig. 2-1 Schematic of the MOCVD reactor used in this work.

The precursors for group III atoms were metalorganic TMG, TMA and TMI. The precursors for group V atoms were DMHy and AsH_3. Carbon tetrachloride (CCl_4) or dimethylzinc (DMZ) of 5000 ppm dilution in ultra-high-purity (UHP) H_2 were used as the p-type dopant. Silane (SiH_4) of 500 ppm dilution in UHP H_2 was used as the n-type dopant. Many of these precursors are volatile liquids, such as TMG, TMA, DMHy and CCl_4, or volatile solid such as TMI at room temperature. Therefore, they are stored in sealed steel bubblers and immersed in temperature-controlled baths.

The GaAs wafer was placed on SiC-coated graphite susceptor, which was heated *via* a three-zone infra-red lamp to the growth temperature. Transport of group III

sources (TMG and TMI) and N source (DMHy) was done by flowing the carrier gas, UHP H_2, through the organic sources *via* bubblers. The H_2 flow was carefully regulated and monitored by electronic mass flow controllers. The mixture of alkyl precursors and hydride was then introduced into the growth reactor. These precursors were cracked under elevated temperatures on the substrate surface creating constituent atoms to begin the growth process. A typical pyrolytic reaction for the growth of GaAs (shown in Fig. 2-2) can be expressed as:

$$Ga(CH_3)_3 + AsH_3 \rightarrow GaAs + 3CH_4 \tag{2.1}$$

or for $GaAs_{1-x}N_x$:

$$Ga(CH_3)_3 + (1-x)AsH_3 + x(CH_3)_2NNH_2 \rightarrow GaAs_{1-x}N_x + 3CH_4 + xCH_3NCH_2 \tag{2.2}$$

or for $In_yGa_{1-y}As_{1-x}N_x$:

$$yIn(CH_3)_3 + (1-y)Ga(CH_3)_3 + (1-x)AsH_3 + x(CH_3)_2NNH_2 \rightarrow In_yGa_{1-y}As_{1-x}N_x + 3CH_4 + xCH_3NCH_2 \tag{2.3}$$

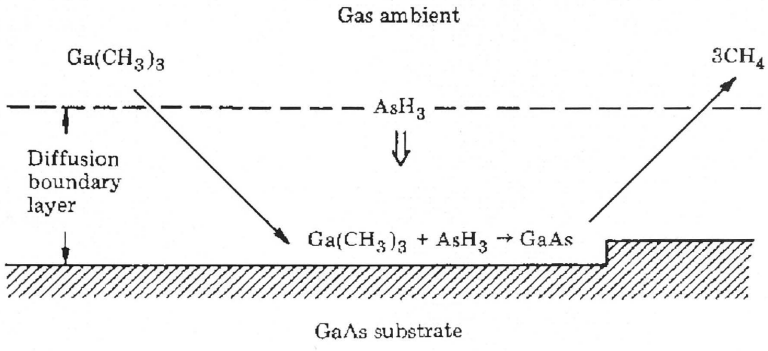

Fig. 2-2 Schematic of epitaxial growth of GaAs (from Ref. 5).

Intentional doping can be achieved by introducing the appropriate dopant sources, such as DMZ and CCl_4 (p-type) or SiH_4 (n-type), into the growth chamber. The exhaust gas mixture which may still contain toxic gases is then passed through an activated charcoal scrubber to remove the toxic components before being released to the atmosphere.

As can be seen from equations 2.1 - 2.3, the growth rate can be controlled by either group III species or group V species. Generally, the MOCVD growth ambient has a large excess of the group V constituent over the group III. Thus the growth rate is limited by the mass transport of the group III species to the growth surface at the high-temperature regime, or a combination of mass transport of the group III species and growth temperature at the low-temperature regime. The mole fraction of N, x, and In, y, in the solid $In_yGa_{1-y}As_{1-x}N_x$ are related to the vapour phase ratio of $(CH_3)_2NNH_2/AsH_3$, x_v, and the ratio of $In(CH_3)_3/Ga(CH_3)_3$, y_v, respectively. The vapour phase ratios of x_v and y_v can be expressed as:

$$x_v = \frac{f_{DMHy}}{f_{DMHy} + f_{AsH_3}} \tag{2.4}$$

$$y_v = \frac{f_{TMI}}{f_{TMI} + f_{TMG}} \tag{2.5}$$

where f_{DMHy}, f_{AsH_3}, f_{TMI} and f_{TMG} are the flow rates of DMHy, AsH_3, TMI, and TMG respectively. The detailed study of the rate of GaAsN growth will be discussed in Chapter 3.

2.3 Materials processing

2.3.1 Ion implantation

Ion implantation is a technique where ions are accelerated to a high energy and speed and injected into a material. Such energetic ions, upon impact, lose their energy *via* a series of collisions with target nuclei and electrons. These collisions can result in displacements of atoms in the target, leaving lattice defects and/or injected ions as dopant in crystalline solids. Detailed description of ion implantation may be found in several textbooks.[6-8]

Ion implantation used in this work was performed at ANU in a tandem ion accelerator (National Electrostatics Corporation 5SDH-4) with a maximum terminal voltage of 1.7 MV. Fig. 2-3 shows the schematic of the ion implanter. The ion source is a

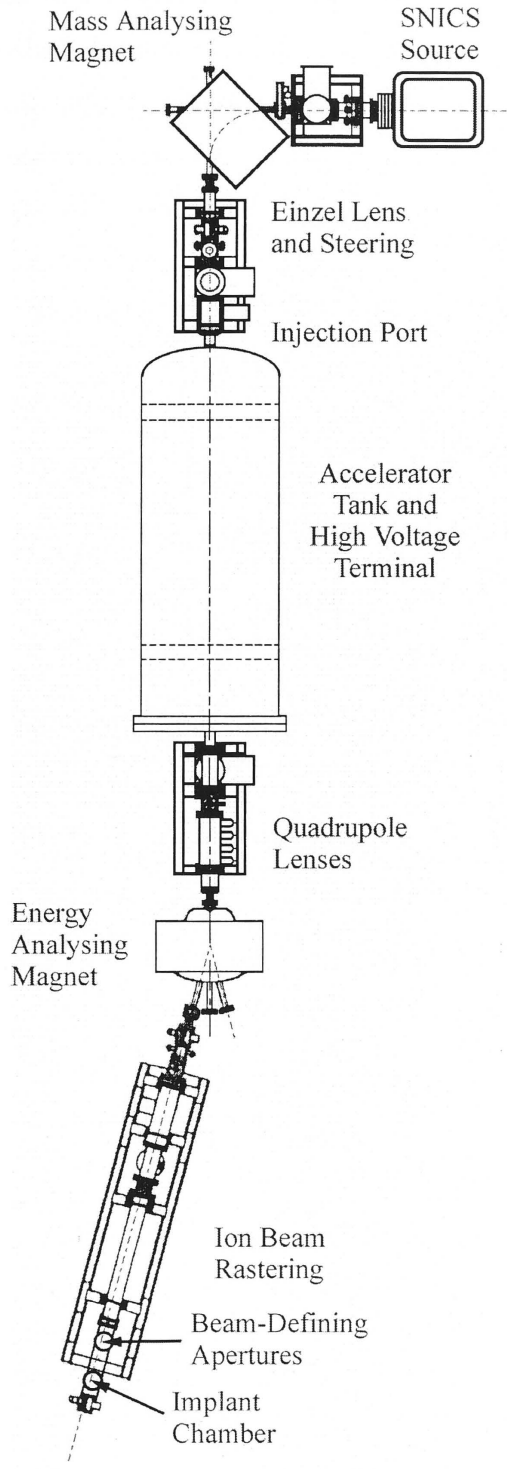

Fig. 2-3 Schematic of the 1.7 MV tandem ion accelerator used for ion implantation.

SNICS-type[9,10] (Source of Negative Ions by Cesium Sputtering) where a stream of Cs vapour is ionised into Cs^+ which are then attracted to a negatively biased Cu cathode ($\leq$ 10 kV). The ions to be implanted are normally obtained from a powder source which is pressed into a Cu cathode. The list below shows the source materials used for the various ion species used in this work.

Ions	Atomic mass (a.m.u.)[11]	Source material
H	1	TiH powder
C	12	Carbon powder
O	16	Al_2O_3 powder
Si	28	Crushed Si wafer

The sputtered negative ions are then attracted by the positively-biased extractor ($\leq$ 15 kV) and further accelerated by a bias ($\leq$ 80 kV) into a 90 ° magnet, with a path radius, R, for mass-filtering. By setting the magnetic field such that the magnetic force acting on the accelerating ions is equal to the centripetal force of the ions as they are deflected through a radius (R), then the required ions with mass (m) and charge (n) will be deflected towards the high voltage terminal, i.e.

$$B = \frac{1}{R}\sqrt{\frac{2mV_i}{qn}} \tag{2.6}$$

where B is the magnetic field, V_i is the potential of the ions and q is the electronic charge.

The high voltage terminal resides in the middle of a tank and is supplied with positive charge (up to 1.7 MV) by two pelletron chains. Since the beam path at the two ends of the tank are at ground potential, the voltage applied onto the high voltage terminal is sustained through a series of equi-potential rings separated by resistors. A set of corona points form a closed loop feedback system to ensure the voltage stability of the terminal. The mass-filtered negative ions are then electrostatically steered into the tank through the focussing system and accelerated towards the positive high voltage

terminal. At this terminal, they are partially stripped of electrons in a nitrogen charge-exchange cell to become positive ions and as a result are further accelerated towards the other end of the tank (at ground potential). Thus, the final energy of the ions, V_f, can be expressed as

$$V_f = q[V_i + (1+n)V_t] \tag{2.7}$$

where q is the electronic charge, V_i is the injected potential of the ions, n is the charge state of the ions, and V_t is the voltage at the terminal. Typically, the final ion energy is in the range of 0.2 - 10 MeV. However, if lower ion energies are required (≤ 100 keV), the stripping gas is not introduced and no charge exchange occurs in the high voltage terminal. Thus, the potential that the ions pick up upon entering the terminal is lost through deceleration upon leaving the terminal. The ions are then focussed and steered by a series of lenses and energy-filtered by another magnet. Finally, the desired ions (with the desired energy) are electrostatically scanned onto the target with rastering frequencies of 517 Hz by 64 Hz.

The targets are mounted onto a *Ni* block with vertical translation and rotational movements. A *k*-type thermocouple is mounted inside the Ni block close to the surface to measure the temperature as close as possible to the samples. The samples are held onto the block using clips or conductive silver paste. Heating and cooling of the block can be achieved *via* an embedded resistive heating element, and liquid nitrogen, respectively. Implantation is normally carried out when the vacuum in the target chamber is ≤ 1×10^{-6} Torr to minimise contamination. Secondary electron emission is suppressed by a Cu cage maintained at -300 V that surrounds the target. The *Cu* cage is also cooled by liquid nitrogen to condense any contaminant molecules in the chamber. Dosimetry measurements are carried out with a capacitive-coupled charge integrator.

2.3.2 Plasma enhanced chemical vapour deposition

In this work, plasma enhanced chemical vapour deposition (PECVD) was used to deposit the dielectric layers of SiO_2 for the intermixing studies and device fabrication (ridge waveguide lasers). This was done using an Oxford Plasmalab 80 Plus plasma enhanced chemical vapour deposition (PECVD) system shown in Fig. 2-4.

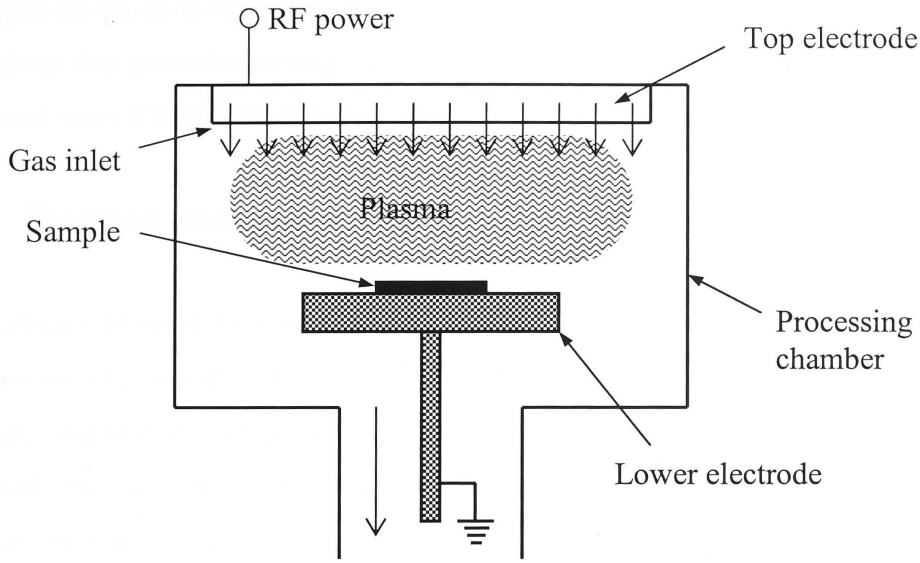

Fig. 2-4 Schematic of PECVD system used in this work.

The principle of PECVD is based on nonequilibrium glow discharge,[12] which is defined as a partially ionised gas containing equal volume concentrations of positively and negatively charged particles (mostly ions and electrons, respectively) existing in different concentrations of ground-state and excited states.[13] Non-equilibrium glow discharges are generated by subjecting the gas to a radio frequency (RF) electric field. The small concentration of free electrons which are initially present in the gas are accelerated by the electric field. Acquiring sufficiently high energy, the electrons collide with atoms in the gas, resulting in excitation and ionisation, in the latter case creating additional electrons which are also accelerated by the electric field. In this way an avalanche of accelerated electrons creates a steady state glow discharge. At steady state, a fraction of the ground-state parent atoms in the gas phase undergoes electron impact dissociation and excitation such that highly reactive species are created, which in turn diffuse towards the sample, adsorb on the surface, undergo chemical reactions and surface migration, and eventually form a solid film. Since the reactive species produced in the plasma have lower energy barriers to physical and chemical reactions than the parent species, they can react at low temperatures, which is the major advantage of PECVD compared with other thin film deposition techniques.

As shown in Fig. 2-4, the plasma is generated between two parallel, circular electrodes, with the sample being placed on the lower, electrically grounded electrode.

The upper electrode is connected to a 13.56 MHz RF generator and the gas reactants are fed in from the gas inlet through the top electrode, entering the plasma region. The gases used were 5% SiH_4 (in N_2) and N_2O for SiO_2 deposition.

2.3.3 Electron beam evaporation

Dielectric films of TiO_2 for interdiffusion studies and metal-contact layers for laser devices were deposited on the surface of samples by a Temescal CV-8 electron beam (E-beam) evaporator. In this case, a focused E-beam is used to heat the material to be deposited. The advantage of E-beam is that it can be focused on a small region of the target material and heat to very high temperatures to evaporate the source material. The material then deposits on all the surfaces of the evaporation chamber, including on exposed sample surfaces. A quartz crystal is used for monitoring the thickness of deposited materials.

2.3.4 Rapid thermal annealing

Rapid thermal annealing (RTA), also known as rapid thermal processing (RTP), is very important for both Si and GaAs technology.[14] It was carried out by using an AET thermal RX rapid thermal annealer in this work. RTA is a crucial step in preparing samples for almost all aspects of this work. Annealing process is an indispensable step to recover the crystal quality of as-grown GaAsN epilayers and is a part the device fabrication techniques. RTA was also used to investigate the interdiffusion process. All the RTA processes were performed in an Ar or N_2 ambient with temperature ramping at 100°C/s. When the annealing temperature was higher than 400 °C, samples were protected using sacrificial GaAs wafers as the proximity cap (i.e., sandwiching the sample between two fresh pieces of GaAs wafers) to prevent excessive loss of As.

2.4 Materials characterisation

2.4.1 Double-crystal X-ray diffraction

Double-crystal X-ray diffraction (DCXRD)[15,16] is a non-destructive technique widely used for the measurement of composition, layer thickness and strain in epi-

taxial structures. The advantage of DCXRD is its capability to separate the Bragg peaks from the epilayer and the substrate which have a small difference in the lattice parameters, such as GaAs and GaAsN. A Bede QC2a diffractometer was used in this work. The schematic of this system is shown in Fig. 2-5.

A beam of Cu Kα X-rays is collimated to a reference crystal of the same material and orientation as the specimen which also acts as a monochromator. Bragg conditions are satisfied when the planes of the specimens are parallel to those of the reference crystal, i.e.

$$n\lambda = 2d\sin\theta_B \tag{2.8}$$

where d is the spacing of the Bragg planes, λ is the X-ray wavelength, θ_B is the Bragg angle [33.026 ° for (004) GaAs] and n is the order of diffraction (n = 1, 2,....). A slit is positioned in front of the detector to limit the angular divergence and improve the resolution. A small rotation of the specimen with respect to the reference crystal will result in the loss of intensity from the substrate. However, when the conditions of diffraction are satisfied for the Bragg spacing of the GaAsN epilayer, a secondary peak in addition to GaAs is observed.

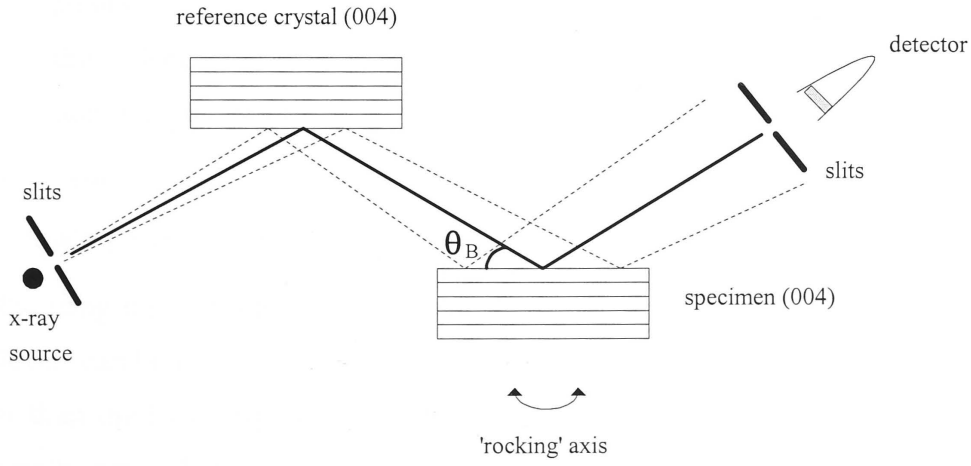

Fig. 2-5 Schematic of a double-crystal diffractometer (DCXRD).

2.4.2 Photoluminescence and electroluminescence

Luminescence is defined as a non-equilibrium emission of radiation, i.e. the light emitted by a material system in excess of thermal radiation.[17] It can be excited by irradiation with photons, where it is called photoluminescence (PL), or by applying an electric field, where it is called electroluminescence (EL).

PL is a very powerful and non-destructive spectroscopic technique for studying the intrinsic and extrinsic properties of semiconductors. This technique requires only small quantity of material and is particularly useful for semi-insulating materials where electrical contact is difficult. A reasonably monochromatic optical excitation source (such as a laser) is used to create electron-hole pairs. These photoexcited carriers then diffuse and recombine to generate photons (luminescence) with characteristic energies related to the bandgap. The interband recombination between these carriers can generally be classified into three categories:[18]

(i) Fundamental transitions, which include exciton recombination and conduction-band-to-valence-band transitions. These transitions are due to free/bound exciton recombination, or electron-hole recombination near the bandgap.

(ii) Transitions between a band and an impurity level, i. e. transitions involving an electron from the conduction band to an acceptor state or from a donor to the valence band, or transitions between a deep level and the conduction/valence band.

(iii) Donor-acceptor transitions, which are due to the recombination of donors and acceptors, such as Si-S and Si-Te in GaP.

By using light of different energies (above or below the band gap), different energy levels can be probed. Typically, in standard PL measurements, light with energy higher than the band gap is used and the photo-excited carriers then diffuse and recombine to emit photons. For the QW or QD structures, photo-excited carriers are preferentially trapped in the wells or dots due to their lower energy states. The recombination of the electron-hole pairs generates photons with characteristic energies of the quantised energy levels of the wells or dots, which can then be collected and analysed.

Detailed theory and experimental aspects of PL and optical processes in semiconductors may be found in references 17-20.

PL is a main technique employed in this work to investigate the band structure of GaAsN epilayers and the interdiffusion process. The experimental setup is schematically shown in Fig. 2-6. A 4 W Coherent Innova 70 Ionpure water-cooled Ar ion laser or a diode-pumped frequency-doubled solid-state (DPSS) laser is used as the excitation source. The laser lines of 514.5 nm and 532 nm are used for Ar ion laser and DPSS laser, respectively. The samples for PL measurements are mounted with vacuum grease on a liquid N_2 cooled or closed-cycle He cryostat. The laser beam is directed onto the sample through a chopper operating at a few hundred Hz. The resulting luminescence is then collected by a thermoelectric-cooled Si CCD camera or a thermoelectric-cooled InGaAs photodiode with a built-in pre-amplifier *via* a set of lenses and a spectrometer. The signal from the InGaAs photodetector is analysed by a lock-in amplifier, which is tuned to the frequency of the chopper. A desktop computer is then used to control the spectrometer for a wavelength scan and also records the PL signal.

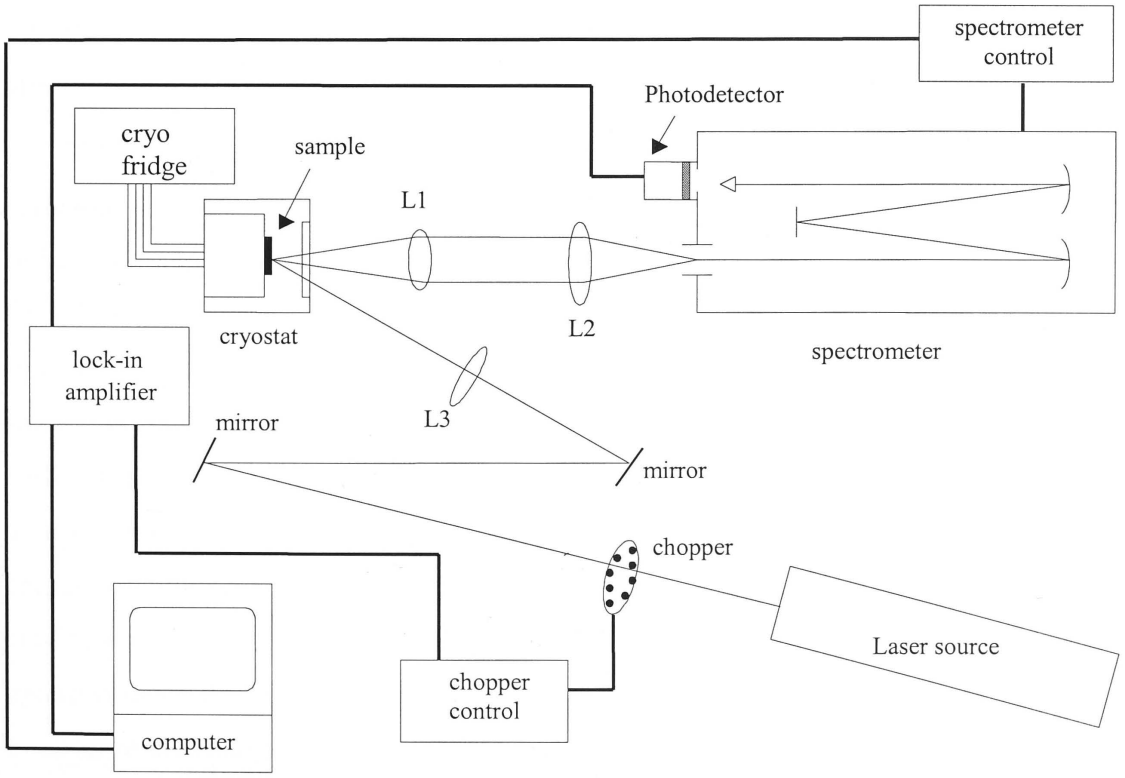

Fig. 2-6 Schematic of the setup for photoluminescence measurements.

In addition to the photoluminescence, electroluminescence (EL) *via* electrical excitation can give the similar information about the active region in a structure with a *p-n* junction. Electrical excitation is capable of producing a very high density of electron-hole pairs near the *p-n* junction and EL converts this electrical energy directly into radiation. EL is a very useful tool to study the spontaneous and the stimulated emissions in laser devices. The setup for EL measurements is almost identical to that for PL measurements, except a bias is applied on the sample's top and bottom surfaces and the luminescence is collected from the sample's edge.

2.4.3 Time resolved photoluminescence

The length of time a photoexcited carrier can remain in the conduction (or valence) band is an important parameter directly related to semiconductor material quality, purity, and doping level. Time-resolved photoluminescence (TRPL) is the method of choice to measure this important parameter. Although there are numerous ways to measure carrier lifetime, TRPL has many advantages over the other methods. Most importantly, TRPL is contactless and highly sensitive. It can be used to extract sub-nanosecond lifetimes and in many instances may be used to deduce information about specific recombination mechanisms.

TRPL measurements in this work were done by using luminescence up-conversion technique, as shown schematically in Fig. 2-7. In this technique the laser pulse itself acts as a switching gate and relates the photoluminescence signal with the time domain. The output pulse train from an ultra-fast laser firstly splits into two. The semiconductor sample is excited by one pulse train (pump) and the PL signal from the sample is collected and focused on a nonlinear crystal. The second pulse train (probe) is directed and focused on the same spot on the nonlinear crystal after passing through a variable delay lens. The angle between the two beams and the angle of the nonlinear crystal are adjusted for phase matched sum-frequency generation at a given luminescence photon energy. The time resolution is limited by the laser pulse width, and the group velocity dispersion in the nonlinear crystal. The luminescence is then monitored to observe the changes in the sample produced by the pump. The up-conversion signal from the photoluminescence and the pump beam is directed through filters and a spectrometer to eliminate the background light from the signal and is detected with a photomultiplier tube (PMT) giving it an extremely high sensitivity. If the relative delay

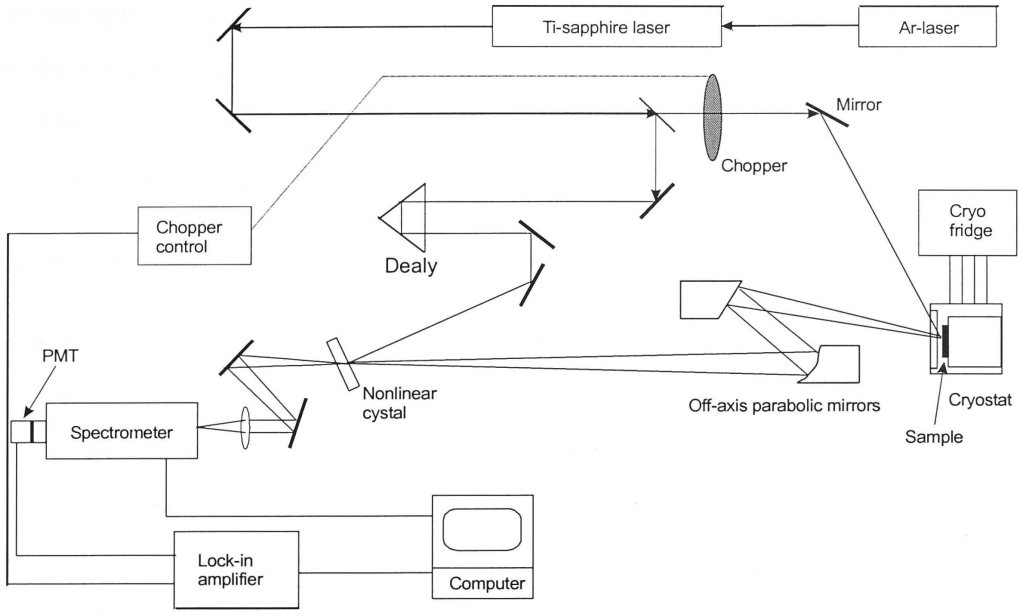

Fig. 2-7 Schematic of experimental setup for up-conversion TRPL.

between the two beams is scanned, the time evolution of the luminescence at a given photon energy can be acquired. Time resolved luminescence spectra can be obtained by keeping the delay fixed and synchronising the scanning angle of the nonlinear crystal and the spectrometer.

In the measurements, the sample was mounted in a variable-temperature close-cycle He cryostat and excited by a femtosecond (fs) self-mode locked Ti:sapphire laser. The laser was tuneable between 750 and 900 nm, with a pulse width of 80 fs, a frequency of 85 MHz, and an output power of 180 mW at λ = 780 nm. The optically excited carrier concentration was about 3 x 10^{10} carriers/cm^2 and the time resolution was about 100 fs. Detailed description may be found in references 21-23.

2.4.4 Absorption spectroscopy

In this work, to obtain absorption spectra of the laser devices, two approaches were used: photocurrent measurements and a multisection-device technique. The photocurrent technique has an advantage to span over a large spectral length, but it is difficult to calibrate in terms of absolute values. Measuring absolute values of the ab-

sorption is an easy task for the multisection technique, but the wavelength range is limited to the spectral width of spontaneous emission from the second section, which provides the source of the light to be absorbed in the first section of the multisection device. These two approaches can be combined in principle, allowing the absorption spectra from photocurrent measurements to be calibrated in terms of absolute units.

Photocurrent technique

Photocurrent is the opposite process of electroluminescence and was used to characterise the QD and QW laser devices in this thesis. The experimental setup is schematically shown in Fig. 2-8. In this case, the light from a tungsten-filament lamp is spectrally resolved through a monochromator before being focused on the front facet of the laser device. The light produces an excess of free carriers in the device. These free carriers move in response to local fields or an applied reverse bias, resulting in a photocurrent through an external circuit. The absorption of the light by the device as a function of wavelength can be obtained by controlling the monochromator and measuring the photocurrent. Furthermore, the effect of external electric field on the photocurrent can also be measured by varying the applied bias.

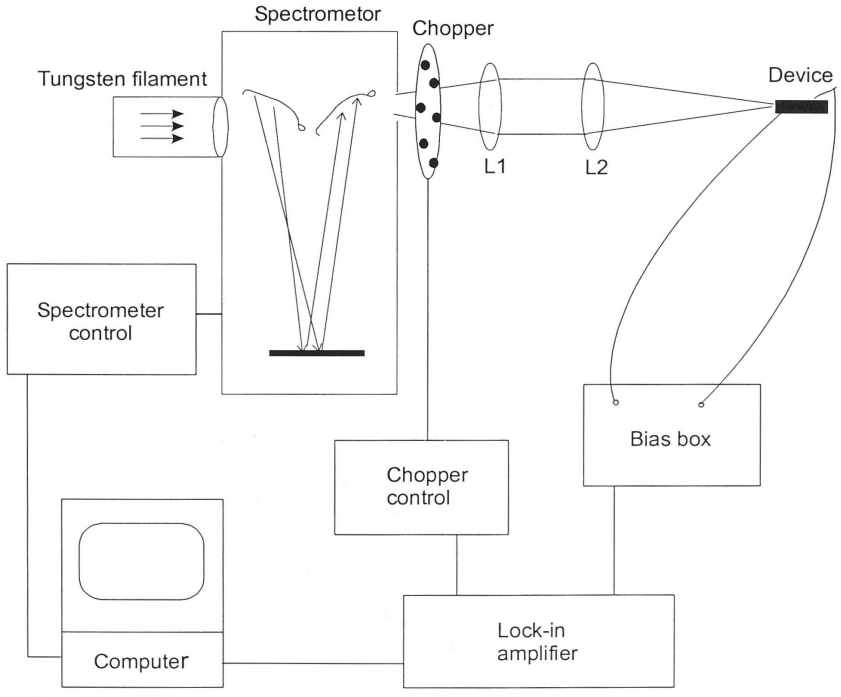

Fig. 2-8 Schematic of experimental setup for photocurrent measurements.

Photocurrent technique is a powerful tool, which provides insight into the energy, the oscillator strength and the polarisation of different transitions. When the reverse bias is applied to a *p-i-n* structure, such as the laser device in this work, changes of the transition strength and energy in the absorption spectrum will provide information about the built-in electric field and the polarisation of the electrons and holes in the device, which is crucial for both the fundamental understanding of the device physics and for device applications. Photocurrent is a complementary characterisation tool to photoluminescence or electroluminescence. While the photoluminescence or the electroluminescence spectra of about 30-60 meV in width allow us to probe the states at the bottom of the conduction band and the top of the valence band, photocurrent spectroscopy probes the absorption of states in the range of 1 eV above the spontaneous emission peak, which are not accessible in luminescence spectra under typical excitation conditions.

Multisection-device technique

To study the light absorption behaviour of the laser devices, an interesting approach is to compare the absorption spectra measured by the photocurrent technique with that measured by a multisection device. The latter technique is based on the analysis of the amplified spontaneous emission spectra[24-26] using a multisection device, as shown in Fig. 2-9. This device consists of six to eight 1 mm long (L) sections cleaved in an individual chip, electrically separated by a 100 μm of unpumped region. Only the first two sections are biased and the rest of the device acts as an absorber. In this way, the reflected signal at the back mirror of the second section is absorbed before becomes significant at the front mirror to ensure that we only have single pass amplifica-

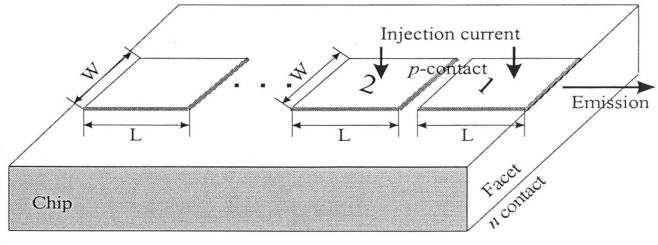

Fig. 2-9 Schematic of the multisection device used for absorption measurements in this work.

tion. Taking an absorption coefficient of at least 2.5 cm^{-1} in the unpumped region, a simple calculation of the light propagation after multiple reflections along the whole length shows that the errors introduced by the light reflection at the back facet are not important for a long device.

In all cases, if gain saturation is neglected the sum of P_1 and P_2 should be smaller than or equal to (when the gain is small) $P_{1\text{-}2}$, where P_1 is the power measured when only the first section close to the front facet is forward biased, P_2 is power measured when only the second section behind the front facet is biased, and $P_{1\text{-}2}$ is measured when both sections are biased. When the sum $P_1 + P_2$ is larger than $P_{1\text{-}2}$, gain saturation effects take place. We use this criterion to estimate the critical current for which errors in the final measured absorption coefficient in terms of absolute values are to be expected. The modal absorption coefficient can be then calculated according to:

$$\alpha = \frac{1}{L} ln(\frac{P_2}{P_1}) \tag{2.9}$$

and the modal gain can also be calculated according to:

$$g = \frac{1}{L} ln(\frac{P_{1-2}}{P_1} - 1) \tag{2.10}$$

In this work, only the absorption coefficient was calculated and investigated.

2.4.5 Electrochemical capacitance-voltage (EC-V) measurements

Depth profiling of the conventional C-V measurements is limited by the breakdown voltage of a Schottky diode, especially in the case where the epilayer has a very high doping concentration. To overcome this limitation, EC-V was used to measure the carrier concentration of the highly doped epilayer. EC-V uses the same principle as the standard C-V but the former adopts stepped surface etching for stepped reverse bias voltage. The Schottky diode is formed at the surface of the semiconductor material contacted with the electrolyte. A very small bias voltage needs to be applied during EC-V measurements, avoiding the breakdown of the Schottky diode. A very large depth can be profiled by using the step-by-step etching process. Detailed theory and practice of EC-V measurements can be found in reference 27. In this work, EC-V meas-

urements were carried out with a BIO-RAD PN 4300 profiler using NaOH:EDTA as an electrochemical etching solution for GaAs.

2.4.6 Sheet resistance

Sheet resistance (R_s) is the resistance between the opposite edges of a square of arbitrary dimensions. Sheet resistance is independent of the size of the square and is determined by material resistivity and sample thickness. Thus, R_s is a intrinsic property of a sheet material. For R_s measurements, rectangular samples with a size about 6 x 4 mm^2 were cut from GaAsN epilayers grown on semi-insulating GaAs substrates. On two opposite sides of each sample, ohmic contacts were fabricated by manually applying indium (In) strips and sintering at 250°C for 2 minutes. The ohmic behaviour of the sintered In contacts has been verified by their linear current-voltage characteristics. Sheet resistance of ion implanted GaAsN was measured in-situ (without breaking vacuum in the target chamber of the implanter) with a specially designed sample holder by using a Keithley 617 electrometer. Measurements were performed when the resistance had stabilised after each ion dose had been delivered.

2.4.7 Rutherford backscattering spectrometry – ion channeling

Rutherford backscattering spectrometry (RBS) is a well-established quantitative ion beam analysis technique, based on classical Coulomb scattering of a fast light ion by a more massive stationary atom. It is commonly used to analyse the compositions of target samples. With this technique, a beam of mono-energetic light ions (such as H or He) is bombarded onto the specimen to be analysed. The incident ions collide with target atoms and are then backscattered into a detector-analysis system, where their energy distributions are analysed to yield information about the atomic constituents and also a depth profile of the target. If the incident ions are aligned along a low index crystallographic direction of a crystalline target (axial channeling), then most of the ions are steered into the 'channels' between the rows and planes of the crystal, causing a significantly reduced backscattered ion yield. On the other hand, if the target is randomly oriented with respect to the incident ions, then fewer ions are channeled along the crystallographic axes and more direct scattering will occur. The aligned technique is generally referred to as ion channeling or RBS-channeling (RBS-C). If defects are

present in the sample, such as displaced atoms in the channeling paths, then the yield of the backscattered ions will increase. In this way, the channeling spectrum can give a depth and concentration profile of defects present in the material, and is ideal for analysis of defect distribution and concentration in ion-implanted semiconductors.

The geometry of the RBS detection system is important in the quantitative analysis of the results, such as, the depth profile. The energy loss of an incident ion with energy E_o in traversing a distance x, from the surface and backscattered by an As atom is related to the following expressions 2.11 and 2.12,[28] as illustrated in Fig. 2-10:

$$\Delta E_{As} = K_{As}E_0 - E_{1,As} = [S]_{As}x \tag{2.11}$$

$$[S]_{As} = \frac{K_{As}}{\cos\theta_1}\frac{dE}{dx}\Big|_{in} + \frac{1}{\cos\theta_2}\frac{dE}{dx}\Big|_{out} \tag{2.12}$$

where K_{As} is the kinematic factor of As, $E_{1,As}$ is the energy of the ion backscattered off an As atom at x, $[S]_{As}$ is the energy loss factor of As and $dE/dx\,|_{in}$ and $dE/dx\,|_{out}$ are the rate of energy loss evaluated at the inward and outward paths, respectively. For regions near the surface, the depth, x, is small and hence, the relative change of the ion energy along an incident path is also small. Thus, it is sufficient to use a surface energy approximation, which reduces the expression 2.12 to:

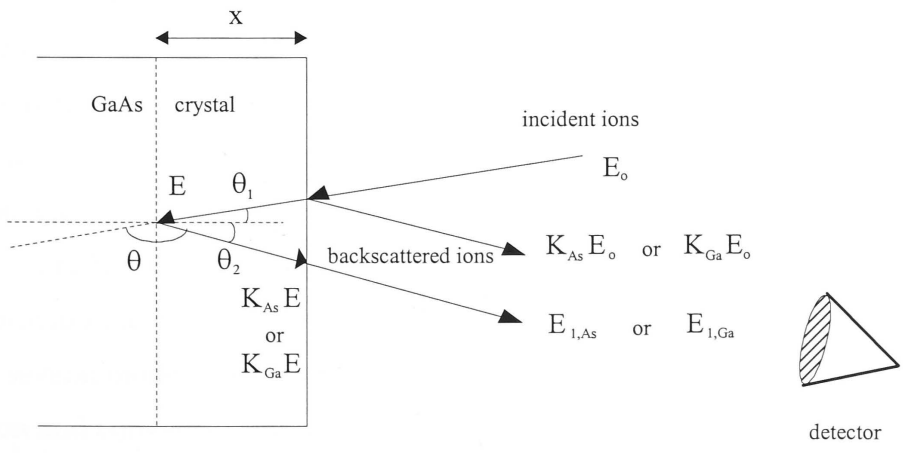

Fig. 2-10 Schematic of the RBS setup for a specific geometry.

$$[S]_{As} = \frac{K_{As}}{\cos\theta_1}\frac{dE}{dx}\bigg|_{E_o} + \frac{1}{\cos\theta_2}\frac{dE}{dx}\bigg|_{K_{As}E_o} \tag{2.13}$$

Similar expressions are true for an ion scattering off a Ga atom. Further treatment of RBS and ion channeling may be found in references 28 and 29.

The RBS-C measurements in this work were conducted at ANU using a 1.7 MV tandem accelerator (National Electrostatics Corporation 5SDH), which has a similar design to the 1.7 MV implanter depicted in Fig. 2-3 except that it has a plasma source (not a SNICS) and a high-voltage tank with only one pelletron chain. Helium (He) ions are generated by means of RF discharge of the He gas plasma. The ions are then mass/energy-filtered for 2 MeV $^4He^+$ through a magnet before being steered onto the target. A collimator box is set along the path of the ions to define a well-collimated beam of particles. The sample is mounted on a 4-axis goniometer for channeling measurements. Backscattered ions are collected by two Si Au-surface barrier detectors. One of the detectors is fixed at a scattering angle of 168° (backward detector) while the other is movable in the scattering angle range of 90-120° (glancing-angle detector). When a backscattered ion impinges on the detector, electron-hole pairs are generated which are then swept by an applied electric field. The resulting current pulse is proportional to the energy of the backscattered ions and is electronically amplified and recorded onto a multi-channel analyser.

2.4.8 Transmission electron microscopy

Transmission electron microscopy (TEM) is a well-established technique to study defects and microstructure of materials. It operates by focusing a beam of electrons through a thin (electron transparent) specimen. The electron beam is (mainly) elastically scattered, or diffracted by the interaction with the sample. The specimen modulates the characteristics (amplitude and phase) of the transmitted beam allowing localised information in the specimen to be measured. A TEM specimen may be investigated in several modes, most commonly, in the diffraction mode (such as selected area diffraction and convergent beam diffraction) and imaging mode (such as bright-field, dark-field and weak beam imaging). Details of the operation of a TEM and the analy-

sis of the images are beyond the scope of this work but may be found in references 30 and 31.

Cross-sectional transmission electron microscopy (XTEM) was employed in this work to study the defects and microstructure of the samples. The microscopy work was carried out at the Electron Microscope Unit at the University of Sydney using a Philips CM12 transmission electron microscope operating at an accelerating voltage of 120 kV.

XTEM specimen preparation

XTEM specimens were prepared by using the conventional mechanical polishing followed by the ion beam thinning. Firstly, a few slices in size of about 2 x 1 mm^2 were cleaved from the sample along {100} planes, and then fixed on a Gatan specimen mount with epitaxial layer facing to the mount. These specimens were mechanically grinded to a thickness of about 200 μm on a water-resistance sand paper and then taken off from the grinder. In order to simultaneously compare the microstructure of different samples, four grinded specimens from different samples were glued together, with epitaxial layer facing the same direction, as shown in Fig. 2-11(a). To distinguish the different samples under the microscope, the specimens were sandwiched between three supporting GaAs wafers, with one on the epilayer side and two others on the substrate side.

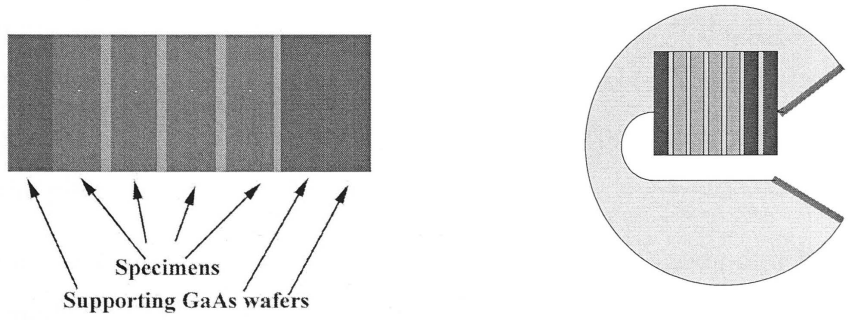

Fig. 2-11 Schematic of TEM specimens (a) sandwiched between GaAs wafers, and (b) mounted on an open-slot Cu grid.

A batch of four specimens was then fixed on a Pyrex tripod with thermoplastic wax and both cross-sectional sides were mechanically grinded and polished until they were free of deep scratches. By adjusting the height of two rear legs of the Pyrex tripod, a wedge was formed on the one cross-sectional side during the grinding and polishing process. The whole batch of the specimens was then mounted on a open-slot Cu grid with M-bond 610 epoxy, as shown in Fig. 2-11(b), and cured in an oven at 80°C for 30 min. Final thinning the specimens to electron transparency was carried out by a 3 keV beam of Ar ions in a Gatan 600 Ion Miller. During ion milling the specimen was rotated to ensure uniform sputtering. To minimise preferential sputtering of certain elements (As in this work), the specimen was cooled by a liquid nitrogen stage during ion milling.

2.4.9 Atomic force microscopy

The AFM development followed the conception of the scanning tunneling microscope (STM). The STM, first developed in the early 1980's, operates by bringing a sharp tip under bias into close proximity to the surface and stimulating a small current flow.[32] However, in this way, only conducting samples can be imaged. In response to this limitation the AFM was developed.[32] The AFM uses force instead of current to obtain an image using similar principles to the STM. A very sharp tip (SiN tip in this work) is used to probe and map the morphology of the sample surface by bringing the tip and the sample close together. The AFM tip is mounted on the end of a cantilever with a low spring constant (usually ~ 1 N/m). A schematic of the operation of an AFM is shown in Fig. 2-12. A laser is aligned on the reflective back of the tip and adjusted to detect the reflected signal by using the photodiode detector. As the tip is scanned across the sample, the deflection of the cantilever is recorded by the reflection of the laser onto the photodiode.

There are two main modes of AFM operation, contact-mode and tapping-mode. In contact mode, the tip is always in contact with the surface of the sample being imaged. A constant contact force (~ 1 mN) is applied to the cantilever by a piezo and maintained by a feedback system. The measured deflection from the nominal value is a measure of the features on the sample surface and is displayed as an image of the sample. Contact-mode is the most common method used in AFM because of the ease

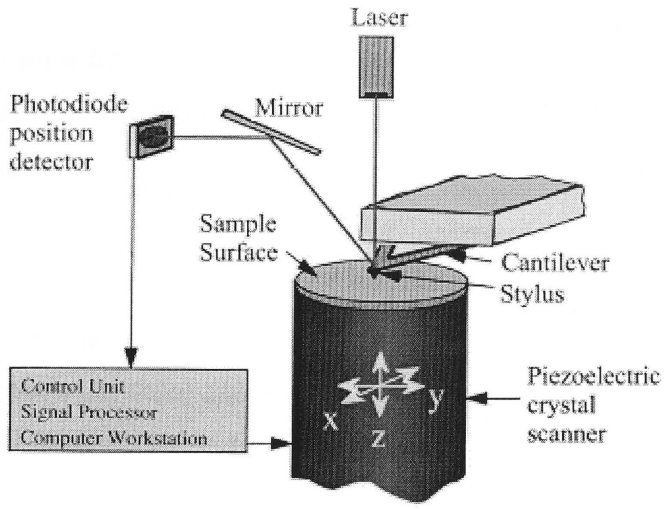

Fig. 2-12 Schematic showing the operation of an atomic force microscope.

of operation and the relatively inexpensive cost of the tips. In tapping-mode, the cantilever is oscillated at a frequency near its resonance during scanning. The oscillation is driven by a constant driving force and the amplitude is monitored. When the tip is lowered into close proximity to the surface, the oscillation amplitude is reduced and this new tapping frequency is maintained. This is done by a feedback system that changes the tip height in response to the measured oscillation amplitude. In the tapping-mode cantilever displays a resistance to displacement and therefore is less susceptible to being 'pulled' down onto the surface. Hence, it is possible to image using much lower contact forces than for contact-mode AFM.

Since semiconductor materials are, in general, relatively hard materials, contact-mode was used for all the samples used in this study. The AFM measurements were performed at room temperature in air using a Digital Instruments Nanoscope III scanning probe microscope located at the Department of Applied Mathematics within the Research School of Physical Sciences and Engineering at the Australian National University.

2.4.10 Device fabrication and characterisation

In this work, a *p-i-n* InGaAsN QD-based graded-index separate-confinement heterostructure (GRINSCH) was designed and fabricated into the ridge waveguide laser devices and characterised.

Device fabrication

A series of processing steps is required to process the multilayered materials into devices, normally involving three main steps: photolithography, etching, and metallisation, as briefly described below and shown in Fig. 3–13.

(i) Photolithography

Photolithography is a method of creating patterns on a semiconductor wafer. It defines where to etch, implant or metallise and is one of the most important steps of in semiconductor device processing.[33] In this process, a layer of photoresist (AZ5214-E) was spun on the sample at a speed of 4000 rpm for 30s and baked at 85°C for 15 minutes. The sample was then patterned by exposing the photoresist with ultra-violet light through a mask using a mask aligner (Karl Suss MJB 3 UV 300). After exposure, the photoresist was developed in a diluted developing solution (AZ312 : H_2O = 2 : 1) followed by a hard bake at 120°C for 2 minutes.

(ii) (Wet) Etching

After patterning, the samples were chemically etched to form the desired geometry. The etchant used in this work was a mixture of H_2O : H_2O_2 : H_3PO_4 at a ratio of 3 : 1 : 1 and was held in an ice bath to ensure the reproducibility. In the fabrication of ridge-waveguide QW lasers, the etched regions outside the ridge were passivated by deposition of a 200 nm thick SiO_2 film. The formation of the ridge improves the confinement of light in the lateral direction due to the small change in refractive index across the ridge.

(iii) Metallisation

One of the final steps to fabricate an optoelectronic device is making electrical contacts to the device by deposition of metals on the semiconductor surfaces. In this work,

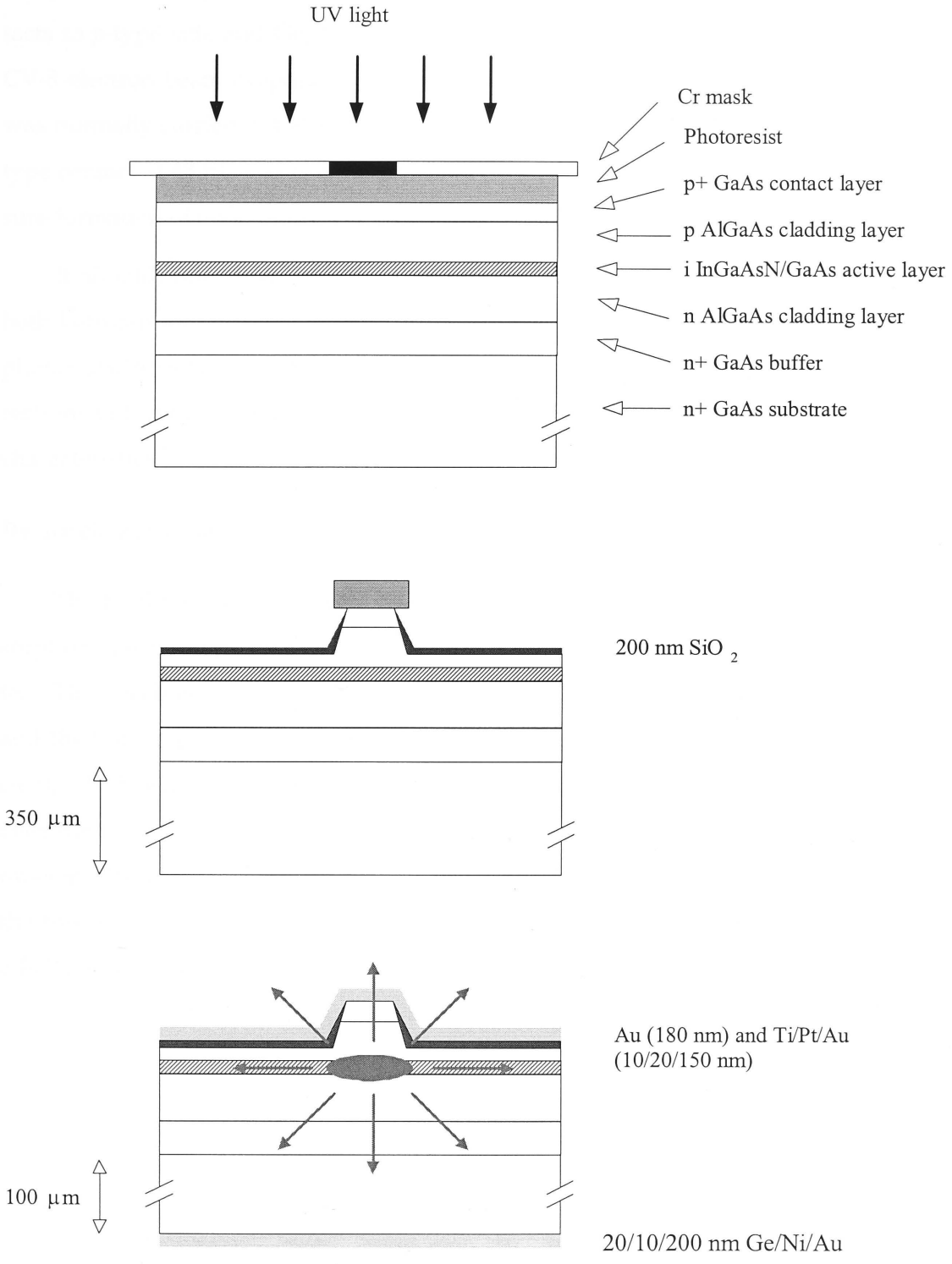

Fig. 2-13 Schematic of the three major steps in processing of a ridge-waveguide laser, from top: photolithography, etching and metallisation.

Au (180 nm) and (Ti/Pt/Au (10/20/150 nm) were evaporated for making ohmic contacts to *p*-type side and Ge/Ni/Au (20/10/200) for *n*-type side, by using a Temescal CV-8 electron beam evaporator. To improve the quality of the contacts, evaporation was normally carried out at pressures < $8x10^{-6}$ Torr. After evaporation, alloying of p-type contact at 430°C and n-type contact at 380°C for 1 minute were carried out to ensure formation of good ohmic contact.

It should, however, be noted that several other processing steps were required both between and after these main steps, such as polishing, ultrasonic cleaning, and photoresist removal, etc. After fabrication, the lasers were cleaved along the [100] directions to form the cavity mirrors and then tested for both their electrical and optical characteristics.

Device characterisation

The final laser devices were characterised using various techniques, such as absorption spectroscopy and electroluminescence spectra described earlier in this chapter. These techniques enable us to probe the QD transitions in the absorption spectra and the lasing spectra, and to obtain the absolute values the modal absorption coefficient, which will be discussed in detail in Chapter 7. The light output power of each laser device *versus* injection current (*L-I*) was measured using an InGaAs optical multimeter. These measurements provide several key parameters of the devices, such as the threshold current density, the external quantum efficiency, the internal quantum efficiency, and the internal loss.

References

1 H. M. Masasevit and W. I. Simpson, J. Electrochem. Soc. **12,** 156 (1968).

2 H. M. Manasevit, Appl. Phys. Lett. **116,** 1725 (1969).

3 G. B. Stringfellow, *Organometallic Vapor-Phase Epitaxy: Theory and Practice*, Second Edition. (Academic Press, San Diego, 1999).

4 J. J. Coleman and P. D. Dapkus, "*Metalorganic chemical vapor deposition*" in *III-V Semiconductor Materials and Devices*, edited by R. J. Malik (North Holland Publishers, Amsterdam, 1989).

5 T. F. Kuech, Mat. Sci. Rept. **2,** 1 (1987).

6 J. W. Mayer, L. Eriksson, and J. A. Davies, *Ion Implantation in Semiconductors* (Academic Press, New York, 1970).

7 G. Dearnaley, J. H. Freeman, R. S. Nelson, and J. Stephen, *Ion Implantation* (North-Holland Publishers, Amsterdam, 1973).

8 *Ion Implantation and Beam Processing*, edited by J. S. Williams and J. M. Poate (Academic Press, Sydney, 1984).

9 R. Middleton, C. T. Adams, and N. I. Methods, Nucl. Instrum. Methods **118,** 329 (1974).

10 R. Middleton, Nucl. Instrum. Methods **214,** 139 (1983).

11 *Handbook of Chemistry and Physics*; 73rd ed., edited by D. R. Lide (CRC Press, Florida, 1992).

12 B. Chapman, *Glow Discharge Processes* (John Wiley, New York, 1980).

13 R. Reif, in *Handbook of Plasma Processing Technology: Fundamentals, Etching, Deposition and Surface Interactions*, edited by S. M. Rossagnel, J. J. Cuomo, and W. D. Westwood (Noyes Publications, Westwood, 1980).

14 R. B. Fair, *Rapid Thermal Processing* (Academic Press, San Diego, 1993).

15 B. K. Tanner, J. Crystal Growth **99,** 1315 (1990).

16 B. K. Tanner and D. K. Bowen, J. Crystal Growth **126,** 1 (1993).

17 D. Dragoman and M. Dragoman, *Optical Characterization of Solids* (Springer, Berlin, 2002).

18 J. I. Pankove, *Optical Processes in Semiconductors* (Dover Publications Inc, New York, 1971).

[19] H. B. Bebb and E. W. Williams, "*Photoluminescence I : Theory*" in *Semiconductors and Semimetals, Vol. 8, Transport and Optical Phenomena*, edited by R. K. Willardson and A. C. Beer (Academic Press, New York, 1972).

[20] E. W. Williams and H. B. Bebb, "*Photoluminescence II : Gallium Arsenide*" in *Semiconductors and Semimetals, Vol. 8, Transport and Optical Phenomena*, edited by R. K. Willardson and A. C. Beer (Academic Press, New York, 1972).

[21] M. B. Johnston, PhD Thesis, The University of New South Wales, 1999.

[22] J. Shah, IEEE J. Quantum Electron. **24,** 276 (1988).

[23] J. Shah, *Ultrafast Spectroscopy of Semiconductors and Semiconductor Nanostructures* (Springer-Verlag, Berlin, 1996).

[24] S. D. McDougall and C. N. Ironside, Electr. Lett. **31,** 2179 (1995).

[25] M. Korbi, A. Groning, H. Schweizer, and J. L. Gentner, J. of Appl. Phys. **92,** 2942 (2002).

[26] J. D. Thomson, H. D. Summers, P. J. Hulyer, P. M. Smowton, and P. Blood, Appl. Phys. Lett. **75,** 2527 (1999).

[27] P. Blood and J. W. Orton, *The Electrical Characterization of Semiconductors : Majority Carriers and Electron States* (Academic Press, London, 1992).

[28] W.-K. Chu, J. W. Mayer, and M.-A. Nicolet, *Backscattering Spectrometry* (Academic Press, New York, 1978).

[29] J. S. Williams and R. G. Elliman, "*Channeling*" in *Ion Beam for Material Analysis*, edited by J. R. Bird and J. S. Williams (Academic Press, Sydney, 1989), p. 261.

[30] P. J. Goodhew and F. J. Humphreys, *Electron Microscopy and Analysis* (Taylor and Francis Ltd., London, 1988).

[31] P. B. Hirsch, A. Howie, R. B. Nicholson, D. W. Pashley, and J. M. Whelan, *Electron Microscopy of Thin Crystals* (Butterworths, London, 1967).

[32] D. A. Bonnell, *Scanning Probe Microscopy: Theory, Techniques, and Applications* (Wiley-VCH, New York, 2000).

[33] W. M. Moreau, *Semiconductor Lithography: Principles, Practices and Materials* (Plenum Press, New York, 1988).

CHAPTER 3

MOCVD growth of (In)GaAsN alloy materials

3.1 Introduction

Due to the large miscibility gap between GaN and GaAs,[1,2] studies on N incorporation in GaAs had been limited to doping levels (i.e. [N] < 10^{19} cm^{-3}) until Weyers and Sato reported the growth of $GaAs_{1-x}N_x$ with x up to 1.6% using MOCVD with the plasma-cracked NH_3 as the N source.[3,4] The unusual feature of this alloy is a strong red shift of the PL emission with increasing N content. Another important feature of this direct bandgap alloy system is the ability to grow lattice-matched GaAsN (with 20%N) on Si[5] or lattice-matched InGaAsN on GaAs.[6] These features have stimulated extensive experimental and theoretical studies, in particular, a great amount of effort has been put into epitaxial growth of these alloys.[3-5,7-16] To date, it has been possible to grow single-phase GaAsN on the GaAs substrate with a few percent of N using various techniques, such as MBE,[5,6,13,16] MOCVD,[3,4,7-12] and chemical beam epitaxy (CBE)[14,15]. Nitrogen concentrations as high as 10% and 5.6% in GaAsN have been obtained by MBE[13] and MOCVD,[10] respectively. However, the growth of GaAsN alloy is appreciably more complex and challenging than that of other GaAs based systems, due to (i) large differences in atomic radii (1.21 Å for As *vs* 0.75 Å for N) as well as in electronegativity values;[17] (ii) differences in crystal structures of the binary parental compound (zinc-blende structure for GaAs and wurtzite or zinc-blende structure for GaN); (iii) extremely low equilibrium solubility of N in GaAs.[18-20] In order to incorporate sufficient N in GaAs, the growth has to be done at low growth temperatures and under non-equilibrium growth conditions. Thus, when the N concentration and/or growth temperature increase, phase separation tends to occur as observed by different groups.[20-22] This new epitaxy challenge requires firstly to choose a suitable growth technique combined with an appropriate N-containing precursor, and secondly to optimise specific growth conditions for (In)GaAsN alloys. As MOCVD is the technique used in this thesis, the following section reviews some growth issues related to MOCVD.

Due to the low growth temperature that is required for (In)GaAsN alloys to incorporated sufficient N, a N precursor with low decomposition temperature is very important. As a second property, a low toxicity and low explosive nature of the precursor is also required for safety concerns. Because of these requirements, unsymmetrical 1,1-dimethylhydrazine (DMHy)[8,9,23-25] has been widely used as the N source for

MOCVD growth. It was also the N source used in this work. Figure 3-1 illustrates the chemical bonds of DMHy molecules, which comprise NH_2 and CH_3 radicals.

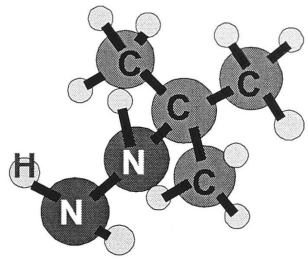

Fig. 3-1 Illustration of 1,1-dimethylhydrazine (DMHy) molecules.

The pyrolysis process of DMHy has been investigated in detail by Bourret-Courchesne *et al.*[26] using a vertical stainless-steel reactor and Lee *et al.*[27] using a horizontal tube, respectively. For the co-pyrolysis study, DMHy and triethylgallium (TEG) were used in a H_2 ambient in the former study,[26] whereas DMHy and TMG were used in a He or D_2 ambient in the latter one.[27] The relationships between percent decomposition of DMHy and temperature from these two reports are shown in Fig. 3-2. In the

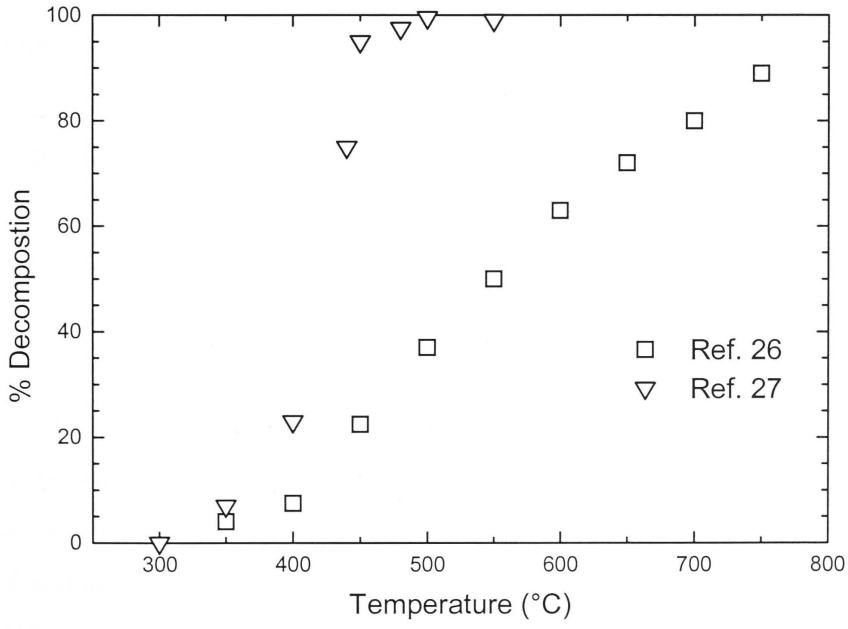

Fig. 3-2 Percentage decomposition of DMHy in H_2 as a function of temperature.

former report, the temperatures for 50% (T_{50}) and 100% (T_{100}) decomposition of DMHy were at 550 °C and 800 °C, respectively. The authors also found that the pyrolysis of DMHy begins with the splitting of the N-N bonds and the consequent cleavage of $N(CH_3)_2$ radical. Whereas in the latter report, Lee *et al* found that T_{50} and T_{100} were about 420 °C and 500°C, respectively. They also reported that the N-C bond in the $N(CH_3)_2$ radical did not cleave, implying that only NH_2 can contribute to the active N atoms. Since the combination of a horizontal reactor and a co-pyrolysis of DMHy and TMG used in the latter report is similar to that we used in this work, therefore, the latter pyrolysis behaviour of DMHy might be more representative of that taking place in this work.

In this chapter, the growth rate and uniformity of GaAsN epilayers were firstly calibrated. Then, MOCVD growth of different III-V nitride materials, including GaAsN epilayers on GaAs and AlGaAs, GaAsN/GaAs QW, N-δ-doped GaAs, and InGaAsN QWs and QDs, were explored. In particular, two major growth parameters affecting N incorporation, growth temperature and molar flow ratio of DMHy to the total flow of group V (DMHy + AsH_3), DMHy/V, in GaAsN growth have been carefully investigated. Furthermore, a kinetic model of MOCVD growth of GaAsN on GaAs and a new structure to improve the PL efficiency of GaAsN/GaAs QW were proposed.

3.2 Growth of GaAsN epilayers on GaAs

3.2.1 Experimental

All samples used in this study were grown on (100) GaAs by MOCVD at 76 Torr. Firstly, the substrate was heated to 800 °C in an ambient of H_2 and AsH_3 and held at this temperature for 10 min to desorb any surface oxides. Then the substrate was cooled down to 650 °C and a ~250 nm thick GaAs buffer was grown. The growth of GaAsN layers was then commenced by switching DMHy into the reactor when the temperature was stabilised at growth temperature (T_g = 500 - 630 °C). The flow rate of AsH_3 was fixed at 4.5 x 10^{-4} mol/min during the growth of all GaAsN layers. The flow rate of DMHy was varied in the range from 5.7 x 10^{-5} to 2.6 x 10^{-3} mol/min. The N content and thickness of GaAsN epilayers were determined by (004) DCXRD using Vegard's law and assuming no strain relaxation and a Poisson's ratio of 0.333. The thick-

nesses of some GaAsN layers grown on an AlAs/GaAs superlattice structure were also measured using scanning electron microscopy (SEM). The relationship between N concentration, x, and the peak separation between the substrate and the GaAsN epilayer, $\Delta\theta$, in the (004) X-ray diffraction rocking curves is:

$$x = 2.0 \times 10^{-5} \cdot \Delta\theta \tag{3.1}$$

3.2.2 Calibration of growth rate and uniformity

Growth rate of GaAsN epilayers

In order to precisely control the growth of multiple layer structures, the MOCVD reactor has been carefully calibrated for the growth of (Al)GaAs materials.[28,29] It was found that the uniformity of these epilayers is almost independent of growth temperatures between 600 and 750 °C and the total flow rate of group III metal organic precursors (or growth rate), but dramatically affected by H_2 carrier gas flow or reactor pressure. A thickness uniformity of better than 5% over a 2" wafer was achieved at the optimum carrier flow rate of 17.5 standard litres/min. Also the growth rate was almost independent of typical growth temperatures for (Al)GaAs in the range of 600 - 750 °C. Thus the growth rate is limited by the mass transport of the group III reactants to the growth surface. A linear relationship was found as

$$r_g = 1.264 \times 10^6 f_{III} \tag{3.2}$$

where r_g is the growth rate in nm/min and f_{III} is the flow rate of group III reactants in mole/min.

However, the growth rate of GaAsN epilayers could be different to that of (Al)GaAs, due to the growth temperature and growth ambient being different in these two cases. Therefore, we carefully calibrated the growth rate and uniformity for GaAsN growth again. Results are shown below.

Figure 3-3 shows the relationship between the growth rate of GaAsN epilayers and the growth temperature at different DMHy/V ratios. The flow rates of TMG and AsH_3 were fixed at 1.935 x 10^{-5} and 4.5 x 10^{-4} mol/min, respectively. It is clearly seen that the epitaxial growth between 500 - 600 °C is highly dependent on the temperature, indicating the growth is in the kinetically limited regime. When the growth tempera-

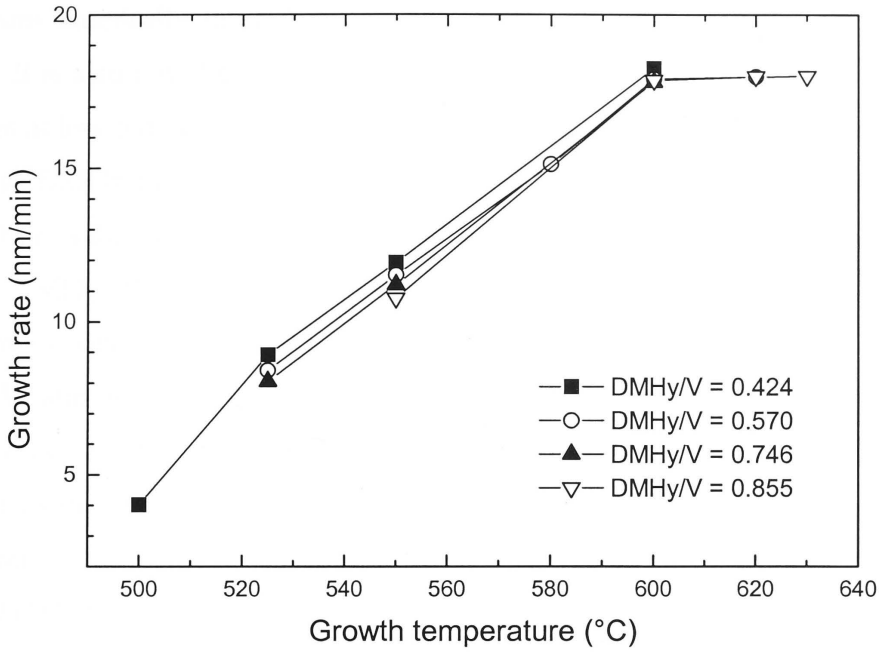

Fig. 3-3 Relationship between the growth rate of GaAsN epilayers and the growth temperature.

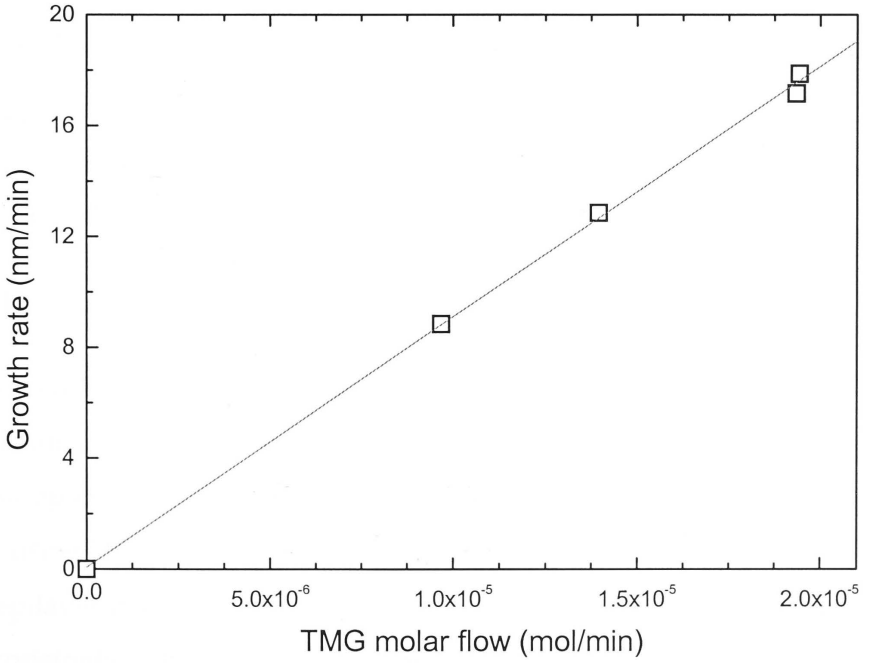

Fig. 3-4 Growth rate of GaAsN epilayers versus group III (TMG) molar flow.

ture is higher than 600°C, the growth rate stays unchanged, corresponding to the transition from kinetically limited growth regime to the mass-transport-limited growth regime. It is also noted that with increasing DMHy/V ratio, the growth rate slightly decreases at low temperatures (but there is little difference at high temperatures). This is because DMHy firstly react with TMG to form the DMHy-TMG adduct during the MOCVD growth,[27] so the concentration of the DMHy-TMG adduct increases with increasing DMHy/V ratio, resulting in the reduction of TMG flux to react with AsH_3. Furthermore, since the N incorporation efficiency is very low (only a few percent at a DMHy/V ratio of 0.57), we know the adsorption coefficient of the DMHy-TMG adduct must be much smaller than that of TMG. Therefore, increasing DMHy/V ratio eventually reduces the concentration of Ga adatoms on the sample surface, hence the slower growth rate. This result is consistent with the MOMBE[30,31] and MOCVD[32] studies using TEG and DMHy.

At growth temperature $T_g \geq 600$ °C, the growth rate was found to linearly depend on the flow rate of group III. Figure 3-4 shows a linear relationship between the TMG molar flow and the growth rate of GaAsN at 600 °C, which can be expressed as:

$$r_g = 9.039 \times 10^5 f_{TMG} \tag{3.3}$$

where r_g is the growth rate in nm/min and f_{TMG} is the flow rate of TMG in mole/min. Comparing equation 3.3 with 3.2, we can see that the growth rate of GaAsN is slower than that of GaAs, which might be also due to the formation of DMHy-TMG adduct which reduces the flow of TMG.

Uniformity

It is well known that incorporation of N into (In)GaAs tends to lead to composition variation or even phase separation.[20-22,33-35] To examine the uniformity of the GaAsN samples grown in this work, we measured the X-ray diffraction spectra over a 2" wafer using DCXRD. The peak separation ($\Delta\theta$) between the GaAs substrate and the GaAsN epilayer is shown in Fig. 3-5. The N deviation (~ 2 x 10^{-5} $\Delta\theta$) across the 2" wafer is surprisingly as larger as 50%. However, the thickness deviation is better than 7%. In the following studies of growth parameters, the DCXRD scan was performed on the centre of each wafer to minimise the experimental error.

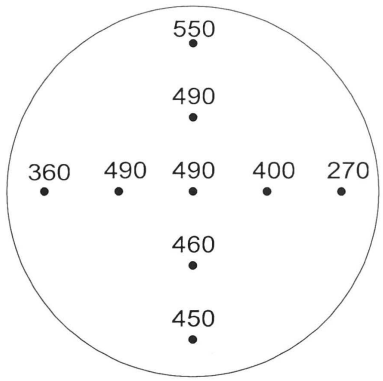

Fig. 3-5 DCXRD peak separation ($\Delta\theta$) in arc sec between the GaAs substrate and the GaAsN epilayer across a 2" wafer.

3.2.3 Growth parameters affecting N incorporation

After the calibration and optimisation of growth parameters, GaAsN epilayers with N content in the range from 0.1% to 4.5% can be readily grown on GaAs substrates. Figure 3-6 shows the experimental and simulated (004) DCXRD rocking curves of GaAsN epilayers with various N contents. The thicknesses of these layers were between 150 nm and 750 nm depending on the N content. The simulated spectra were obtained using the commercially available Bede-RADS program based on Takagi-Taupin X-ray equations.[36-38] The measured narrow GaAsN peaks and the good agreement between the simulated and experimental spectra indicate that GaAsN epilayers with excellent crystal quality have been coherently grown on GaAs substrates.

In the growth of GaAsN, because N and As atoms are competing with each other for the same lattice site, a high DMHy/V or a low As/III ratio is preferred to incorporate high content of N. Therefore, in this study, GaAsN epilayers were grown at a fixed low As/III ratio of 23.3, i.e., the flow rates of TMG and AsH_3 are maintained at 1.935×10^{-5} and 4.5×10^{-4} mol/min, respectively. Two other important growth parameters, DMHy/V ratio and growth temperature, were investigated in detail and the results are presented in the following sections.

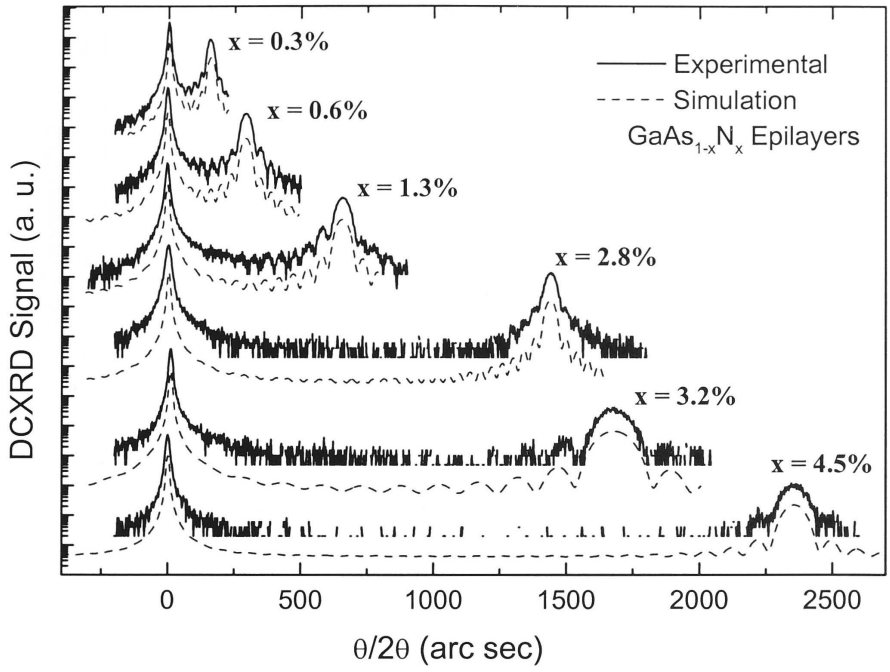

Fig. 3-6 Experimental and simulated DCXRD (004) rocking curves of $GaAs_{1-x}N_x$ epilayers with different N contents. The curves are shifted vertically for clarity.

DMHy/V-ratio

Figure 3-7 shows the N incorporation as a function of fractional DMHy molar flow at different growth temperatures. It is clear that N incorporation is strongly dependent on the DMHy/V ratio for all the temperatures investigated. However, this effect becomes less pronounced at higher growth temperatures, which might be due to the increasing amount of AsH_3 decomposition as well as the higher desorption of N at higher temperatures. These data were very useful in the following studies as they provide an empirical relationship between the vapour concentration and solid concentration of N at these growth temperatures.

Growth temperature

The growth temperature is a crucial parameter for all epitaxial techniques. It can affect all chemical reactions during the MOCVD growth. Figure 3-8 depicts the Arrhenius plot of N content as a function of growth temperature with different DMHy/V ratios. Obviously higher growth temperatures lead to a lower N incorporation, as

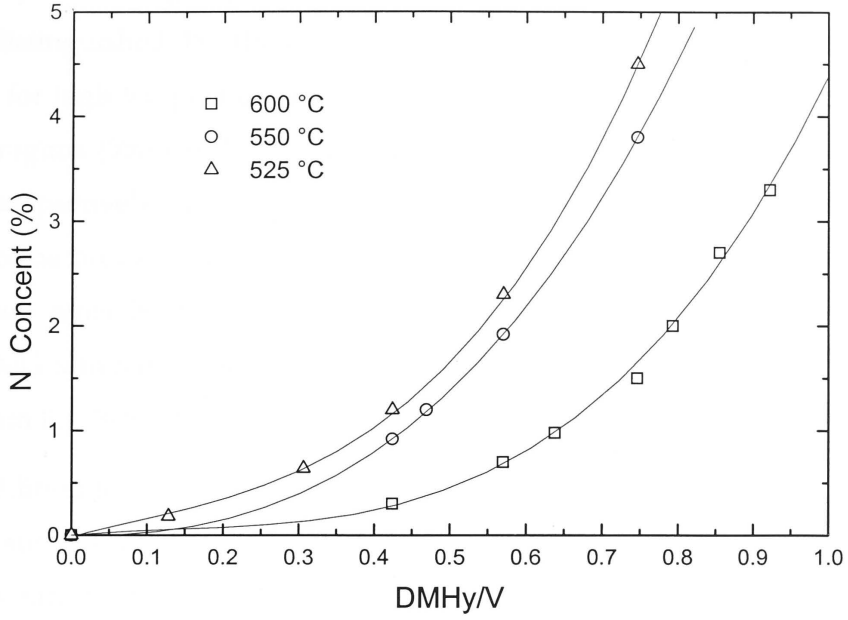

Fig. 3-7 Nitrogen incorporation in GaAsN as function of fractional molar flow of DMHy at various growth temperatures. The lines are just a guide for the eye.

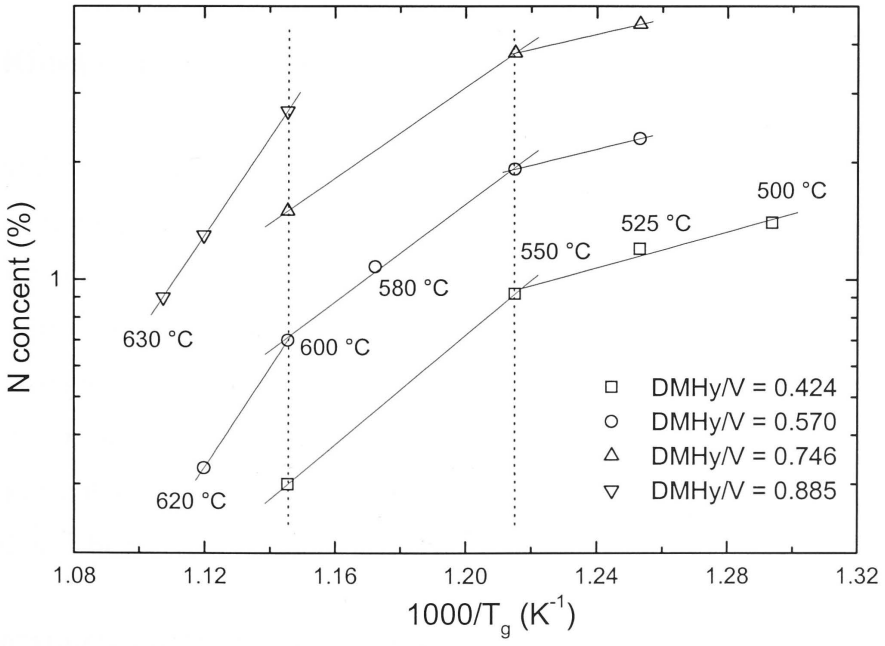

Fig. 3-8 Arrhenius plot of nitrogen incorporation in GaAsN as a function of the growth temperature.

reported by different groups.[8,11,23,31,32] Three temperature regimes of N incorporation can be distinguished by three different activation energies, which are about 57 kcal/mol for high temperature regime (600 - 630 °C), 29 kcal/mol for moderate temperature regime (550 - 600 °C), and 11 kcal/mol for low temperature regime (500 - 550 °C) , respectively. The activation energy of moderate temperature regime is comparable to the previous reported values.[23,31,32] The increase of activation energy with temperature must be primarily related to the sticking coefficient of N adatoms or DMHy-TMG adducts, which decreases at higher temperatures. Another feature observed from Fig. 3-8 is that the activation energy is independent of the DMHy/V.

In addition to the growth temperature and the DMHy/V ratio, other growth parameters, such as carrier (H_2) flow rate, reactor pressure, and growth rate by changing TMG flow rate, were also varied to investigate their effect on N incorporation. It was found that increasing H_2 flow rate or reactor pressure slightly reduces the N content in GaAsN, and growth rate has little effect on N incorporation for TMG flow rates of 9.67 x 10^{-6} to 1.94 x 10^{-5} mol/min. Based on these results, the growth temperature and the fractional DMHy molar flow, DMHy/V, are identified as key factors that affect the N incorporation in GaAsN. Precise control of N content in the range from 0.1% to 4.5% can be obtained by using the appropriate growth conditions.

3.2.4 Kinetic growth model

To understand the process of MOCVD growth of GaAsN described above, we present a simple kinetic model based on Langmuir isotherm mechanism,[39] where the surface is homogeneous and competitive adsorption of N and As species on same group V surface sites occurs. From the study on co-pyrolysis of DMHy and TMG by Lee and Stringfellow,[27] we know DMHy and TMG firstly form an adduct and then decompose to produce one reactive N atom per adduct. Thus, the growth rate of GaAsN can be represented by a sum of fluxes and adsorption coefficients of Ga and the adduct of Ga and N. The formation and pyrolysis of the adduct can be expressed as:[27]

$$(CH_3)_3Ga + (CH_3)_2NNH_2 \rightarrow (CH_3)_3Ga{:}NH_2N(CH_3)_2 \quad (3.4)$$

$$(CH_3)_3Ga{:}NH_2N(CH_3)_2 \rightarrow (CH_3)_2GaNHN(CH_3)_2 + CH_3 \quad (3.5)$$

$$(CH_3)_2GaNHN(CH_3)_2 \rightarrow (CH_3)_2GaNH\bullet + N(CH_3)_2\bullet \tag{3.6}$$

$$N(CH_3)_2 \rightarrow CH_3NCH_2 + H\bullet \tag{3.7}$$

Assuming the TMG flux is fixed and group V precursors are fully decomposed at current growth temperatures, the flux of Ga–N adduct, J_{add}, is then dependent on the ratio of DMHy flux over the total group V flux, J_{DMHy}/J_V, and temperature T. It can be written with an Arrhenius temperature dependence as:

$$J_{add} = C_1 \cdot \frac{J_{DMHy}}{J_V} e^{E_1/kT} \tag{3.8}$$

where C_1 is a constant, E_1 is the activation energy for the adduct formation, and k is Boltzmann's constant. The adsorption coefficient of the adduct, K_{add}, can be also expressed with an Arrhenius temperature dependence:

$$K_{add} = C_2 \cdot e^{E_2/kT} \tag{3.9}$$

where C_2 is a constant, E_2 is the activation energy of the adduct adsorption. The growth rate of GaAsN, R_g, can be then expressed as:

$$\begin{aligned} R_g &\sim J_{add} \cdot K_{add} + (J_{TMG} - J_{add}) \cdot D_{TMG} \cdot K_{TMG} \\ &\sim D_{TMG} \cdot J_{TMG} \cdot K_{TMG} - (D_{TMG} \cdot K_{TMG} - K_{add}) \cdot J_{add} \end{aligned} \tag{3.10}$$

where K_{TMG} is the adsorption coefficient of TMG, D_{TMG} is the decomposition coefficient of TMG, which is assumed to be 1 when the temperature reaches 600°C. Replacing J_{add} and K_{add} with equations 3.8 and 3.9, R_g can be written as:

$$R_g \sim D_{TMG} \cdot J_{TMG} \cdot K_{TMG} - (D_{TMG} \cdot K_{TMG} - C_2 \cdot e^{E_2/kT}) \cdot C_1 \cdot \frac{J_{DMHy}}{J_V} e^{E_1/kT} \tag{3.11}$$

It was evidenced in the earlier study that K_{add} is very small (i.e., N incorporation efficiency is very low), so that it can be neglected. Then the growth rate can be simplified as:

$$R_g \sim D_{TMG} \cdot J_{TMG} \cdot K_{TMG} - D_{TMG} \cdot K_{TMG} \cdot C_1 \cdot \frac{J_{DMHy}}{J_V} e^{E_1/kT} \tag{3.12}$$

At low growth temperatures, D_{TMG} increases with increasing temperature while J_{add} decreases with increasing temperature, resulting in a higher growth rate of GaAsN. When the growth temperature is high enough (600°C in this study), TMG becomes fully decomposed, and J_{add} becomes very small and less sensitive to the temperature. Then the growth rate becomes almost independent on the growth temperature. It should also be mentioned that the first product in equation 3.12 is the growth rate of GaAs. Since the second product is always positive, thus the growth rate of GaAsN is lower than that of GaAs, as observed in the experiments.

The N incorporation x can be expressed as a rate equation:

$$x \sim \frac{J_{add} \cdot K_{add}}{R_g} = \frac{J_{add} \cdot K_{add}}{D_{TMG} \cdot J_{TMG} \cdot K_{TMG} - D_{TMG} \cdot K_{TMG} \cdot J_{add}} \tag{3.13}$$

Since J_{add} is much smaller than J_{TMG}, we neglect J_{add} in the denominator of equation 3.12 and write the N incorporation as:

$$x \sim \frac{C_1 \cdot C_2}{D_{TMG} \cdot J_{TMG} \cdot K_{TMG}} \cdot \frac{J_{DMHy}}{J_V} \cdot e^{(E_1+E_2)/kT} \tag{3.14}$$

It is obvious that the N incorporation is proportional to the DMHy/V ratio and inversely depends on the growth temperature, which is indeed observed in our experiments. The total of activation energies of $E_1 + E_2$ is also estimated from the experimental results.

3.3 Growth of GaAsN epilayers on AlGaAs

One desirable characteristic parameter for QW laser devices is to have a good high-temperature performance, i.e., to have a large band offset between the active QW layer and the barrier layer. Therefore, it is very attractive to grow (In)GaAsN QW sandwiched between the wide band-gap AlGaAs barrier layers. In this study, we investigate the possibility of growing GaAsN epilayers directly on AlGaAs layers.

3.3.1 Experimental

The experimental details are very similar to that described in section 3.2.1 except that a 200 nm thick AlGaAs layer was grown before the GaAsN epilayer. Both GaAs and AlGaAs layers were grown at 750°C, and GaAsN epilayers were all grown at 550°C. The Al content varies from 0.1 to 0.7, and flow rates of TMG, AsH_3, and DMHy were fixed during all growths. N content and structural properties were examined by DCXRD.

3.3.2 Results and discussion

Figure 3-9 shows the DCXRD rocking curves of as-grown GaAsN/AlGaAs structures with various Al contents from 10% to 70%. The main peak at 0 arc sec is from the GaAs substrate. GaAsN peaks are on the positive side of the main peak due to the

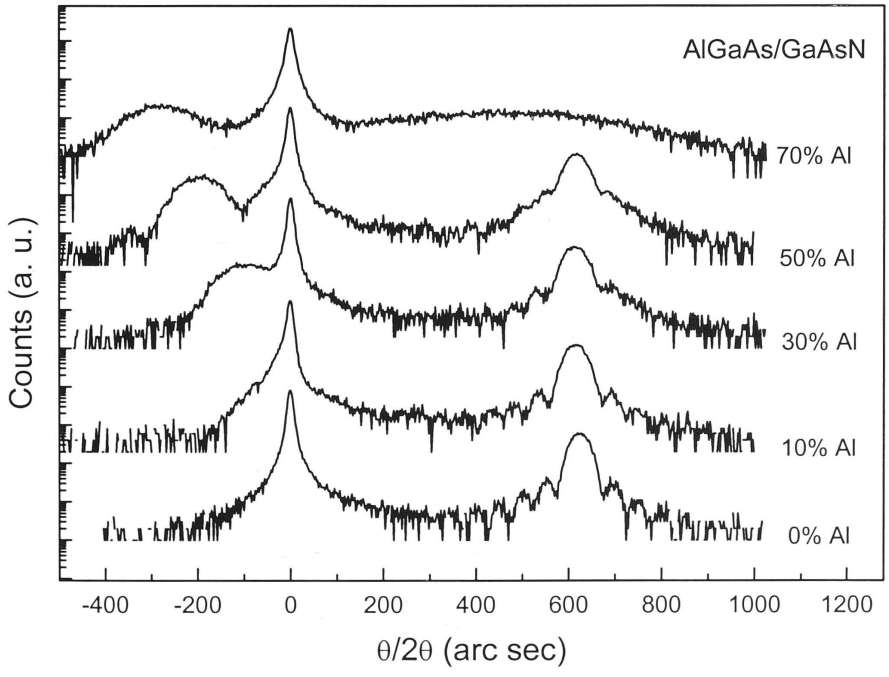

Fig. 3-9 DCXRD rocking curves of AlGaAs/GaAsN structures with different Al contents, the curves are shifted vertically for clarity.

tensile stain while AlGaAs peaks are on the negative side due to the compressive strain. Without AlGaAs, the narrow GaAsN peak and Pendelloesung fringes are clearly seen from the rocking curve, indicating high crystal quality and sharp interface. However, with increasing Al content, the GaAsN peak becomes broader and Pendelloesung fringes disappear, indicating that AlGaAs deteriorates the crystal quality of GaAsN, most likely due to the roughening of the interface between GaAsN/AlGaAs. This result is consistent with several reports from different groups,[40-42] where a significant QW-performance degradation and a rough surface were observed with increasing Al or by growing (In)GaAsN directly on AlGaAs layers. The GaAsN peak totally disappears when the N content reaches 70%, implying that most N atoms have had chemical reactions with Al and a poor crystalline quality was obtained. Based on these results, it is wise to avoid growing (In)GaAsN materials directly on Al-containing layers by MOCVD.

3.4 Growth of the GaAsN/GaAs QW

It has been well known that incorporation of a small amount of nitrogen in GaAs results in a dramatic decrease in the photoluminescence (PL) efficiency.[8,43-45] This is particularly true at room-temperature (only very weak PL could be observed from as-grown GaAsN/GaAs structures).[43-45] Although postgrowth annealing can significantly improve the PL efficiency,[43-45] it still remains a challenge to improve the PL properties of as-grown samples. Many methods have been tried to improve the PL properties of InGaAsN/GaAs QW structures, including the insertion of GaAsN or GaAsP strain-compensating layers (SCLs).[46-48] However, little effort has been made to improve the PL efficiency of GaAsN/GaAs QWs. Using migration-enhanced epitaxy, Hong et al. demonstrated an improved optical properties of GaAsN/GaAs QWs compared with that grown by conventional molecular beam epitaxy.[49] Nevertheless, in their case, all the PL spectra were collected at 10 K and the postgrowth annealing was still required to improve the PL intensity.

Here, an approach for improving the PL properties of the GaAsN/GaAs QW is demonstrated, in which multiple monolayer (ML) thick InAs SCLs are inserted into the GaAsN QW. Significant improvement of PL intensity has been achieved through this approach.

3.4.1 Experimental

The structures studied here were grown on SI-GaAs (100) substrates at 600 °C and 76 Torr, as schematically shown in figure 3-10. The nominal N content in GaAsN was about 2.8%. The reference QW (Ref. QW) structure shown in Fig. 3-10(a) is a single GaAsN/GaAs QW structure, in which a 5 nm thick GaAsN QW was sandwiched between a 400 nm GaAs buffer and a 100 nm GaAs cap/barrier layer. To compensate for the tensile strain experienced by the GaAsN QW, a strain-compensating QW (SCQW) structure was designed, in which three InAs MLs were evenly inserted in the 5 nm thick GaAsN QW, as shown in Fig. 3-10(b). After growth, both samples were cut into two pieces. One piece of each sample was annealed in a RTA furnace at 750 °C for 30 s in a flowing N_2 ambient. The microstructural quality of the two as-grown samples was evaluated by XTEM. The optical properties of all four samples were investigated using both low-temperature (10 K) PL and room-temperature (RT) PL.

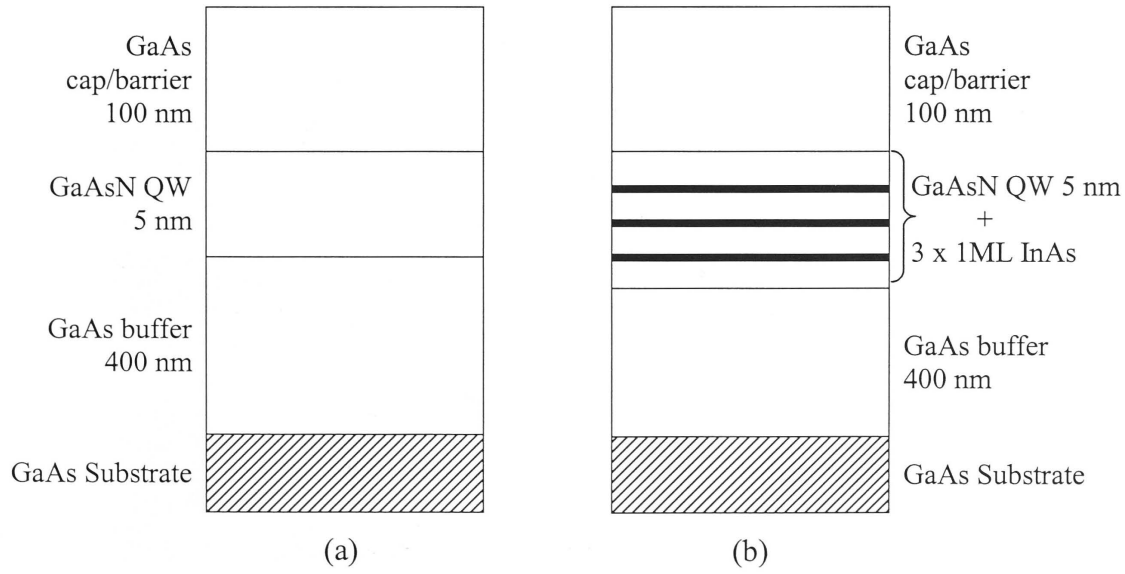

Fig. 3-10 Schematic of (a) the reference quantum well (Ref. QW) structure and (b) the InAs strain-compensating quantum well (SCQW) structure.

3.4.2 Results and discussion

Figures 3–11(a) and 3–11(b) are XTEM images of the as-grown structures of Ref. QW and SCQW, respectively, showing the high quality of the QW structures (dislocation free). It is important to note that the contrast shown in Fig. 3–11 is mainly due to the misfit strain (short white lines indicate the interface between the QW and the GaAs buffer/capping layer). In Fig. 3–11(a), the GaAsN QW is clearly seen, indicating the QW experiencing a certain degree of strain with respect to the GaAs buffer/capping layers. In Figure 3–11(b), the contrast of GaAsN disappears, meaning that the misfit strain between the GaAsN and GaAs becomes too small to become apparent in the TEM image. On the other hand, the InAs MLs showed a contrast, indicating that these three layers experience a sufficient misfit strain. From this investigation, we may conclude that the InAs MLs are able to compensate for the misfit strain between GaAsN and GaAs.

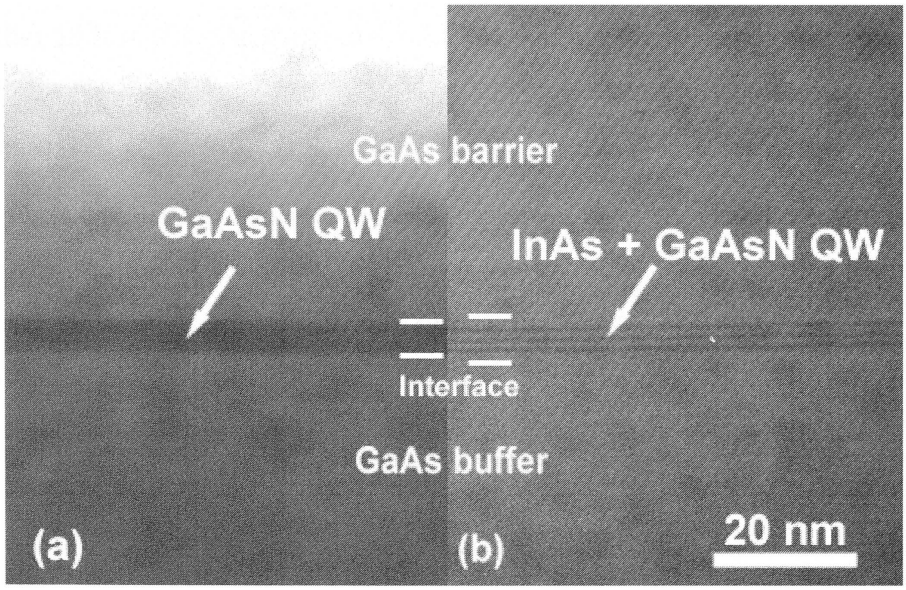

Fig. 3-11 Bright-field cross-section TEM images of (a) reference QW and (b) strain-compensated QW with three periods of InAs monolayer. Two short white lines indicate the interface between the QW and the GaAs layers.

To assess optical properties of these QW structures, PL measurements were carried out at both 10K and RT. Figures 3-12(a) and 3-12(b) show PL spectra taken from 10K and RT, respectively. The following features can be clearly seen in Fig. 3-12(a) and 3-12(b):

(i) In all cases, the insertion of InAs SCL resulted in a significant improvement of PL intensity (more than one order of magnitude higher at RT) and a blueshift of PL peak energy (about 65 meV) compared with its corresponding Ref. QW. It is worth noting that no PL emission was detected from the as-grown Ref. QW at RT [Fig. 3-12(b)].

(ii) At RT in the annealed samples, the InAs SCL reduced the full width at half maximum of PL spectrum from 55 meV (Ref. QW) to 35 meV (SCQW).

(iii) The postgrowth annealing process led to different PL behaviour for Ref. QW and SCQW. In the case of the Ref. QW, RTA improved the PL intensity significantly (by more than one order of magnitude relative to that of the as-grown sample at 10 K and recovered the PL emission at RT). Whereas in the case of the SCQW, no such improvement of PL intensity was achieved after RTA at either 10 K or RT. Furthermore, RTA blueshifted the PL peak wavelength of the Ref. QW by about 9 nm at 10 K, whereas no blueshift was observed for the SCQW.

It is clear from these results that the insertion of InAs MLs significantly improved the optical properties of the GaAsN QW structure. In addition, the insertion of InAs SCLs substantially improved the overall optical uniformity of the QW structure, where the variation of the PL peak position was about ±3 nm for the SCQW structure across the 2-inch diameter wafer, compared with about ±15 nm for the Ref. QW structure. The explanation of how the InAs monolayers could affect the PL properties of QW structures could be as follows:

(i) They compensate for the tensile strain experienced by a GaAsN QW and, therefore, reduce the strain and composition fluctuations, hence the improved optical properties and uniformity.

(ii) They reduce the tensile strain experienced by the GaAsN QW or convert it to a compressive strain, contributing to the blueshift of the PL emission wavelength.

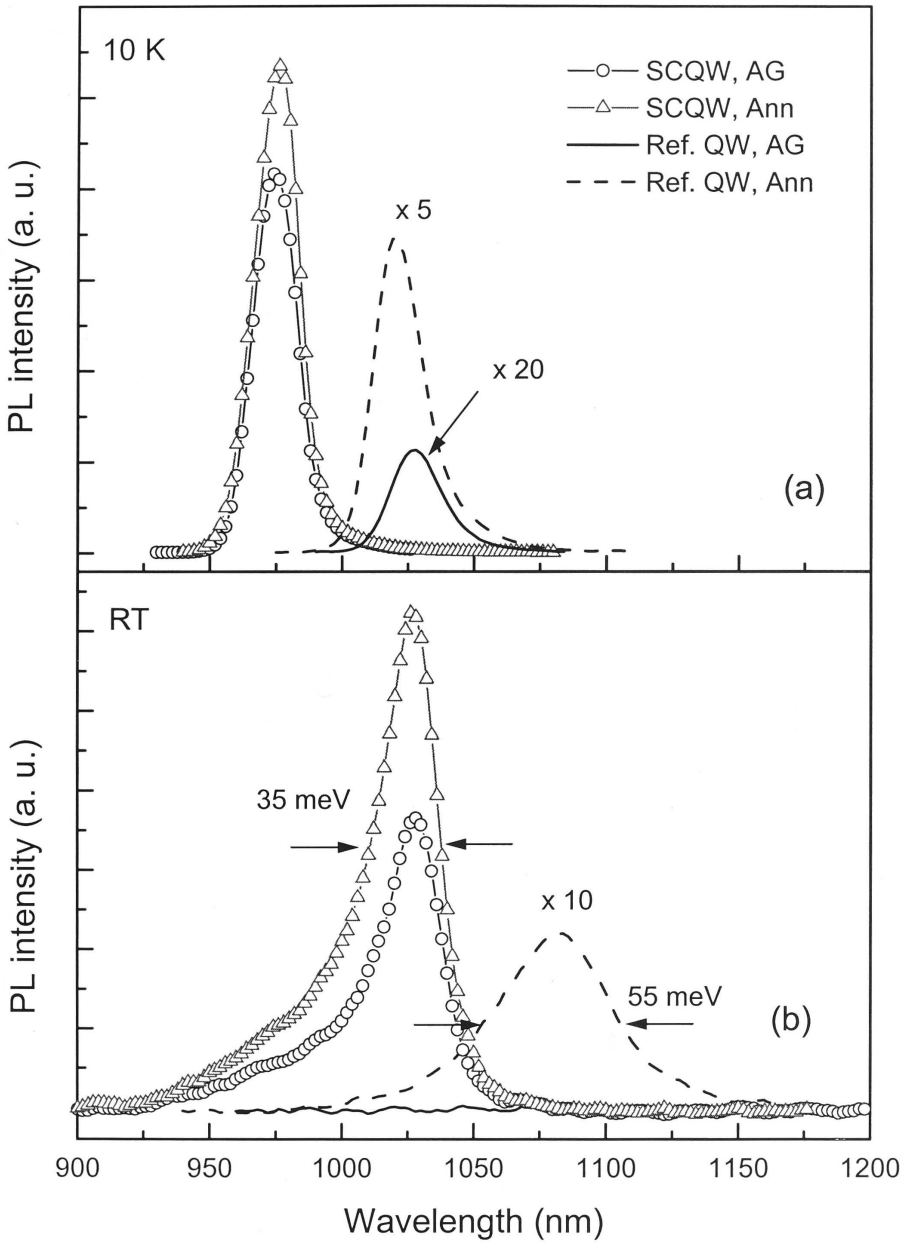

Fig. 3-12 (a) Low-temperature (10 K) and (b) room-temperature (RT) PL spectra from the as-grown (AG) and annealed (Ann) strain-compensated QWs (SCQW) and reference GaAsN/GaAs QWs (Ref. QW).

(iii) They could reduce the N content in the GaAsN QW and result in a further blueshift of the PL emission wavelength, which is similar to the reports by many groups that N incorporation in (In)GaAs is reduced with increasing In concentration during MOCVD growth.[7,8,50,51] Especially in Ref. 7, N incorporation in a GaAs/InAs superlattice was found to be about 4 orders of magnitude lower than that in a normal GaAsN epilayer. If the PL blueshift was solely caused by the reduction of N incorporation, it is estimated that the N content is reduced by 0.5% (from 2.8% to 2.3%) in the InAs-inserted GaAsN/ GaAs QW.

In addition to the above factors, there might be some other effects associated with the insertion of InAs MLs, such as changes of chemical bonds and carrier confinement. Overall, we suggest that the improvements of the PL efficiency and uniformity are mainly due to the strain compensation, and the blue shift of PL emission wavelength might be due to the strain compensation and/or In-induced reduction of N incorporation. It is also worth mentioning here that in spite of the In-induced reduction of N incorporation (if any), similarly as observed here, the PL intensity in this SCQW structure was significantly higher than that of the reference GaAsN (2.3% N)/GaAs QW either at RT or LT (spectra are not shown).

In order to clarify that the strong PL emission from the SCQW structure was not due to the carrier confinement in InAs MLs, we grew two GaAsN epilayer samples under the same growth conditions. One structure consisted of a 200 nm thick GaAsN layer and the other consisted of the same thickness GaAsN layer, but with three InAs MLs inserted. For both samples, PL emissions with same peak wavelength were observed at 10 K after the postgrowth annealing. This suggests that the quantum confinement effects in InAs MLs, if any, are negligible.

In summary, the approach of the insertion three InAs MLs in a GaAsN QW shows a significant improvement of the PL properties and uniformity of the GaAsN/GaAs QW, and blueshifts the PL emission peak. We suggest that the improvements of the PL efficiency and uniformity are mainly due to the strain compensation, and the blue shift of PL emission might be due to the strain compensation and/or In-induced reduction of N incorporation.

3.5 Growth of InGaAsN QW and QD structures

Due to the difficulty to incorporate high concentration of N into GaAs and the negative impact of N on the optical properties of the materials, it is impractical to achieve 1.3 μm PL emission from the GaAsN QW or epilayers. Fortunately incorporation of a few percent N into InGaAs materials not only reduces the lattice mismatch between InGaAs and GaAs, but also results in a significant narrowing of the bandgap energy, which makes this quaternary alloy InGaAsN a very promising candidate for the long-wavelength (1.3 - 1.55 μm) optoelectronic devices. In this work, the (In)GaAsN/GaAs QW structure was first grown on GaAs. However, in addition to the QW emission, a second longer-wavelength PL peak was observed from the InGaAsN/GaAs QW structures, probably due to the phase segregation which was reported in the GaAsN growth in its early stage[20-22], or the deep-level transitions caused by the N incorporation. The growth of InGaAsN QDs on GaAs was then investigated. It is well known self-organised coherently strained QDs could be formed during the epitaxial growth in the Stranski-Krastanow mode when the thickness of a strained layer exceeds the critical value. These QDs have novel physical properties and can overcome the strain limitation of the QW structures. In the past decade or so, In(Ga)As (QD) structures have been extensively studied for the GaAs-based 1.3 μm laser devices and have shown many advantages than the conventional InGaAsP/InP QW laser devices[52-54] However, the growth of InGaAsN QDs on GaAs has only been reported in a very few publications.[55-58] In the following sections, InGaAsN QW and QDs grown on GaAs substrates are presented.

3.5.1 Experimental

Both the InGaAsN/GaAs QW and QD structures used in this study were grown on SI-GaAs (100) substrates at 76 Torr. First, a 500 nm GaAs buffer was deposited at 650 °C. The temperature was then lowered to 600, 550, or 525 °C under AsH_3 flow prior to the growth of an InGaAsN layer with a deposition thickness of 5 nm. Growth of the InGaAsN layer was commenced by injecting TMG, TMI, and DMHy simultaneously into the MOCVD reactor. The nominal In and N mole fraction for the InGaAsN is 30–40% and 2–4%, respectively. The nominal In and N compositions were determined from similar InGaAs/GaAs QW and the GaAsN epilayer samples grown under

the same conditions, respectively. After growth, AFM, PL, or TEM were carried out on selected samples. For samples used in the atomic force microscopy (AFM) study, growths were terminated after the InGaAs(N) layer. For samples used for PL and XTEM studies, immediately after the InGaAs(N) layer, the temperature was ramped to 600 °C whilst depositing a 200 nm GaAs capping layer.

3.5.2 Results and discussion

InGaAsN/GaAs QW

Figure 3-13 shows the low-temperature (10 K) PL spectrum of an as-grown $In_{0.3}Ga_{0.7}As_{0.98}N_{0.02}$/GaAs QW sample grown at 600 °C. The PL spectrum of a reference $In_{0.3}Ga_{0.7}As$/GaAs QW sample is also shown in Fig. 3-13. Two emissions were clearly observed from the InGaAsN sample at ~1005 nm and ~1090 nm, respectively. The broad longer-wavelength PL emission could be due to the N segregation during

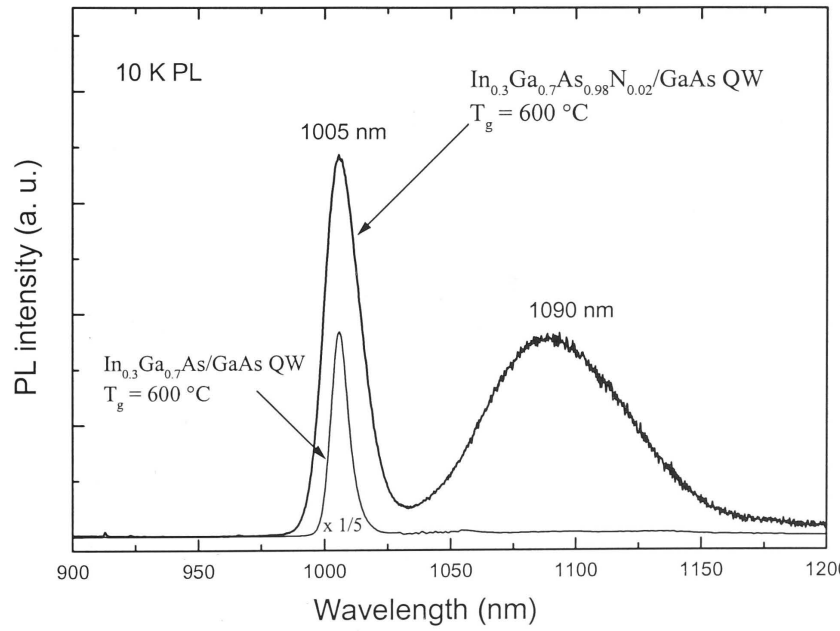

Fig. 3-13 Low-temperature (10 K) PL spectra of a 5 nm $In_{0.3}Ga_{0.7}As_{0.98}N_{0.02}$/GaAs and a 5 nm reference $In_{0.3}Ga_{0.7}As$/GaAs QW structures grown at 600 °C. The PL intensity of the $In_{0.3}Ga_{0.7}As$/GaAs QW sample is reduced by a factor of 5 for clarity.

growth, or the transitions involving N-related defects/clusters. The sharp PL peak (1005 nm) is coincident with the PL peak of the reference InGaAs/GaAs QW sample, implying that this emission is most likely from the InGaAs phase with negligible, if any, N incorporation. Since N atoms have a very low sticking coefficient on the GaAs surface, they tend to segregate, especially at high growth temperatures. On the other hand, as In atoms have a much higher sticking coefficient, InGaAs will form more readily when TMG, TMI, and DMHy are injected simultaneously into the reactor. Therefore, at 600 °C, which is a relatively high temperature for growth of InGaAsN, the InGaAs phase will form in priority and N atoms tend to segregate. The microstructural quality of the above layer was further examined using XTEM, as shown in Fig. 3–14. The XTEM image was obtained under the bright-field mode at g[002] direction. It is important to note that the contrast shown in Fig. 3–14 is mainly due to misfit strain (two short white lines on the image indicate the interface between QW and GaAs). As seen from Fig. 3–14, the image does not reveal any misfit dislocations and a reasonably high hetero-interface quality is observed. However, no phase segregation can be seen from this image. A higher resolution of the microstructural analysis is needed to resolve this issue.

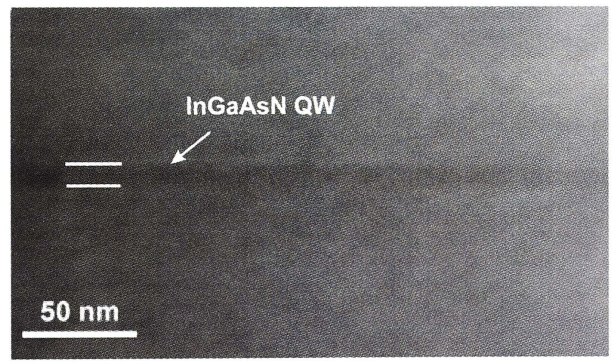

Fig. 3-14 Dark field XTEM image (g = 002) of the interfacial region of a 5 nm thick $In_{0.3}Ga_{0.7}As_{0.98}N_{0.02}$/GaAs QW structure grown at 600 °C.

To push the PL emission to longer wavelength, the In and N contents were increased to 40% and 4%, respectively. Meanwhile, to suppress the possible phase segregation, the growth temperature of InGaAsN was reduced to 525 °C. The low-temperature (77 K) PL spectrum of such an as-grown sample is shown in Fig. 3–15. It is clearly seen that the PL peak wavelength was extended to 1328 nm at 77 K with a

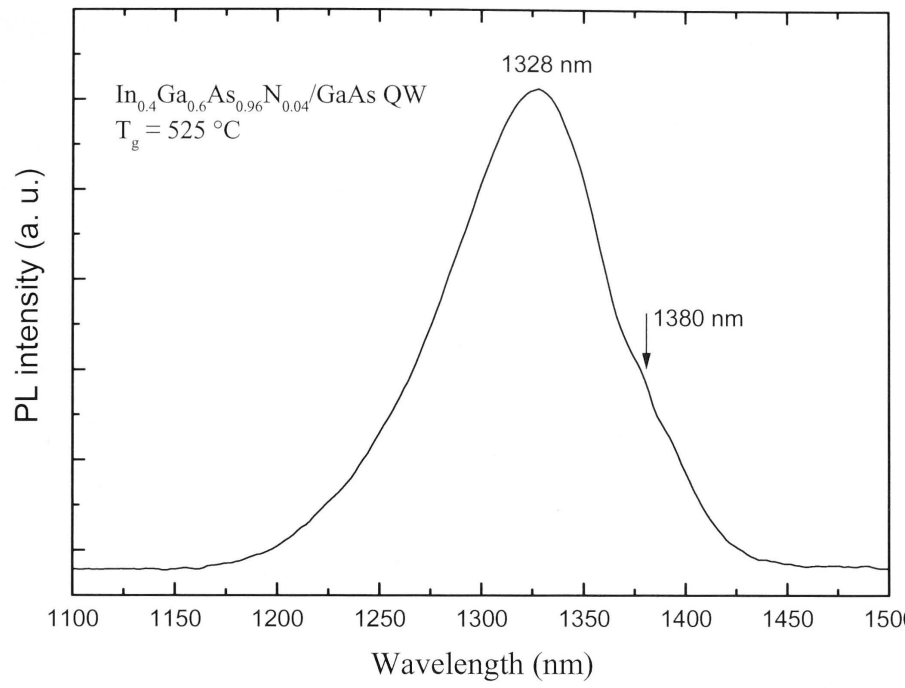

Fig. 3-15 Low-temperature (77 K) PL spectrum of a 5 nm $In_{0.4}Ga_{0.6}As_{0.96}N_{0.04}$/GaAs QW structure grown at 525 °C.

shoulder emission at 1380 nm. It is worth noting that no RT PL was observed from this sample. These features can be well explained by its microstructure, as seen from a XTEM image in Fig. 3–16. The XTEM was carried out in the same condition as that of the former InGaAsN QW sample. Compared with the former $In_{0.3}Ga_{0.7}As_{0.98}N_{0.02}$/GaAs

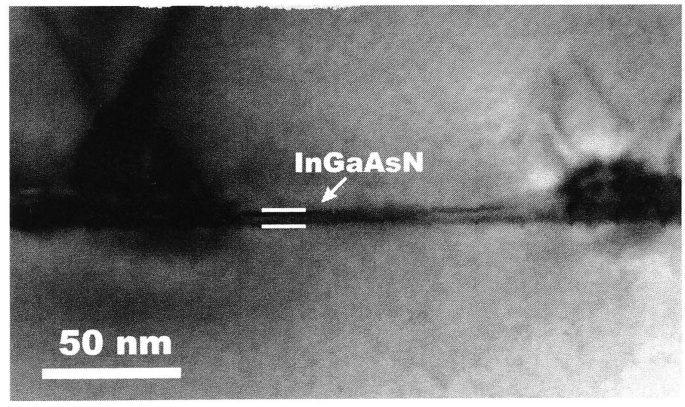

Fig. 3-16 Dark field XTEM image (g = 002) of the interfacial region of a 5 nm thick $In_{0.4}Ga_{0.6}As_{0.96}N_{0.04}$/GaAs QW structure grown at 525 °C.

QW sample grown at 600 °C(Fig. 3-14), this image (Fig. 3-15) has a darker QW region, indicating the larger lattice mismatch due to the higher In composition. The most important feature of Fig. 3-16 is the dot-like dark regions in the QW surrounded by dislocations extending to the sample's surface, presumably due to the N and/or In accumulation which will result in a longer-wavelength PL emission. These features in TEM image can readily account for the absence of RT PL and the shoulder emission at the 77 K PL spectrum (Fig. 3-15).

From the dot-like structure observed, it was promising that by further optimising the growth conditions, self-assembled QDs could be formed. Since QD lasers devices were anticipated to have many advantages than the QW ones, such as largely extended emission wavelength, decreased transparency current density, increased material and differential gain, and a large characteristic temperature T_0,[59,60] growth of the InGaAsN QDs on GaAs was then focused in the next sections.

InGaAsN QDs

Figure 3-17 shows an AFM image of the InGaAsN QDs grown on GaAs. The InGaAsN layer was grown at 550 °C with a 12-monolayer (12-ML) thickness. As seen from Fig. 3-17, the dots are distributed quite homogeneously with an average height about 5 nm and an average lateral size about 35 nm. The density of dots is about 5 x 10^{10} cm^{-2}.

The effects of N incorporation in InGaAs are two folds. One is to reduce the lattice mismatch between InGaAs and GaAs. On the other hand, since the atomic radius and the electronegativity values are much different between N and As, introduction of N may increase the local strain around N atoms. The 2D to 3D growth transition is then more driven by this 'local strain'. Moreover, N atoms may change the surface potential and decrease the migration length due to their strong bond. As a result, InGaAsN tends to form dots during the growth.

Figure 3-18 shows a RT PL spectrum of an as-grown InGaAsN QD sample. The spectrum is quite symmetrical with a peak wavelength at about 1.32 μm, indicating the reasonably good quality of the QDs. Due to the complexity of the MOCVD growth of the QD structures, detailed study on growth parameters for the InGaAsN QDs is needed in the future to obtain the optimum growth condition and to extend the PL emission to longer wavelength.

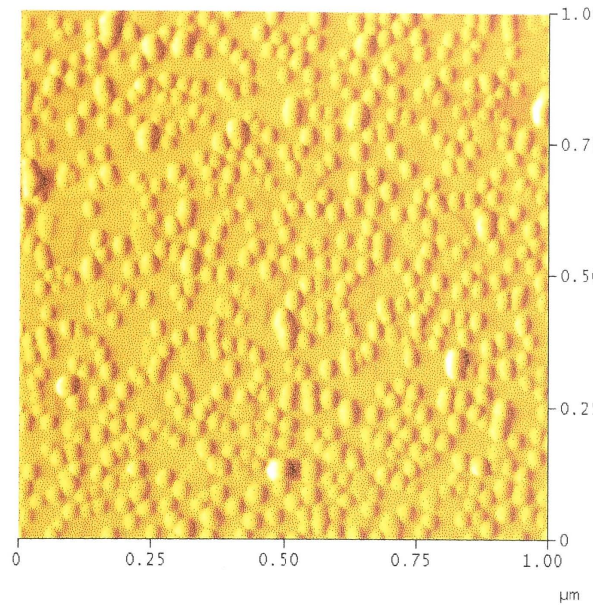

Fig. 3-17 The atomic force microscopy (AFM) image (1 x 1 μm^2) of InGaAsN QDs grown on GaAs.

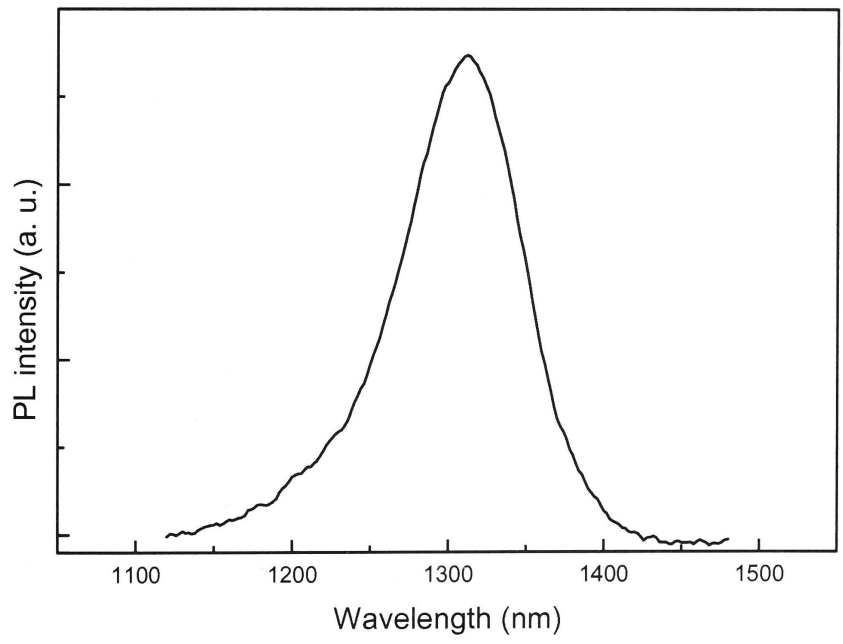

Fig. 3-18 RT PL spectrum of an as-grown InGaAsN QD sample.

3.6 Conclusion

MOCVD growth of the GaAsN epilayers on GaAs and AlGaAs, GaAsN QW, and InGaAsN QW and QDs have been systematically investigated. Mass-transport limited and kinetically limited growth regimes for GaAsN epilayers have been identified. The growth temperature and the fractional DMHy molar flow, DMHy/V, are identified as key factors that affect the N incorporation in GaAsN. Precise control of N content in the range from 0.1% to 4.5% can be obtained by using the appropriate growth conditions. A kinetic growth model is proposed to explain the growth process of the GaAsN epilayers.

It was found that growing GaAsN directly on AlGaAs has a negative effect on the crystalline quality of the GaAsN layer. This effect becomes more prominent for the higher Al content alloys due to the direct reaction between Al and N. Insertion of 3 InAs MLs in GaAsN QW significantly improved the PL efficiency of the QW and blue-shifted the PL peak wavelength, which might be due to the strain compensation and/or In-induced reduction of N content. Finally, InGaAsN QDs were successfully grown on GaAs by MOCVD with a RT PL emission at 1.32 μm, which has a great significance in developing the long-wavelength optoelectronic devices.

References

1 G. B. Stringfellow, J. Electrochem. Soc. **119,** 1780 (1972).

2 G. B. Stringfellow and G. Hom, J. Electrochem. Soc. **124,** 1806 (1977).

3 M. Weyers, M. Sato, and H. Ando, Jpn. J. Appl. Phys. Part 2 **31,** L853 (1992).

4 M. Weyers and M. Sato, Appl. Phys. Lett. **62,** 1396 (1993).

5 M. Kondow, K. Uomi, K. Hosomi, and T. Mozume, Jpn. J. Appl. Phys. Part 2 **33,** L1056 (1994).

6 M. Kondow, K. Uomi, A. Niwa, T. Kitatani, S. Watahiki, and Y. Yazawa, Jpn. J. Appl. Phys., Part 1 **35,** 1273 (1996).

7 D. J. Friedman, J. F. Geisz, S. R. Kurtz, J. M. Olson, and R. Reedy, J. Cryst. Growth **195,** 438 (1998).

8 R. Bhat, C. Caneau, L. Salamanca-Riba, W. Bi, and C. Tu, J. Cryst. Growth **195,** 427 (1998).

9 D. J. Friedman, A. G. Norman, J. F. Geisz, and S. R. Kurtz, J. Cryst. Growth **208,** 11 (2000).

10 J. Toivonen, T. Hakkarainen, M. Sopanen, and H. Lipsanen, J. Cryst. Growth **221,** 456 (2000).

11 H. Dumont, L. Auvray, Y. Monteil, and J. Bouix, Mater. Sci. Eng. B **84,** 258 (2001).

12 S. Kurtz, J. F. Geisz, B. M. Keyes, W. K. Metzger, D. J. Friedman, J. M. Olson, A. J. Ptak, R. R. King, and N. H. Karam, Appl. Phys. Lett. **82,** 2634 (2003).

13 Y. Qiu, S. A. Nikishin, H. Temkin, V. A. Elyukhin, and Y. A. Kudriatsev, Appl. Phys. Lett. **70,** 3242 (1997).

14 K. Takeuchi, T. Miyamoto, T. Kageyama, F. Koyama, and K. Iga, Jpn. J. Appl. Phys., Part 1 **37,** 1603 (1998).

15 C. L. Aardahl, H. K. Yun, T. P. Pearsall, J. W. Rogers, M. Qian, H. Fong, and M. Sarikaya, Thin Solid Films **344,** 646 (1999).

16 Y. Fujimoto, H. Yonezu, K. Momose, A. Utsumi, and Y. Furukawa, J. Cryst. Growth **227,** 491 (2001).

17 *Bonds and Bands in Semiconductors,* edited by J. C. Phillips, A. M. Alper, J. L. Margrave, and A. S. Nowick (Academic Press, New York, 1973).

18 I. Ho and G. B. Stringfellow, J. Cryst. Growth **178,** 1 (1997).

19 S. H. Wei and A. Zunger, Phys. Rev. Lett. **76,** 664 (1996).

[20] Y. Qiu, S. A. Nikishin, H. Temkin, V. A. Elyukhin, and Y. A. Kudriatsev, Appl. Phys. Lett. **70,** 2831 (1997).

[21] J. Salzman and H. Temkin, Mater. Sci. Eng. B **50,** 148 (1997).

[22] C. T. Foxon, T. S. Cheng, S. V. Novikov, D. E. Lacklison, L. E. Jenkins, D. Johnston, J. W. Orton, S. E. Hooper, N. Baba-Ali, T. L. Tansley, and V. V. Tret'yakov, J. Cryst. Growth **150,** 892 (1995).

[23] A. Ougazzaden, Y. Lebellego, E. V. K. Rao, M. Juhel, L. Leprince, and G. Patriarche, Appl. Phys. Lett. **70,** 2861 (1997).

[24] A. J. Ptak, S. Kurtz, C. Curtis, R. Reedy, and J. M. Olson, J. Cryst. Growth **243,** 231 (2003).

[25] S. Kurtz, R. Reedy, G. D. Barber, J. F. Geisz, D. J. Friedman, W. E. McMahon, and J. M. Olson, J. Cryst. Growth **234,** 318 (2002).

[26] E. Bourret-Courchesne, Q. Ye, D. W. Peters, J. Arnold, M. Ahmed, S. J. C. Irvine, R. Kanjolia, L. M. Smith, and S. A. Rushworth, J. Cryst. Growth **217,** 47 (2000).

[27] R. T. Lee and G. B. Stringfellow, J. Electron. Mater. **28,** 963 (1999).

[28] G. Li, PhD Thesis, The Australian National University, 1996.

[29] H. H. Tan, PhD Thesis, The Australian National University, 1996.

[30] Y. Qiu, C. Jin, S. Francoeur, S. A. Nikishin, and H. Temkin, Appl. Phys. Lett. **72,** 1999 (1998).

[31] C. Jin, S. A. Nikishin, V. I. Kuchinskii, H. Temkin, and M. Holtz, J. Appl. Phys. **91,** 56 (2002).

[32] A. Moto, S. Tanaka, N. Ikoma, T. Tanabe, S. Takagishi, M. Takahashi, and T. Katsuyama, Jpn. J. Appl. Phys. Part 1 **38,** 1015 (1999).

[33] P. R. Chalker, H. Davock, S. Thomas, T. B. Joyce, T. J. Bullough, R. J. Potter, and N. Balkan, J. Cryst. Growth **233,** 1 (2001).

[34] H. Dumont, L. Auvray, J. Dazord, Y. Monteil, C. Bondoux, and G. Patriarche, J. Cryst. Growth **248,** 441 (2003).

[35] H. Dumont, L. Auvray, Y. Monteil, C. Bondoux, L. Largeau, and G. Patriarche, Appl. Phys. Lett. **80,** 2460 (2002).

[36] S. Takagi, Acta Cryst. **15,** 1311 (1962).

[37] S. Takagi, J. Phys. Soc. Jpn. **26,** 1239 (1969).

[38] D. Taupin, Bull. Soc. Fr. Miner. Crist. **87,** 469 (1964).

[39] I. Langmuir, J. Am. Chem. Soc. **40,** 1361 (1918).

[40] P. Sundgren, C. Asplund, K. Baskar, and M. Hammar, Appl. Phys. Lett. **82,** 2431 (2003).

[41] S. Sato and S. Satoh, J. Cryst. Growth **192,** 381 (1998).

[42] M. Kawaguchi, E. Gouardes, D. Schlenker, T. Kondo, T. Miyamoto, F. Koyama, and K. Iga, Electron. Lett. **36,** 1776 (2000).

[43] E. V. K. Rao, A. Ougazzaden, Y. Lebellego, and M. Juhel, Appl. Phys. Lett. **72,** 1409 (1998).

[44] S. Francoeur, G. Sivaraman, Y. Qiu, S. Nikishin, and H. Temkin, Appl. Phys. Lett. **72,** 1857 (1998).

[45] L. H. Li, Z. Pan, W. Zhang, Y. W. Lin, Z. Q. Zhou, and R. H. Wu, J. Appl. Phys. **87,** 245 (2000).

[46] N. Tansu, A. Quandt, M. Kanskar, W. Mulhearn, and L. J. Mawst, Appl. Phys. Lett. **83,** 18 (2003).

[47] N. Tansu, J. Y. Yeh, and L. J. Mawst, Appl. Phys. Lett. **83,** 2512 (2003).

[48] L. F. Bian, D. S. Jiang, S. L. Lu, J. S. Huang, K. Chang, L. H. Li, and J. C. Harmand, J. Cryst. Growth **250,** 339 (2003).

[49] Y. G. Hong and C. W. Tu, J. Cryst. Growth **242,** 29 (2002).

[50] T. Hakkarainen, J. Toivonen, M. Sopanen, and H. Lipsanen, J. Cryst. Growth **234,** 631 (2002).

[51] F. Höhnsdorf, J. Koch, C. Agert, and W. Stolz, J. Cryst. Growth **195,** 391 (1998).

[52] O. B. Shchekin and D. G. Deppe, Appl. Phys. Lett. **80,** 3277 (2002).

[53] A. Patane, M. G. Alessi, F. Intonti, A. Polimeni, and M. Capizzi, J. Appl. Phys. **83,** 5529 (1998).

[54] K. Nishi, H. Saito, S. Sugou, and J.-S. Lee, Appl. Phys. Lett. **74,** 1111 (1999).

[55] M. Sopanen, H. P. Xin, and C. W. Tu, Appl. Phys. Lett. **76,** 994 (2000).

[56] K. C. Yew, S. F. Yoon, Z. Z. Sun, and S. Z. Wang, J. Cryst. Growth **247,** 279 (2003).

[57] T. Hakkarainen, J. Toivonen, M. Sopanen, and H. Lipsanen, Appl. Phys. Lett. **79,** 3932 (2001).

[58] S. Makino, T. Miyamoto, T. Kageyama, N. Nishiyama, F. Koyama, and K. Iga, J. Cryst. Growth **221,** 561 (2000).

[59] Y. Arakawa and H. Sakaki, Appl. Phys. Lett. **40,** 939 (1982).

[60] M. Asada, M. Miyamoto, and Y. Suematsu, IEEE J. Quantum Electron. **22,** 1915 (1986).

CHAPTER 4

Optical properties, microstructural properties, and band structures of GaAsN

4.1 Introduction

It has been reported by many groups that (In)GaAsN-related low-temperature PL emission shows a very asymmetric line shape with a sharp high-energy cutoff and an exponential low-energy tail.[1-4] Most authors have ascribed the origin of low-temperature PL emission to the recombination of localised excitons, and the origin of high-temperature PL emission to the recombination between delocalised electrons and holes.[1-3] In this chapter, the question of the mechanism of low-temperature radiative recombination in GaAsN epilayers is re-examined using high-resolution time-resolved PL (TRPL) measurements. Moreover, the band structure and bandgap bowing effects of (In)GaAsN alloy materials have attracted intense theoretical studies. In this chapter, these two topics are investigated from the evolution of low-temperature (10 K) PL peak wavelength as a function of N content in GaAsN, and the temperature dependence of PL emissions in different GaAsN epilayers.

It is also well known that increasing the nitrogen concentration in (In)GaAsN alloy materials steeply degrades the PL intensity.[5-7] The reason may be due to (i) phase separation or the local compositional inhomogeneity due to the large miscibility gap between GaN and (In)GaAs, (ii) large concentration of O, C, or H incorporation alongside N incorporation, and (iii) accumulation of point-defects, such as group-V vacancies. However, an enhancement of PL intensity in a thick (500 nm) and high N content (2.8%) GaAsN sample was observed compared with lower-N-content samples. More interestingly, an unusual random lasing was observed from this sample. This random lasing nature was characterised and confirmed by optical measurement techniques. To understand the origin of this enhancement on PL intensity and lasing scenario, the surface morphology and microstructure of this sample were investigated by using AFM, SEM and XTEM.

4.2 Experimental

The GaAsN epilayers used in this chapter were grown on SI-GaAs (100) at 76 Torr with an initial GaAs buffer of 0.25 μm grown at 600 °C. GaAsN epilayers were grown at temperatures from 525 to 600 °C with different thicknesses depending on the N con-

tent, for example, 500 nm for low N concentration (< 3.0% N) and 150 nm for high N concentration (> 3.0% N). Various techniques described in Chapter 2, such as PL, TRPL, XTEM and SEM, were used to characterise the samples. In order to observe reasonable PL emission from GaAsN epilayers, these samples were annealed at 750°C for 30 s in a flowing N_2 ambient, which is the optimum annealing condition in this thesis. GaAs proximity capping was used to minimise the As preferential evaporation during annealing.

4.3 Results and discussion

4.3.1 Nature of radiative recombination in GaAsN system

The low-temperature (10K) PL spectra of the annealed GaAsN epilayers with different N contents are shown in Fig. 4-1. The growth temperature was 600 °C for all samples except the one with 4.5%N, which was grown at 525 °C. The thickness was 500 nm for samples with N content ≤ 2.8% and 150 nm for the remaining two samples (≥ 3.2% N). As seen from Fig. 4-1, the PL peak wavelength exhibits a strong shift to

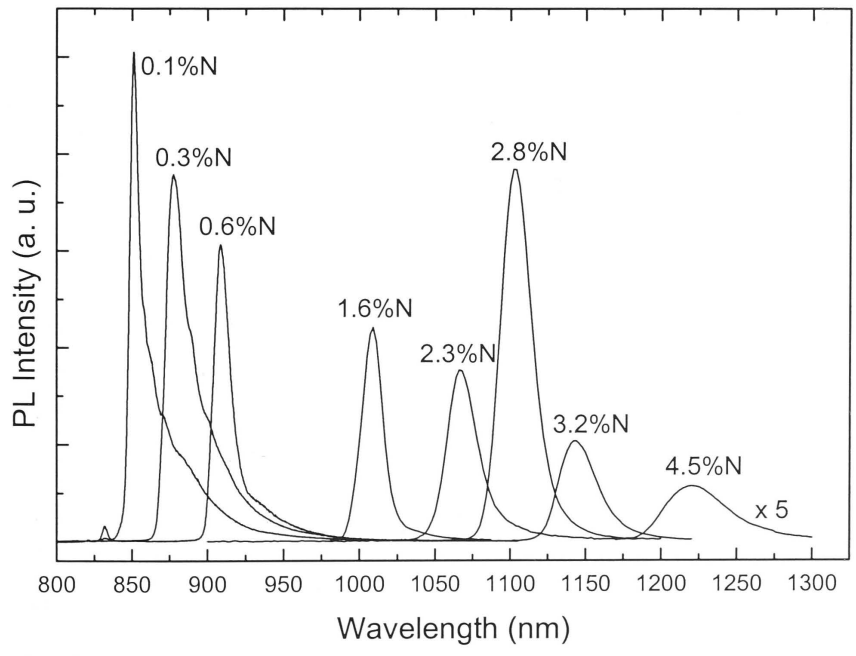

Fig. 4-1 Low-temperature (10 K) photoluminescence spectra of GaAsN epilayers with different N contents.

longer wavelength with increasing N content, which is consistent with the large band-gap bowing effects of this alloy system. Also all PL spectra exhibit an asymmetric shape with a sharp high-energy cut-off and an exponential low-energy tail, as observed by various groups.[1-3] The long low-energy tail is more prominent in the samples with a low N content (0.3 - 1% N) than that in samples with a higher N content (> 1.0% N), inferring that the density of states or band structure changes as a function of N content (to be discussed later).

The unusual luminescence feature of the exponential low-energy tail has been explained in terms of excitons localised by potential fluctuations at the band edges, i.e., localised excitons (LE).[1,2] The localised nature of the carriers assumed in this model is compatible with the observed blue shift in the excitation intensity dependence and the unusual temperature dependence of the PL. The assumption that the recombination is due to localised excitons, as opposed to localised electrons and holes, was based on the observation that the temporal decay of the PL emission can be fitted with a single exponential function.[1,2] Radiative recombination between spatially separated (localised) electrons and holes would result in strongly non-exponential decay. Since the low-temperature PL decay was found to exhibit an exponential function, it was assumed that the recombination is excitonic in nature. However, recombination between localised electrons (holes) and *delocalised* holes (electrons) would also lead to luminescence decay with a single (effective) time constant. The PL decay measurements alone therefore, cannot distinguish between these two models.

One method capable of differentiating between excitonic and electron–hole recombination is high-resolution TRPL, and, in particular, to measure the luminescence risetime. Excitonic recombination in III–V compounds at low temperatures is known to have the PL emission with a very long risetime,[8,9] while electron–hole recombination is much shorter.[10] The risetime of free exciton luminescence in epitaxial (bulk) GaAs was recently measured to be of the order of 1 ns,[8] while that in GaAs quantum wells was found to be somewhat shorter but still of the order of 300–400 ps.[9] It was shown[8] that the very long risetime is the result of several gradual processes including exciton formation (from free electrons and holes), relaxation of the hot excitons via the acoustic phonon emission, and the scattering of the luminescing excitons into the $k \approx 0$ exciton states, which are the only ones observable by optical techniques.[9] Thus, any exciton-related luminescence in GaAsN should exhibit a PL signal with a similar long risetime.

In contrast, electron-hole recombination is expected to have short luminescence risetime because none of the aforementioned time-consuming processes are involved. In GaAs epilayers, for example, the PL risetime at room temperature is of the order of 10-20 ps.[10]

Therefore, to be able to correctly describe the nature of the recombination process in GaAsN, it is essential to determine the risetime of the PL signal. For this analysis, we define the risetime as the time required for the luminescence to reach the maximum intensity.[9] As described in Chapter 2, the PL upconversion technique was used to accurately measure the PL risetime in our samples. Figure 4-2 shows the time evolution of the 10 K PL of a GaAsN epilayer sample with 2.3% N in the first 60 ps after excitation (the PL spectrum of this sample is shown in the inset). The luminescence risetime of this sample is about 25 ps. Similar risetime was measured for all GaAsN epilayer samples investigated here, irrespective of the nitrogen content (between 0.1% and 2.8%), the measurement wavelength (within the emission band), and the measurement

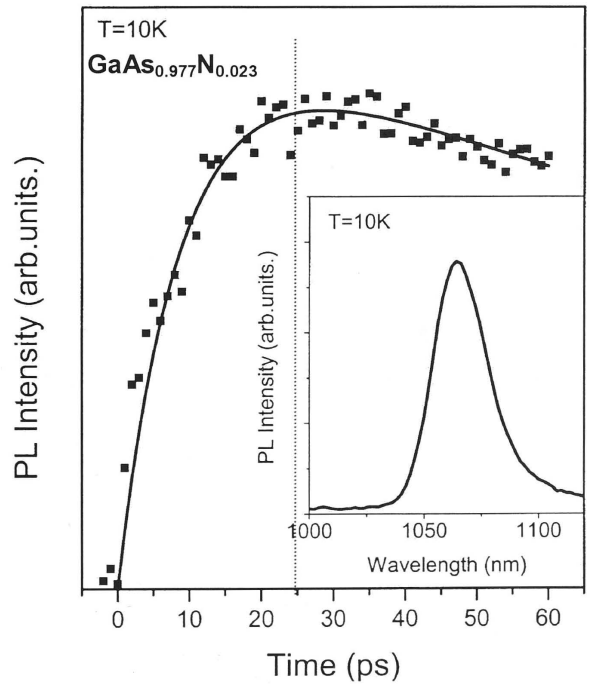

Fig. 4-2 Time evolution of the PL of a $GaAs_{0.977}N_{0.023}$ epilayer sample in the first 60 ps after excitation. The solid squares represent the experimental data; the solid line is a guide for the eyes. The dotted line indicates the PL risetime. The PL spectrum of the same sample at 10 K is also shown in the inset.

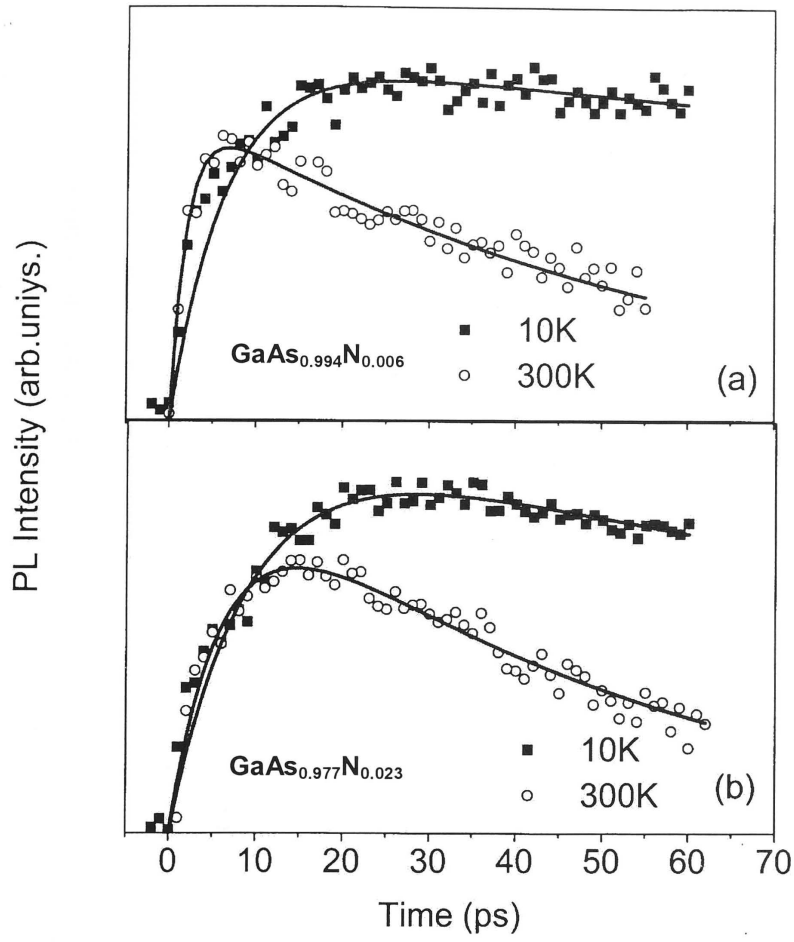

Fig. 4-3 TRPL spectra of two GaAsN epilayers with different N contents measured at 10 K and 300K. The N contents are (a) 0.6%; (b) 2.3%, respectively.

temperature. Figure 4-3 shows the time evolution of the PL of two samples (0.6% N and 2.3% N) at 10 K and 300 K, respectively. As seen from Fig. 4-3, the risetimes of the two different samples are very similar, and change very little with temperature. In all cases, the risetime is between 10-30 ps.

To explore whether it is just the alloy nature of the GaAsN samples that leads to the observed significant reduction of the PL risetime, we have also measured the TRPL signal in a different but related alloy system. We chose a quaternary $In_{0.8}Ga_{0.2}As_{0.4}P_{0.6}$ epitaxial layer with a similar PL spectrum as that of the $GaAs_{0.977}N_{0.023}$ sample. The TRPL spectra of this quaternary sample at 10 K and 300 K are shown in Fig. 4-4, with the PL spectrum in the inset. The risetime of this alloy at 10 K is more than one order of magnitude longer than that observed in the GaAsN samples and, in fact, the PL

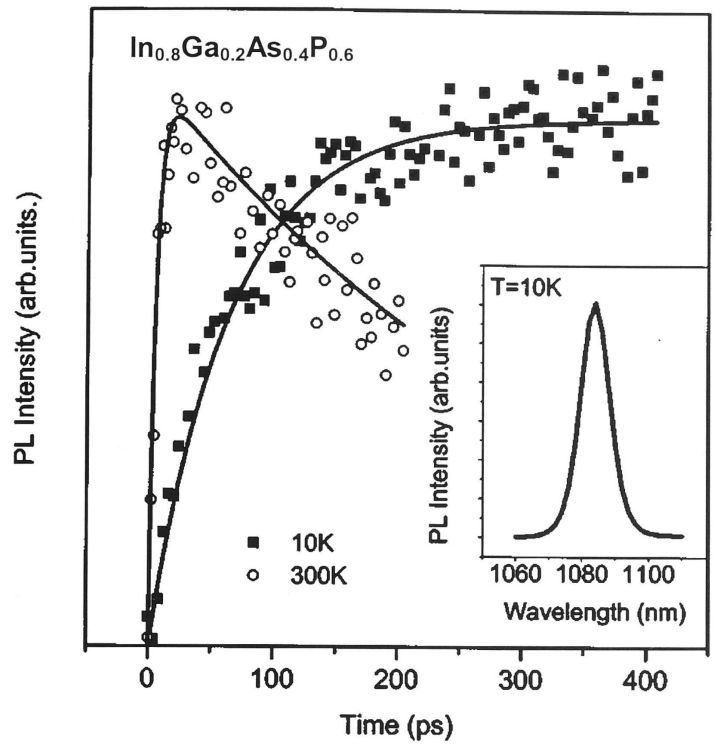

Fig. 4-4 TRPL spectra of an InGaAsP sample measured at two 10 K and 300 K. The PL spectrum of the same sample at 10 K is displayed in the inset.

intensity was still increasing 400 ps after excitation. With increasing temperature, the risetime of this sample significantly reduces, and it is approximately 15 ps at 300 K. This is similar to that observed for GaAs.[10] We can, therefore, conclude that the alloying process by itself does not result in the observed type of PL risetime for GaAsN samples. The short PL risetime and its temperature independent nature are specific characteristics of GaAsN alloy system.

We believe that the short PL risetime is an indication that the radiative recombination process in the GaAsN system does not involve excitons. Since the various studies[1,2] on the temperature and excitation intensity dependence of PL have demonstrated the involvement of localised particles in the radiative process, we have to assume here that luminescence occurs via electron-hole recombination in which one, or both, of the particles are localised. However, because recombination between localised electron and localised holes would result in a non-exponential luminescence decay, which would be contrary to the experimental observations, we, therefore, conclude that the recombination process in this alloy system must involve only one localised and one

delocalised particle. Since the nitrogen is known to mainly affect the conduction band of (In)GaAsN alloys,[11-13] we can assume that the electrons are localised by the band-edge fluctuations created by the nitrogen, and the holes remain "free". The photoexcited electrons are known to rapidly relax into band-tail states[14] which, in the InGaN system, is of the order of 0.5 ps. If we assume a similar fast capture process in the GaAsN system, the observed PL risetime is a measure of the radiative recombination rate between the localised electron and delocalised holes.

In summary, the high temporal resolution of our TRPL measurements has provided evidence that the PL risetime in GaAsN is not consistent with the formation and recombination of excitons. All the optical evidence suggests that the nature of radiative recombination in GaAsN system is related to the recombination between *localised* electrons and *delocalised* holes.

4.3.2 Optical bowing coefficient of GaAsN epilayers

There have been many studies that concentrate on the dependence of the GaAsN bandgap on N composition.[15-21] Here, we give an overall view of our experimentally determined low-temperature (10 K) PL peak positions as a function of the N content compared with some reported reference data, as seen in Figure 4-5. The composition weighted linear average of the bandgaps of the parental binary compounds, GaAs (E_g = 1.519 eV) and GaN (E_g = 3.28 eV), at 10 K is also shown in Fig. 4-5. It is obviously seen that instead of following the linear average between GaAs and GaN, the PL peak energy of GaAsN decreases with increasing N content. Although our experimental data were taken at 10 K, while the reference data were obtained at 300 K, the trend of the decrease of PL peak energy with increasing N content is comparable with reference data except those from Bi et al, probably due to the GaAsN was grown on GaP substrates in their work.[18] An optical/bandgap bowing coefficient b can be used to describe the deviation between bandgap energy of GaAsN and the linear average of the bandgap energies of GaAs and GaN as a function of N content x:

$$b(x) = \frac{x \cdot E_{g,GaN} + (1-x) \cdot E_{g,GaAs} - E_{g,GaAs_{1-x}N_x}}{x \cdot (1-x)} \tag{4.1}$$

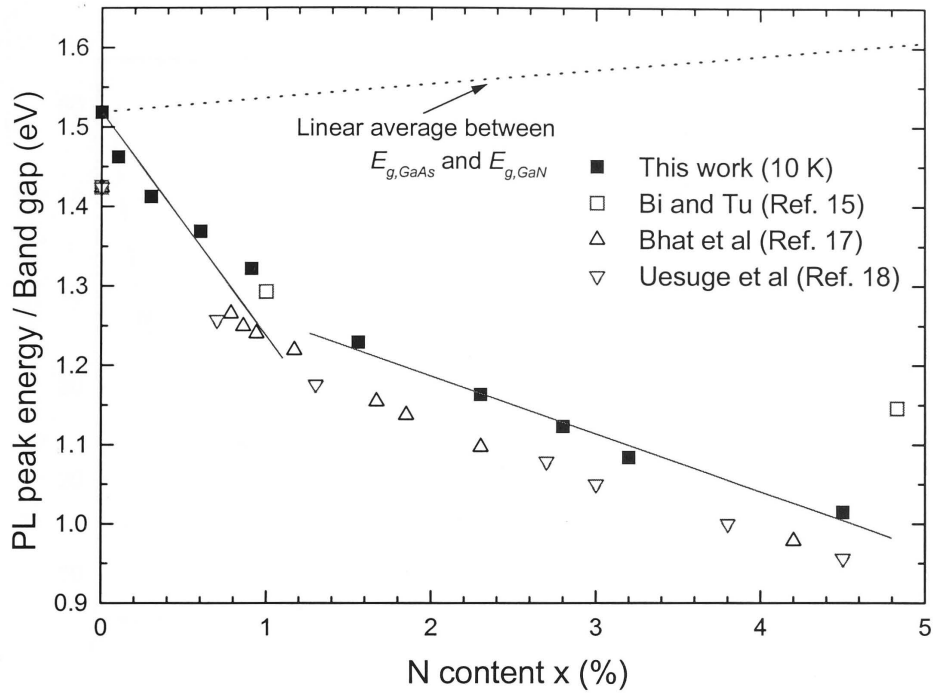

Fig. 4-5 Relationship between the N content in GaAsN and the measured PL peak energy at 10 K (or the bandgap energies from the references). The composition weighted linear average of the bandgaps of GaAs and GaN is also shown in dotted line. Two solid lines are the linear fits of our experimental data in low N content regime (< 1%) and high N content regime (> 1%), respectively.

where $E_{g,GaN}$, $E_{g,GaAs}$, and $E_{g,GaAs_{1-x}N_x}$ are, respectively, the bandgap energy of GaN, GaAs, and $GaAs_{1-x}N_x$. Based on the linear fits of our experimental data in low N content regime (< 1%) and high N content regime (> 1%) (Fig. 4-5), we note that the PL peak energy drops rapidly in the low-N-content regime (~x < 1%), but decreases slower in the relatively high-N-content regime (~x > 1%), suggesting that the bowing coefficient may not be a constant, but is dependent on N content. This can be seen more clearly in Fig. 4-6, where the optical bowing coefficients at 10 K are plotted as a function of N content x (solid squares). An empirical double exponential decay line fits the experimental data quite well, which can be expressed as:

$$b(x) = b_0 + b_1 e^{-x/t_1} + b_2 e^{-x/t_2} \tag{4.2}$$

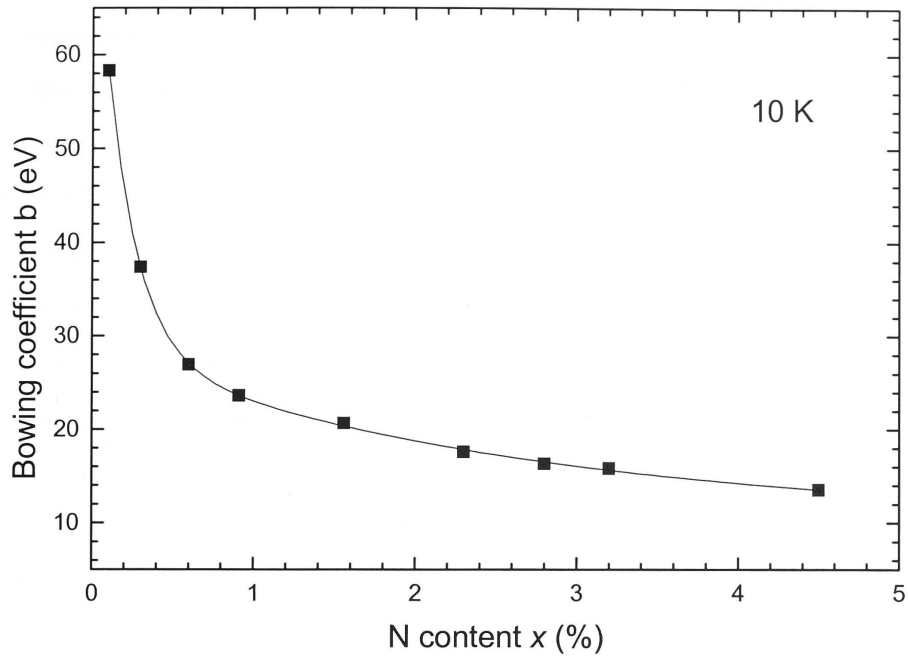

Fig. 4-6 Optical bowing coefficient b (eV) of $GaAs_{1-x}N_x$ as a function of N content x. A double exponential decay fitting line is also shown.

where b_0, b_1, b_2, t_1 and t_2 are fitting parameters, whose values are about 10.4, 51.3, 18.2, 0.19, and 2.56 eV, respectively. We found that the bowing coefficient $b(x)$ can reach very high value of ~58 eV for dilute concentrations ($x \sim 0.1\%$), and then decreases rapidly to a nearly constant value of ~15 eV for higher N concentrations ($x \geq 1.6\%$). The similar phenomenon of the strongly composition dependent $b(x)$ was also reported by several groups[18,19,22] and theoretically predicted by Wei and Zunger using a first-principle supercell model.[23] As discussed by Wei and Zunger,[23] the bandgap variation in GaAsN system as a function of x can be divided into two regions: (i) an impurity-like region where the bowing coefficient is relatively large and composition dependent, and (ii) a band-like region where the bowing coefficient is relatively smaller and nearly constant. Our experimental data clearly suggest the existence of these two regions.

In summary, we found that the optical bowing coefficient of GaAsN epilayers strongly depends on the N content, which is consistent with the first-principle super-cell model.[23] A double exponential composition dependence of the bowing coefficient is obtained to fit the experimental data.

4.3.3 N composition dependence of the band structure

To understand the evolution of the band structure of GaAsN epilayers with N content, the PL spectra as a function of temperature were collected at an excitation power of 5 mW. Figures 4-7(a) and 4-7(b) show the PL spectra from two samples with 0.3% and 1.6% N, respectively, typically representing the low-N-content range (< 1.0%) which shows a strongly exponential low-energy tail, and the high-N-content range (> 1.0%) which shows a weakly exponential low-energy tail in the 10 K PL spectra (see Fig. 4-1). It is clearly seen that for the sample with 0.3% N, at least three PL peaks (E1, E2, and E3) can be distinguished from the spectra in the measured temperature range. However, for the sample with 1.6% N, only one PL peak (E_{mix}) can be distinguished from the spectra in the same measured temperature range. Figure 4-8 shows the evolution of all these PL peaks with temperature. The progression of the PL peaks denoted as E1, E2, and E3 are in agreement with the Varshni-like dependence of temperature, whereas E_{mix} first increases and then decreases with increasing temperature (hereafter called C-shape behaviour). Obviously, the E1, E2 and E3 peaks indicate that there are three different emission bands. We propose that the PL emission E1, which cannot be distinguished at 10 K due to the overlapping of E1, E2 and E3, is the result from the recombination of electrons from the conduction-band edge (CBE) with holes. PL emissions of E2 and E3 are attributed to the recombination of electrons trapped in the localised states (LS) near the conduction-band edge with delocalised holes, as previously discussed in *section 4.3.1*. It is possible that when the N concentration in GaAsN is high enough (e.g. 1.6%), these emission bands are so close to each other that they cannot be distinguished, resulting in a combined PL peak E_{mix}. Similar PL emissions were also reported in several papers,[1,24-26] where they were ascribed to the likely formation of localised defect/cluster states near the conduction band as well.

To further investigate the PL emission behaviours in the different N-composition regimes (i.e. N%< 1.0% and > 1.0%), temperature dependent PL measurements were performed on various GaAsN epilayer samples with different N contents. Figure 4-9 shows these PL spectra from two samples with 0.6% and 3.2% N, respectively. The similar features to those observed in Fig. 4-7 can be seen in Fig. 4-9, indicating two different N-composition regimes indeed exist. It is also noted that the different PL emissions become more difficult to be distinguished with increasing N content (e.g. from

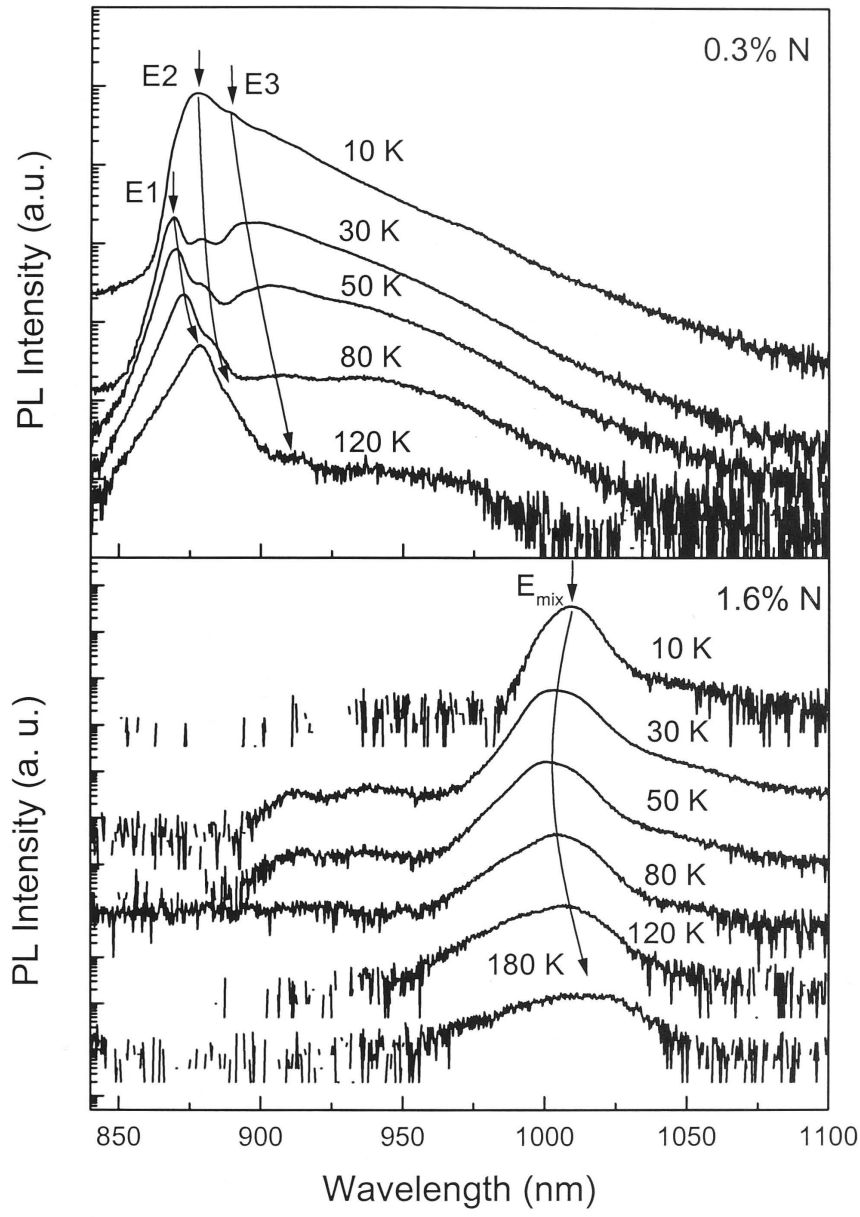

Fig. 4-7 Temperature dependence of PL spectra of GaAsN epilayer samples with (a) 0.3% N, and (b) 1.6% N, respectively. Spectra are shifted vertically for clarity.

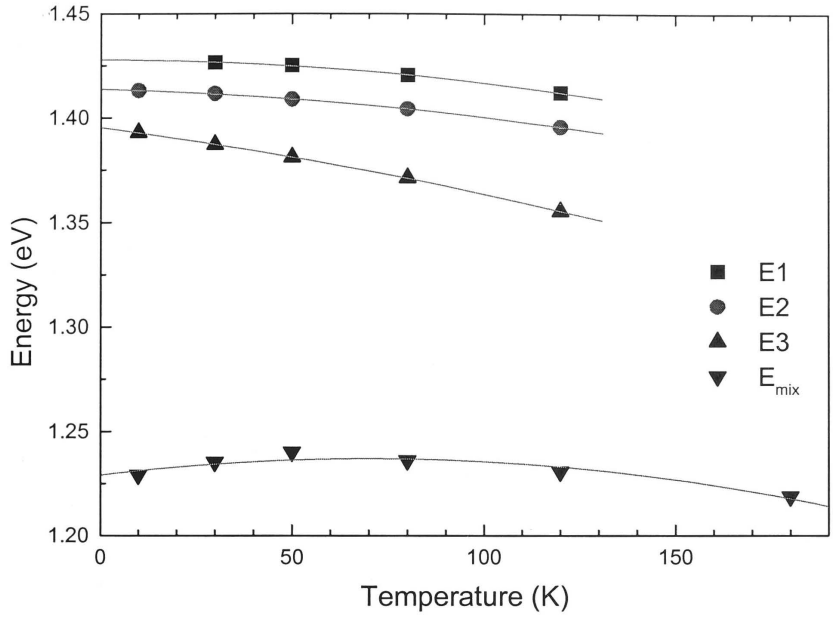

Fig. 4-8 Evolution of PL peaks E1, E2, E3 and E_{mix} indicated in Fig. 4–7 with measurement temperature.

0.3% to 0.6% N). This characteristic phenomenon in the GaAsN alloy system can readily be explained in terms of the N-regime model proposed in Ref. 27. In this model, a critical N composition x_c is proposed, which is estimated at about 1% from our experimental data. At N composition $x < x_c$, LS appears within the bandgap and cause a rapid decrease of the bandgap with incorporation of N. With increasing N content ($x \geq x_c$), LS starts to interact with CBE and forms an extended amalgamation region. Conventional alloy behaviour can be expected only at very high N composition ($x >> x_c$), where all LS are far above the conduction band minimum.

In this study, energy state of E_{mix} is obviously in the amalgamation region and behaves more like localised state. When temperature increases slightly, more localised electrons thermally activate to the delocalised states, resulting a blue shift of the PL peak energy. When the temperature is high enough, most of the localised electrons are activated. Therefore, the PL emission is dominated by the band-edge emission and redshifts with increasing temperature. The origin of the C-shape behaviour of PL peak E_{mix} as a function of temperature in this study is very similarly to that of the S-shape

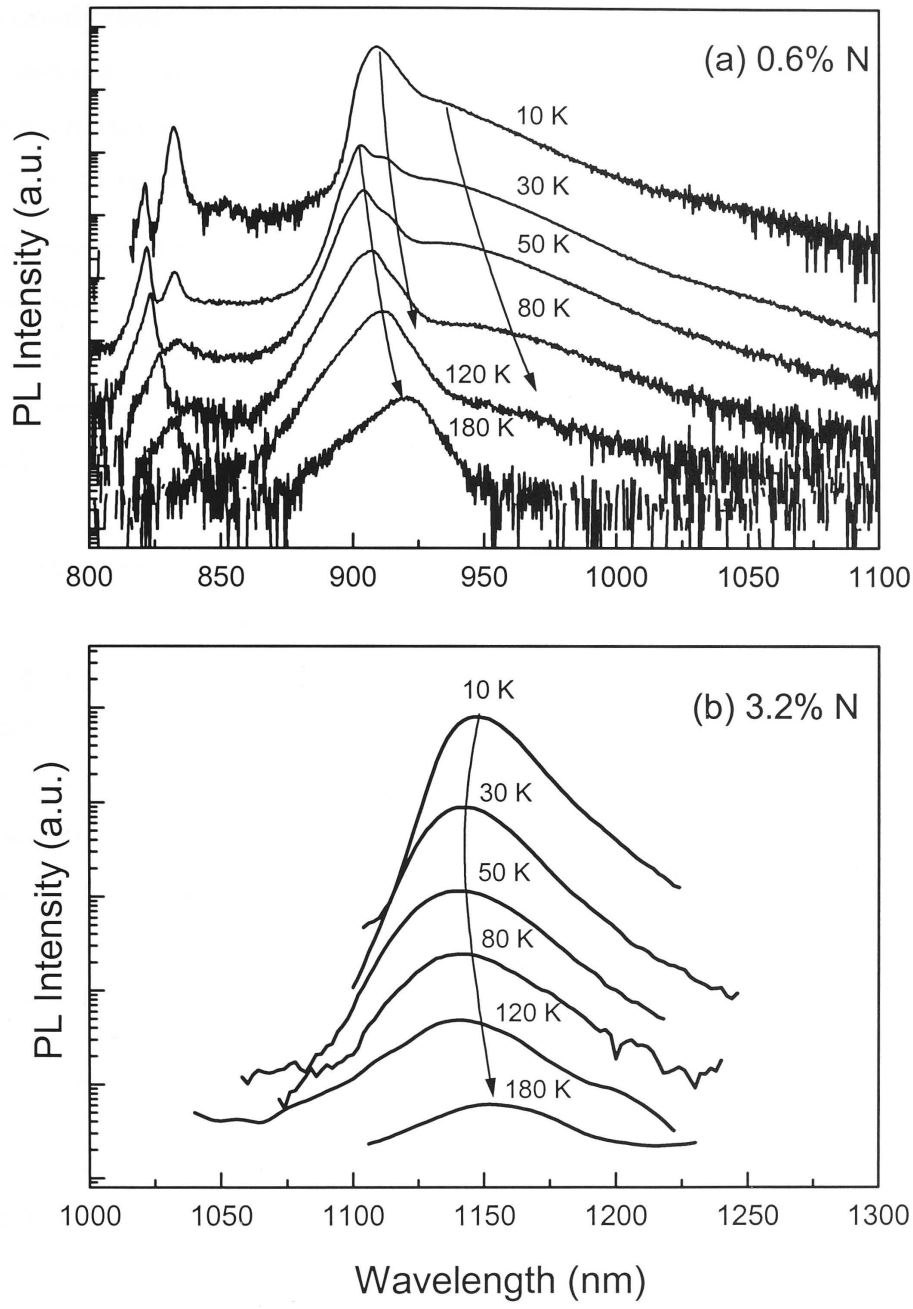

Fig. 4-9 Temperature dependence of PL spectra of GaAsN epilayer samples with (a) 0.3% N; and (b) 1.6% N. Spectra are shifted vertically for clarity.

behaviour in (In)GaAsN alloy systems reported by many groups.[24-26] The difference in shape could be due to the differences of the N content, the sample's treatment (annealed or as-grown), the excitation intensity, and the measurement system. The above results clearly reveal that the PL peak at low temperatures (e.g. 10 K or lower) does not solely originate from the interband transition, but from a combination of the interband transition and transitions involving localised states. The interband transition becomes more pronounced with increasing N content or increasing temperature.

In summary, the band structure of GaAsN epilayers was readily explained by N-composition-regime model proposed by Kent and Zunger.[27] It is revealed that low-temperature (10 K) PL emission from the GaAsN epilayers is not solely due to the interband transition, but originates from a combination of several transitions involving localised defect/cluster states near the conduction band.

4.3.4 Epitaxially grown GaAsN random lasers

In general, the PL intensity of GaAsN epilayers decreases with increasing N concentration. However, there is an exception for a 500 nm thick epilayer with 2.8% N, which shows an enhanced PL emission (see Fig. 4-1). More interestingly, a random lasing scenario was observed from this sample under optical excitation, as discussed in detail in next sections. To understand the origin of these unusual results, we also investigated the surface morphology and the microstructure of this sample using AFM, SEM and XTEM. The results and discussion are presented in the following sections.

Lasing scenario

Figure 4-10 shows the excitation intensity dependence of PL spectra at 10 K of a 500 nm thick $GaAs_{0.972}N_{0.028}$ epilayer sample. At a low excitation level, the spectrum exhibits common features of this alloy system, similarly to those shown in Fig. 4-1. However, under higher intensity pulsed excitation, the PL spectrum changes radically. Above a certain threshold excitation intensity, several narrow, laser-like peaks appear, as shown in Figs. 4-10(b) and (c), which represent the spectra measured at two different spots on the sample. Unlike the conventional lasing emissions from the edge-emitting semiconductor laser devices, the mode spacings of the lasing lines in Fig. 4-10

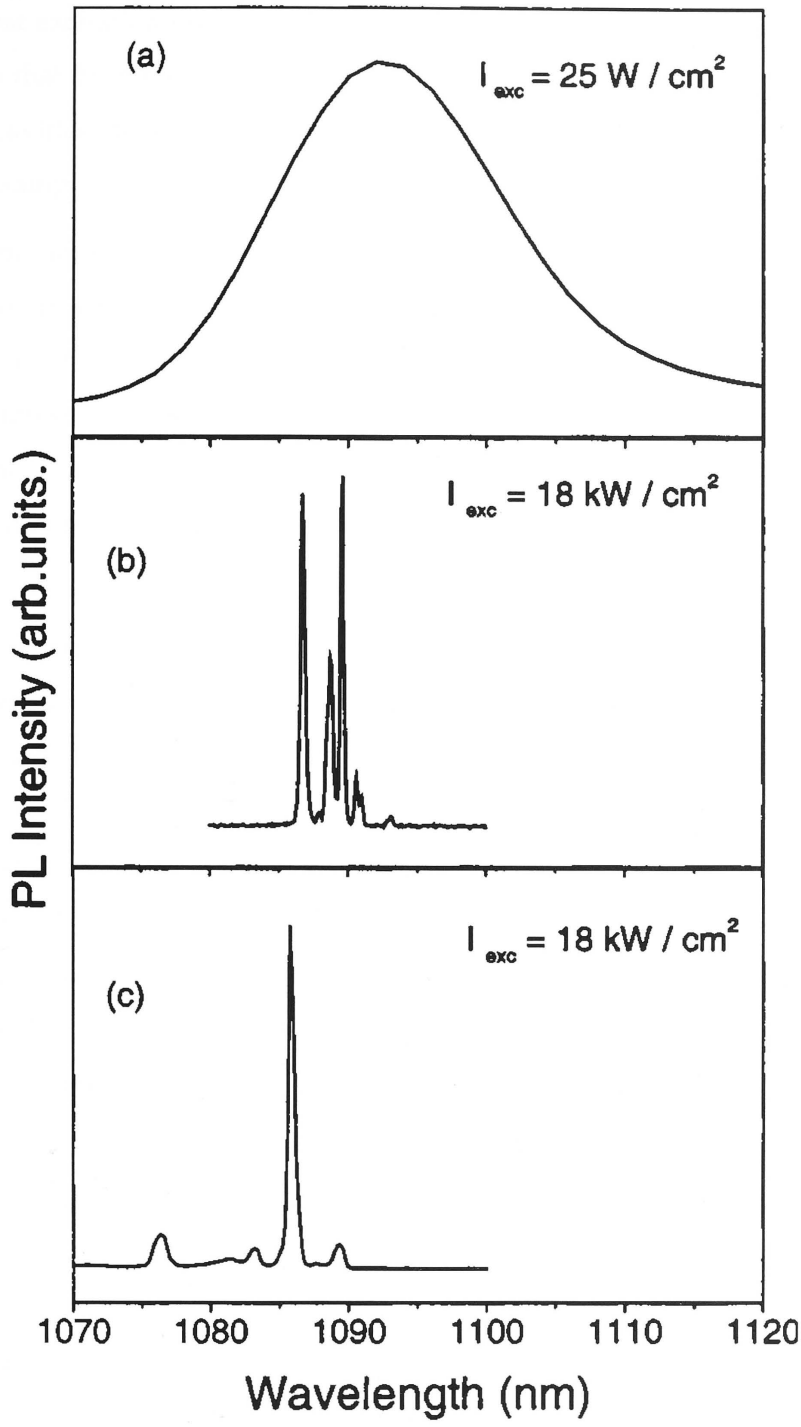

Fig. 4-10 (a) Low temperature (10 K) photoluminescence spectra of a $GaAs_{0.972}N_{0.028}$ epilayer sample grown on GaAs below threshold excitation; (b), (c) The spectra at two different spots on the sample above threshold.

are broad, irregular, and change with excitation position and intensity. Moreover, even at the highest excitation intensity, much fewer modes (< 10) were observed from this sample than that from the conventional edge-emitting laser devices. This suggests that the optical cavities embedded in this sample are much smaller than the actual dimensions of the samples.

Furthermore, the emission intensity of each mode displays distinctive threshold behaviour, as shown in Fig. 4–11, indicating that the lasing does indeed occur. The inset of Fig. 4–11 shows the three modes for which the threshold was measured at 10 K. The lasing threshold varies between 0.1 and 10 kW/cm^2, depending on the lasing mode and the location of excitation on a given sample. These characteristics reveal that these lasing modes are related to different optical cavities.

Another essential feature of these laser spectra is that they could be detected from any angle of observation. We have collected the lasing emission spectra in three orthogonal directions, as shown in Fig. 4–12. Although the spectral positions of the lasing lines and the mode separations fluctuate with the observation angle, laser-like emissions were observed from all three directions. It is also interesting to note that the emission emerging from the edges of the samples was linearly polarised in a direction perpendicular to the sample surface but was unpolarised when emerging perpendicular to the top surface of the sample. The laser-like emission (line spectra) disappeared upon heating the sample to temperatures above approximately 100 K, but the broad, spontaneous emission remained.

Another interesting feature of the laser emission from this sample is the excitation volume dependence of the threshold intensity. For example, at a given point on the sample and a given excitation intensity of 1 kW/cm^2, lasing occurred when the excitation spot size was *larger* than 2500 μm^2 but disappeared when the spot size was reduced below this value.

Figure 4–13 shows the TRPL spectra of this lasing sample using PL upconversion technique. The rise time was found to be approximately 30 ps both below and above threshold, which is similar to the rise times measured for other GaAsN samples (Fig. 4–3). The decay time, on the other hand, was significantly reduced above the threshold excitation intensity. While below threshold the decay time was of the order of 400 ps or more, above threshold it was reduced to between 20 and 80 ps depending on the sample position and excitation intensity. The decay spectrum above threshold often

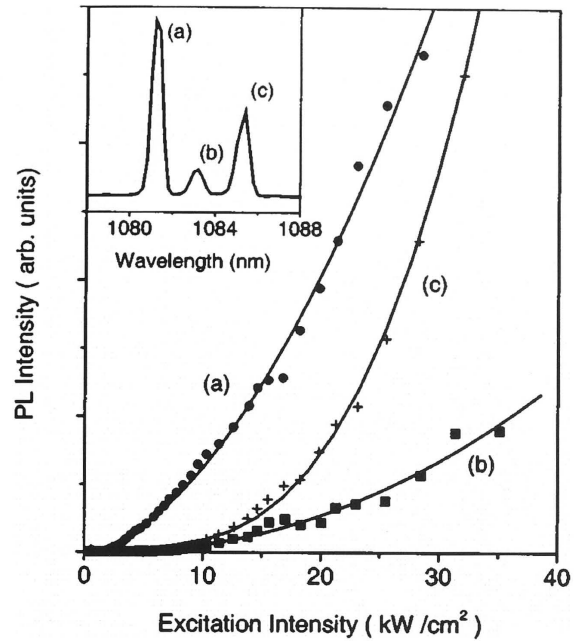

Fig. 4-11 Low temperature (10K) PL of a $GaAs_{0.972}N_{0.028}$ layer as a function of the excitation intensity for three different laser modes, as shown in the inset.

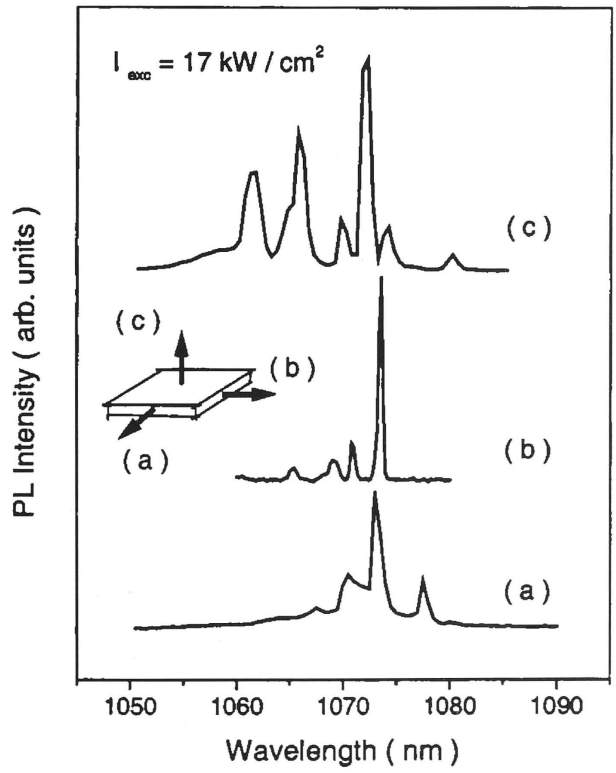

Fig. 4-12 Laser-like emission with similar mode structure detected from three orthogonal directions from a $GaAs_{0.972}N_{0.028}$ layer grown on GaAs.

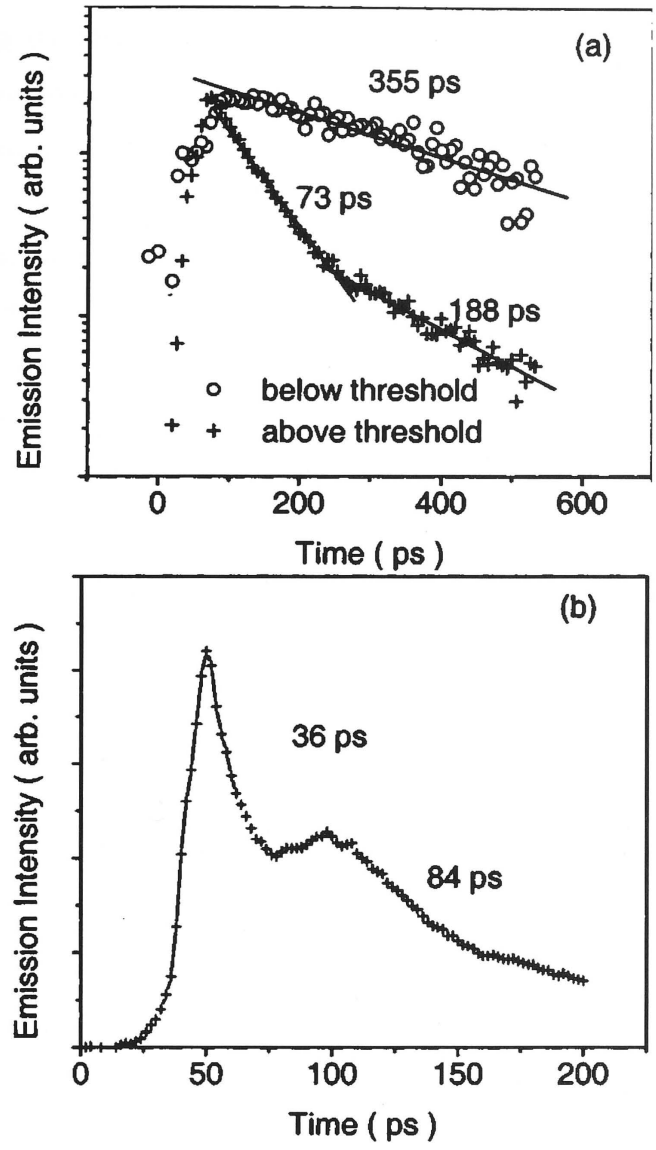

Fig. 4-13 (a) Low temperature photoluminescence decay as a function of time measured below and above threshold excitation. (b) Photoluminescence relaxation oscillations observed at some positions on the sample.

involves two decay processes with differing time constants, as shown in Fig. 4-13(a). In addition, at some positions on the sample, relaxation oscillations were observed, as seen in Fig. 4-13(b). The significant reduction in the luminescence decay time above threshold is consistent with the nature of (stimulated) emission in these samples, and the variation of the decay constant with position can be an indication of the existence of different cavities with different losses/gains.

Overall, these results are very similar to those reported recently by a number of groups describing the observation of laser emission from various random or disordered media. For example, Cao *et al.*[28] reported laser emission from polycrystalline ZnO films, and ZnO and GaN powders, which do not contain any obvious optical cavities with mirrors. Above threshold, the lasing spectra could be observed in all angular directions, and varied with excitation level and excitation volume.[28] Soukoulis *et al.*[29] reported relaxation oscillations and position-dependent decay times in ZnO random lasers, which are similar to those observed in our experiments. These results are also the characteristics of other 'random lasers', such as the lasing emissions from laser dye solutions containing microparticles,[30] organic dye-doped gel films,[31] and opal crystals saturated with polymer and laser dye solutions.[31] In all these systems, the key to laser emission is the existence of a high gain medium and efficient light scattering within the sample to produce the necessary coherent feedback.

Structural properties

The above experimental results indicate that the underlying mechanism for the laser-like emissions from the 500 nm thick $GaAs_{0.972}N_{0.028}$ epitaxial layer is similar to that found in random lasers. While gain is known to be present in high quality GaAsN layers, the existence of efficient light scattering is uncertain. A number of previous studies have called attention to the inherent inhomogeneous structural properties of this group of alloys. For example, optical absorption and Raman studies have suggested that alloy ordering may take place in these materials, while other studies indicated the existence of nitrogen enriched GaAsN clusters due to the significant differences of atomic size and electronegativity between As and N.[32,33] Here, the surface morphology of this lasing sample using AFM was investigated, as shown in Fig. 4–14(b). For comparison, the AFM image of a low-N-content (0.6% N) GaAsN sample grown at the same temperature with the same thickness is also shown in Fig. 4–14(a). For the low-N-content GaAsN sample [Fig. 4–14(a)], the surface shows a step/terrace structure with a small root-mean square (RMS) roughness of about 0.76 nm. However, this structure was no longer observed and some local features were noted for the other sample with 2.8% N, such as some circular bumps [Fig. 4–14(b)]. In particular, the surface of the $GaAs_{0.972}N_{0.028}$ epilayer becomes very rough (RMS = 4 nm) and many parallel microcracks were observed. This is mainly because that the GaAsN layer thickness (500 nm)

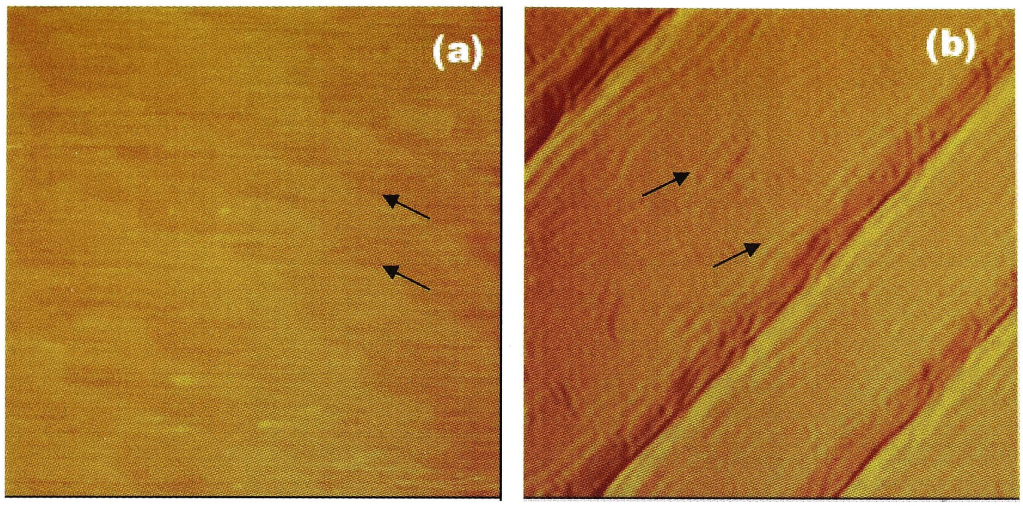

Fig. 4-14 1 x 1 μm^2 AFM surface images of two GaAsN epilayers grown at 600 °C and with the thickness of 500 nm. The N contents are, respectively, (a) 0.6%, and (b) 2.8%. The arrows indicate the step/terrace edge in image (a) and bumps in image (b), respectively.

is well above the critical layer thickness, though the exact value of critical thickness for this sample is not well known. No indication of the 3D-growth was observed for both samples. Further evidence of these micro-cracks in $GaAs_{0.972}N_{0.028}$ epilayer can be seen from the top-view SEM image of this sample (Fig. 4–15), which shows a micro-crack with a width of 10–50 nm. These cracks appear randomly across this sample, often as two mutually perpendicular sets of parallel lines, which may form mirrors to reflect and enhance the light output, resulting in the enhanced PL emission and even lasing emissions.

Further insight on the microstructural properties of this lasing sample was obtained by using XTEM technique to study the GaAsN/GaAs interface. Figure 4–16(a) and 4–16(b) show the XTEM images of two different GaAsN samples along near <110> zone direction. These two samples were grown at the same temperature (600 °C) with the same thickness but with different N contents as indicated in the figure. The same samples were also used for PL measurements (Fig. 4–1) and AFM imaging (Fig. 4–14). It is noted that the contrast at the interface between the epilayer and the substrate is mainly due to the misfit strain. The interfacial regions of both samples are clearly seen, indicating that both GaAsN epilayers experience a certain amount of strain near the

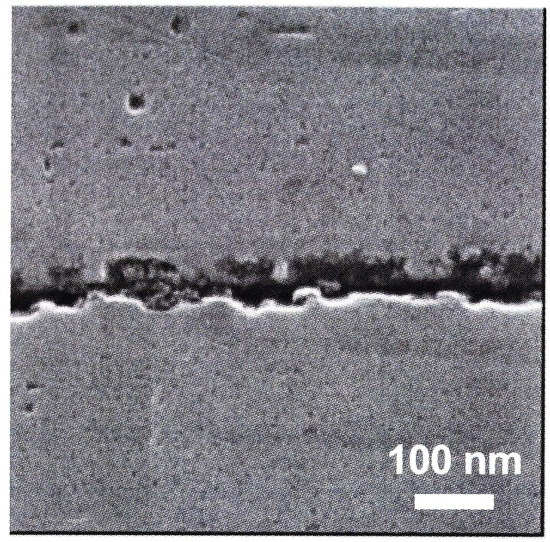

Fig. 4-15 Top view SEM image of a 500 nm thick GaAsN epilayer grown on GaAs.

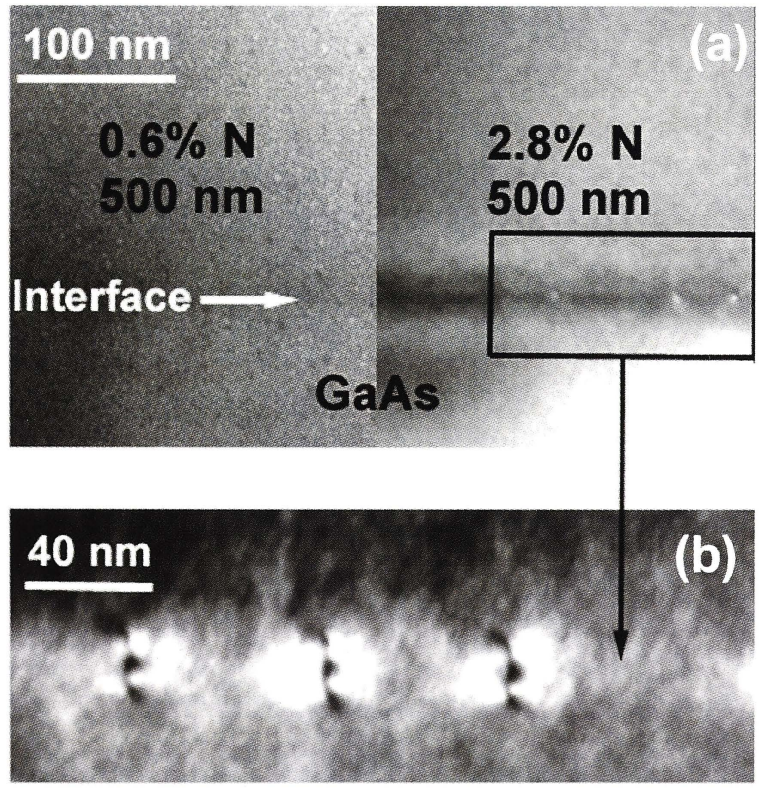

Fig. 4-16 (a) Bright field XTEM images of the interfacial regions between GaAsN and GaAs. (b) Dark field XTEM image of GaAsN/GaAs interface of the sample with 2.8% N.

interfacial region. It is also noted that no misfit dislocations were observed in low-N-content sample. However, high density of dislocations were observed in the sample with 2.8%N. This is because the epilayer thickness of this sample is greater than the critical layer thickness (depending upon the misfit strain and epilayer thickness) required for the misfit dislocation formation[34]. These misfit dislocations could be seen as white dots in Fig. 4-16(a) where they were viewed edge-on (i.e. parallel to the incidental electrons inside a TEM). To image the misfit dislocation more clearly, the sample was tilted along the <220> axis that is in the interface, so that the interface was inclined to the electron beam and segments of misfit dislocations can be seen easily as shown in Fig. 4-16(b). These dislocations are consistent with the formation of microscopic cracks, which are seen from the AFM and SEM images of this sample (Figs. 4-14(b) and 4-15). These features could have been easily used to account for the degraded optical properties. However, on the contrary, these dislocations and micro-cracks enhanced the PL intensity and resulted in the lasing behaviour. Interestingly, apart from these micro-cracks, this sample maintained relatively high crystal quality in most areas, resulting a narrow linewidth of the GaAsN peak in the DCXRD spectrum (Fig. 3-5). It was also observed in the XTEM images that away from the GaAsN/GaAs interface, the overall crystal quality seems relatively high for both GaAsN samples investigated here. These structural inhomogeneities could well explain the efficient light scattering necessary for random lasing.

To check the reproducibility of this type of lasing emission, several samples with the same N composition but differing thickness were grown. Similar lasing emissions were observed from samples with GaAsN thickness beyond 500 nm. However, no such lasing emissions were observed from samples with GaAsN thickness below 500 nm. This again confirms that this type of lasing emissions is closely related to the formation of dislocations and microscopic cracks.

In summary, a GaAsN epilayer sample grown by MOCVD was found to exhibit characteristic emission properties of the random lasers. The surface morphology and microstructures of this sample were investigated by AFM, SEM, and XTEM. Parallel microscopic cracks were found on the surface and dislocations were observed at the GaAsN/GaAs interface. It is believed that the structural inhomogeneities, such as dislocations and microscopic cracks, are the efficient light scattering centres for random lasing.

4.4 Conclusion

In conclusion, the high temporal resolution of the TRPL measurements has provided evidence that the nature of the low-temperature (10 K) radiative recombination in GaAsN systems is related to the recombination between *localised* electrons and *delocalised* holes. The optical bowing coefficient of GaAsN epilayers was found to strongly depend on the N content, which is consistent with the first-principle supercell model.[23] Based on the temperature dependence of PL measurements, it was also revealed that the low-temperature (10 K) PL peak emission from GaAsN epilayers is not solely resulted from the interband transition, but originates from the combination of several transitions involving localised defect/cluster states near the conduction band. These results also confirm a N-composition dependent conduction-band structure for GaAsN alloys. The structural studies of GaAsN epilayers have demonstrated that, when the thickness of GaAsN layers is above a critical value, microscopic cracks and dislocations begin to form on the sample's surface and at the GaAsN/GaAs interface, respectively. These structural inhomogeneities form efficient light scattering centers, resulting in random lasing emissions from the thick ($\geq$ 500 nm) $GaAs_{0.972}N_{0.028}$ epilayers grown on GaAs.

References

1 I. A. Buyanova, W. M. Chen, G. Pozina, J. P. Bergman, B. Monemar, H. P. Xin, and C. W. Tu, Appl. Phys. Lett. **75,** 501 (1999).

2 X. D. Luo, Z. Y. Xu, W. K. Ge, Z. Pan, L. H. Li, and Y. W. Lin, Appl. Phys. Lett. **79,** 958 (2001).

3 S. Z. Wang, S. F. Yoon, W. K. Loke, C. Y. Liu, and S. Yuan, J. Cryst. Growth **255,** 258 (2003).

4 B. Q. Sun, M. Gal, Q. Gao, H. H. Tan, and C. Jagadish, Appl. Phys. Lett. **81,** 4368 (2002).

5 S. Francoeur, G. Sivaraman, Y. Qiu, S. Nikishin, and H. Temkin, Appl. Phys. Lett. **72,** 1857 (1998).

6 H. P. Xin and C. W. Tu, Appl. Phys. Lett. **72,** 2442 (1998).

7 T. Kageyama, T. Miyamoto, S. Makino, F. Koyama, and K. Iga, Jpn. J. Appl. Phys., Part 2 **38,** L298 (1999).

8 M. Gurioli, P. Borri, M. Colocci, M. Gulia, F. Rossi, E. Molinari, P. E. Selbmann, and P. Lugli, Phys. Rev. B **58,** R13403 (1998).

9 T. C. Damen, J. Shah, D. Y. Oberli, D. S. Chemla, J. E. Cunningham, and J. M. Kuo, Phys. Rev. B **42,** 7434 (1990).

10 J. Shah, B. Deveaud, T. C. Damen, W. T. Tsang, A. C. Gossard, and P. Lugli, Phys. Rev. Lett. **59,** 2222 (1987).

11 M. Kondow, K. Uomi, A. Niwa, T. Kitatani, S. Watahiki, and Y. Yazawa, Jpn. J. Appl. Phys., Part 1 **35,** 1273 (1996).

12 P. Krispin, S. G. Spruytte, J. S. Harris, and K. H. Ploog, J. Appl. Phys. **89,** 6294 (2001).

13 B. Q. Sun, D. S. Jiang, Z. Pan, L. H. Li, and R. H. Wu, J. Cryst. Growth **227,** 501 (2001).

14 C. K. Sun, Y. L. Huang, S. Keller, U. K. Mishra, and S. P. DenBaars, Phys. Rev. B **59,** 13535 (1999).

15 M. Weyers, M. Sato, and H. Ando, Jpn. J. Appl. Phys. Part 2 **31,** L853 (1992).

16 M. Kondow, K. Uomi, K. Hosomi, and T. Mozume, Jpn. J. Appl. Phys. Part 2 **33,** L1056 (1994).

17 A. Ougazzaden, Y. Lebellego, E. V. K. Rao, M. Juhel, L. Leprince, and G. Patriarche, Appl. Phys. Lett. **70,** 2861 (1997).

18 W. G. Bi and C. W. Tu, Appl. Phys. Lett. **70,** 1608 (1997).

[19] U. Tisch, E. Finkman, and J. Salzman, Appl. Phys. Lett. **81,** 463 (2002).

[20] R. Bhat, C. Caneau, L. Salamanca-Riba, W. Bi, and C. Tu, J. Cryst. Growth **195,** 427 (1998).

[21] K. Uesugi, N. Morooka, and I. Suemune, Appl. Phys. Lett. **74,** 1254 (1999).

[22] R. Chtourou, F. Bousbih, S. Ben Bouzid, F. F. Charfi, J. C. Harmand, G. Ungaro, and L. Largeau, Appl. Phys. Lett. **80,** 2075 (2002).

[23] S. H. Wei and A. Zunger, Phys. Rev. Lett. **76,** 664 (1996).

[24] H. Yaguchi, S. Kikuchi, Y. Hijikata, S. Yoshida, D. Aoki, and K. Onabe, Phys. Stat. Sol. B **228,** 273 (2001).

[25] A. R. Kovsh, J. S. Wang, L. Wei, R. S. Shiao, J. Y. Chi, B. V. Volovik, A. F. Tsatsul'nikov, and V. M. Ustinov, J. Vac. Sci. Technol. B **20,** 1158 (2002).

[26] R. J. Potter, N. Balkan, H. Carrere, A. Arnoult, E. Bedel, and X. Marie, Appl. Phys. Lett. **82,** 3400 (2003).

[27] P. R. C. Kent and A. Zunger, Phys. Rev. Lett. **86,** 2613 (2001).

[28] H. Cao, Y. G. Zhao, S. T. Ho, E. W. Seelig, Q. H. Wang, and R. P. H. Chang, Phys. Rev. Lett. **82,** 2278 (1999).

[29] C. M. Soukoulis, X. Y. Jiang, J. Y. Xu, and H. Cao, Phys. Rev. B **65,** 041103 (2002).

[30] N. M. Lawandy, R. M. Balachandran, A. S. L. Gomes, and E. Sauvain, Nature (London) **386,** 436 (1994).

[31] S. V. Frolov, Z. V. Vardeny, A. A. Zakhidov, and R. H. Baughman, Opt. Commun. **162,** 241 (1999).

[32] S. Gwo and S. Y. Huang, Phys. Rev. B **64,** 113312 (2001).

[33] K. Matsuda, T. Saiki, M. Takahashi, A. Moto, and S. Takagishi, Appl. Phys. Lett. **78,** 1508 (2001).

[34] J. Zou and D. J. H. Cockayne, Phys. Rev B **49,** 8086 (1994).

CHAPTER 5

Ion damage buildup and electrical isolation in GaAsN epilayers

5.1 Ion damage buildup in GaAsN epilayers

5.1.1 Introduction

Ion implantation has been widely used as an important step in fabrication of various electrical and optical semiconductor devices, such as selective-area doping, electrical and optical isolation, and quantum-well intermixing. However, bombardments with energetic ions inevitably produce lattice defects, which are often an undesirable side effect of ion-beam processing. Undesirable damage, in fact, is always the main problem for satisfactory selective-area doping and QW intermixing made by ion implantation. Therefore, understanding of implantation damage and its consequences in semiconductors is very important for a successful application of ion implantation in device fabrication. A great amount of information has been gathered on damage buildup (i.e., lattice damage as a function of ion dose) in various III-V compound semiconductors, such as GaAs, AlGaAs, and GaN,[1-6] in the past few decades. However, there has not been any report on the damage buildup in dilute III-V nitride semiconductors. From the studies on ternary semiconductor alloy such as AlGaAs, it was found that the resistance to amorphisation in AlGaAs increases with Al content.[4,5] The similar question arises here when dealing with GaAsN alloy system: what is the relationship between damage formation and the fraction of N in GaAsN? Additionally, epitaxial growth temperature is crucial for crystal quality and it was found that increasing growth temperature can improve the optical properties in GaAsN.[7] Therefore, the effects of N content and growth temperature on damage buildup in GaAsN are discussed in this chapter. To properly understand the damage buildup and amorphisation processes in GaAsN, irradiations were carried out at LN_2 temperature to minimise dynamic annealing effects that are expected to occur at higher temperatures.

5.1.2 Experimental

For ion damage buildup studies, all structures were grown on SI-GaAs (100) substrates at 76 Torr. An initial GaAs buffer layer of ~0.5 μm was first grown on the GaAs substrate at 650°C followed by 200 nm thick GaAsN epilayers. Two sets of GaAsN epilayers were used in this study. In order to investigate the effect of N content on the

process of ion damage buildup, one set of GaAsN layers with different N contents of 0%, 1%, and 2% were grown at 600 °C. To study the effect of growth temperature which was found to be a crucial factor affecting the optical properties of GaAsN materials,[7] the second set of samples with same N content of 1% were grown at different temperatures of 550, 600, and 630 °C. Implantations were performed at LN_2 temperature with low energy, 50 keV Si^- beams to ensure that the ions were confined only to the near surface regions (to minimise interfacial effects), as shown in Fig. 5-1, where the displacement density profile was calculated using TRIM[8] (transport of ions in matters) code. During implantation, the samples were tilted 7° away from the beam axis to minimise channeling effects. Ion fluences ranging from 2×10^{13} to 1×10^{14} cm^{-2} were used and the beam flux was maintained at 1.55×10^{11} $ions \cdot cm^{-2}s^{-1}$. Analysis was carried out at room temperature by Rutherford backscattering channeling technique (RBS-C), as described in Chapter 2. The detector was set at a glancing angle of 100° (10° grazing exit angle to the surface) to increase the depth resolution in the regions of interest.

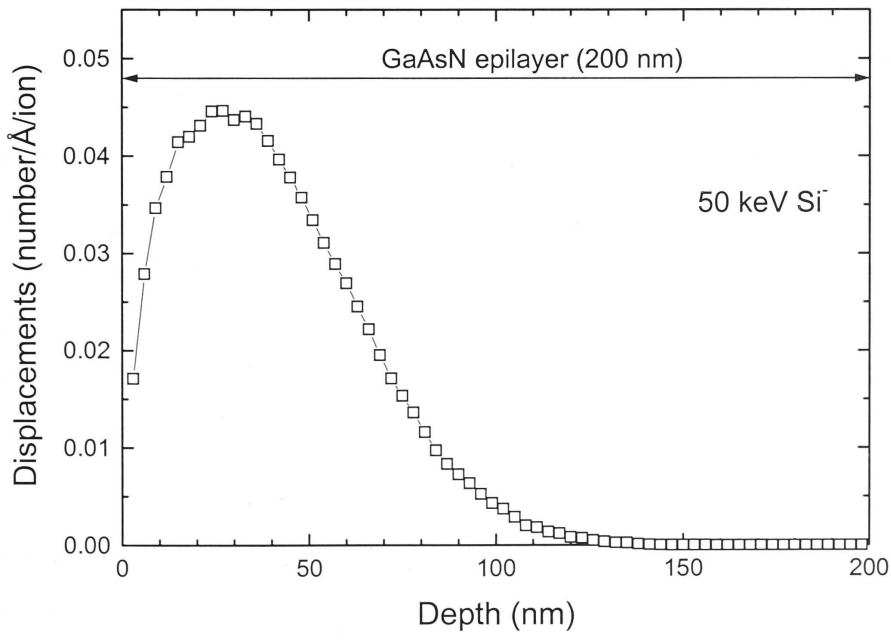

Fig. 5-1 Profile of displacement density calculated by TRIM[8] code in 200 nm thick GaAsN epilayers implanted with 50 keV Si ions, indicating the ion beam damage is confined in the near surface regions.

5.1.3 Results and discussion

Damage buildup as a function of N composition

Figures 5-2(a)-(c) illustrate the RBS-C spectra of the damage buildup at LN_2 temperature as a function of ion fluence in GaAsN epilayers of various N contents (x = 0, 1%, and 2%, respectively). As observed by RBS channeling, at an ion fluence of 2×10^{13} cm^{-2}, no obvious damage buildup was observed except the dechannelling yield increased slightly for all three samples. Then with further increase of ion fluence, the amount of disorder increased until a buried damage peak was formed at a depth of ~30 nm, corresponding to the maximum displacement (nuclear energy deposition) density of 50 keV Si ions as calculated by TRIM[8] code (Fig. 5-1). The observation of this buried damage peak is a result of direct backscattering of the incident ions and is indicative of the formation of point defects, clusters and possibly small pockets of amorphous zones created by the individual ion tracks.[9] With increasing ion fluence, the density of these defects increases until a level when the aligned signal just coincides with the random level, which can be interpreted as, a buried amorphous layer is just formed at this stage. Although a continuous amorphous layer is not necessarily formed at this fluence, it is reasonable to take this fluence as a convenient measure of the onset of amorphisation. Therefore, for GaAs, the onset of amorphisation is at $\sim 1 \times 10^{14}$ cm^{-2}, for both $GaAs_{0.99}N_{0.01}$ and $GaAs_{0.98}N_{0.02}$, the threshold fluences are $\sim 5 \times 10^{13}$ cm^{-2}. Beyond the threshold fluence, the damage peak grows both towards the surface and substrate to form a continuous amorphous layer in both $GaAs_{0.99}N_{0.01}$ and $GaAs_{0.98}N_{0.02}$. Although the threshold fluence to form amorphous layer is same $GaAs_{0.99}N_{0.01}$ and $GaAs_{0.98}N_{0.02}$, at the same ion fluence, the amorphous layer in $GaAs_{0.98}N_{0.02}$ is broader than that in $GaAs_{0.99}N_{0.01}$, indicating more damage buildup in $GaAs_{0.98}N_{0.02}$ than in $GaAs_{0.99}N_{0.01}$. Based on these results, we can conclude that GaAsN epilayers become easier to amorphise with increasing N content.

The effect of N content on the damage buildup in GaAsN epilayers can be more clearly seen in Fig. 5-3, which presents RBS-C spectra of unimplanted and implanted (3×10^{13} cm^{-2}) GaAs, $GaAs_{0.99}N_{0.01}$ and $GaAs_{0.98}N_{0.02}$ samples. Although higher concentration of nonradiative centres or defects were accounted for the degradation in optical properties of GaAsN epilayers with higher N contents,[10-13] these grown-in defects are virtually undetectable by RBS-C spectroscopy, as evidenced by the similar spectra (no

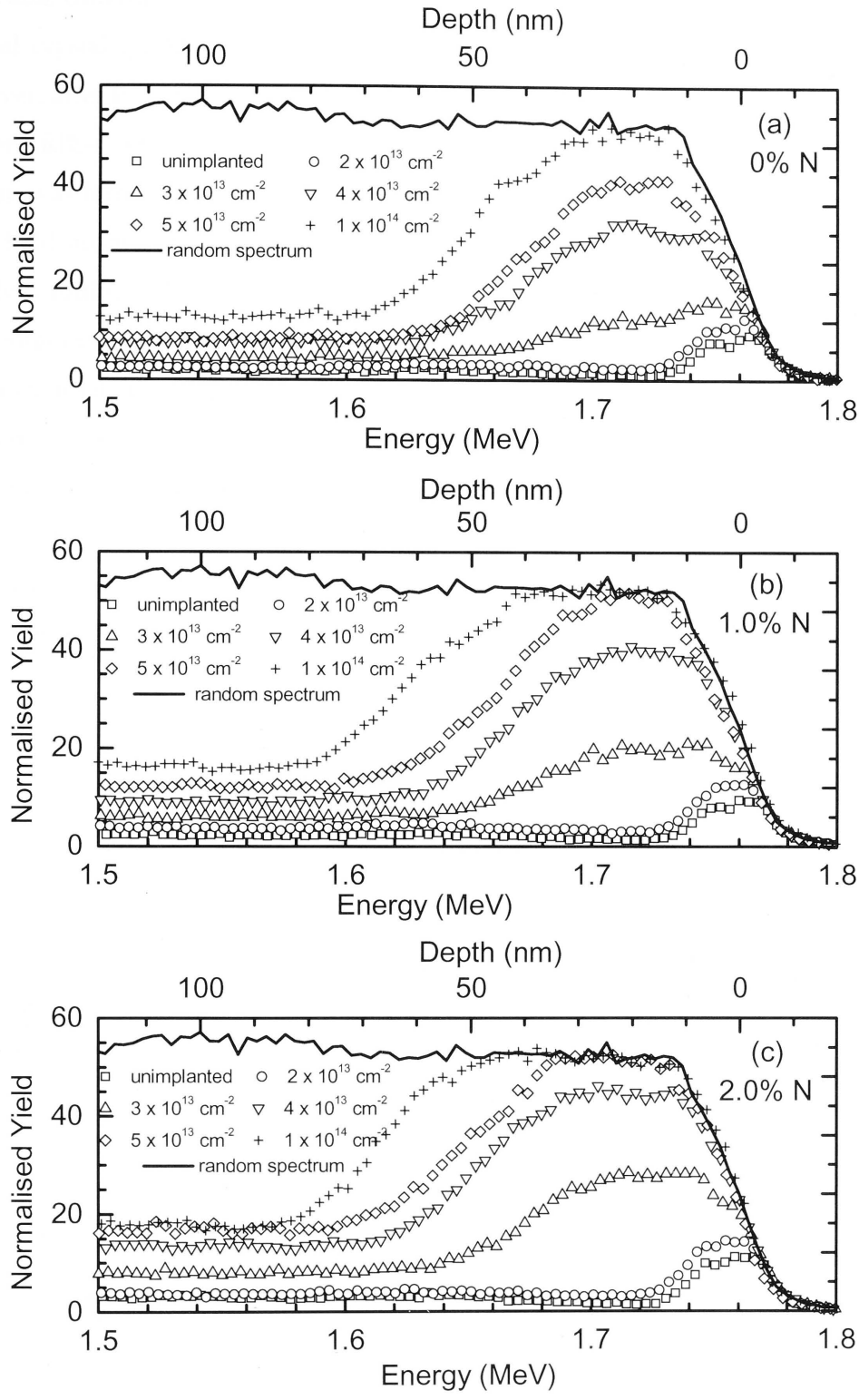

Fig. 5-2 RBS-channeling spectra showing the damage buildup at LN_2 temperature as a function of ion fluence for 50 keV Si^- implantation in $GaAs_{1-x}N_x$ epilayers with various N contents of (a) x = 0, (b) x = 1%, and (c) x = 2%, respectively.

observable difference) from all three unimplanted samples in Fig. 5-3. Therefore, the original crystal quality is same for these three samples in terms of RBS-C analysis. However, after implantation with 50 keV Si ion to 3 x 10^{13} cm^{-2}, these samples result in different RBS-C spectra as shown in Fig. 5-3. Obviously, higher density of damage buildup was formed in samples with higher N contents. The possible reason is that the strain field around N atoms may act as a sink for ion beam induced defects, subsequently resulting in higher density of damage buildup. Although there is no direct experimental evidence to support this speculation, it is quite reasonable. Considering N has much smaller atomic radius and higher electronegativity than As, substituting N for As in GaAs will inevitably result in a distorted lattice structure and a large strain field around N atoms. This distorted lattice structure and strain field will be enhanced by increasing N content and can more easily attract ion beam induced damage, such as vacancies and interstitials, thus rendering samples highly disordered at a lower ion fluence. However, more detailed studies are required to clarify this issue.

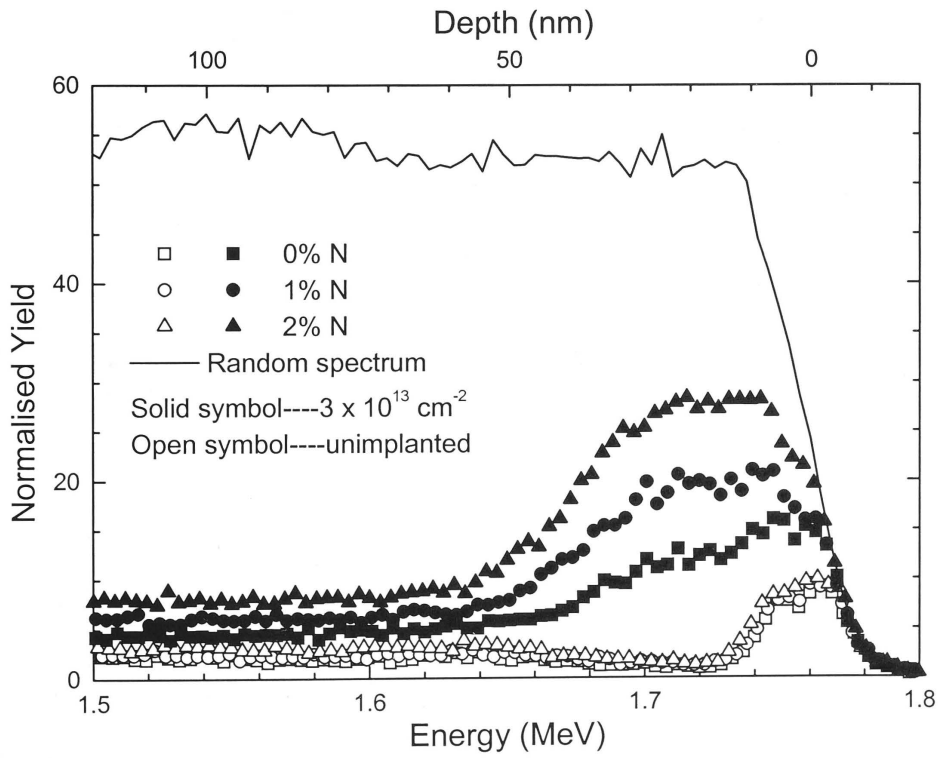

Fig. 5-3 RBS-channeling spectra of unimplanted (open symbol) and implanted (3 x 10^{13} cm^{-2}, solid symbol) GaAs, $GaAs_{0.99}N_{0.01}$ and $GaAs_{0.98}N_{0.02}$ samples. The random spectrum is also shown for comparison.

Effect of growth temperature

The second set of samples, which were grown at different temperatures with same N content (1% N), were also subjected to the same implantation process and RBS-C analysis. The RBS-C spectra of both unimplanted and implanted samples are shown in Fig. 5-4. It is obvious that there is no difference for all three samples. These results clearly demonstrate that grown-in defects caused by different growth temperatures used in this study have little effects on damage buildup behaviour in GaAsN epilayers.

In addition, it has been demonstrated that postgrowth annealing dramatically improved the PL properties of GaAsN alloys by many groups[7,10,13] and also shown in the previous chapters. To examine whether the postgrowth annealing will affect the amorphisation process in GaAsN layers or not, ion implantation and RBS-C analysis were also performed on the samples annealed at 750 °C for 30 s. Results showed no

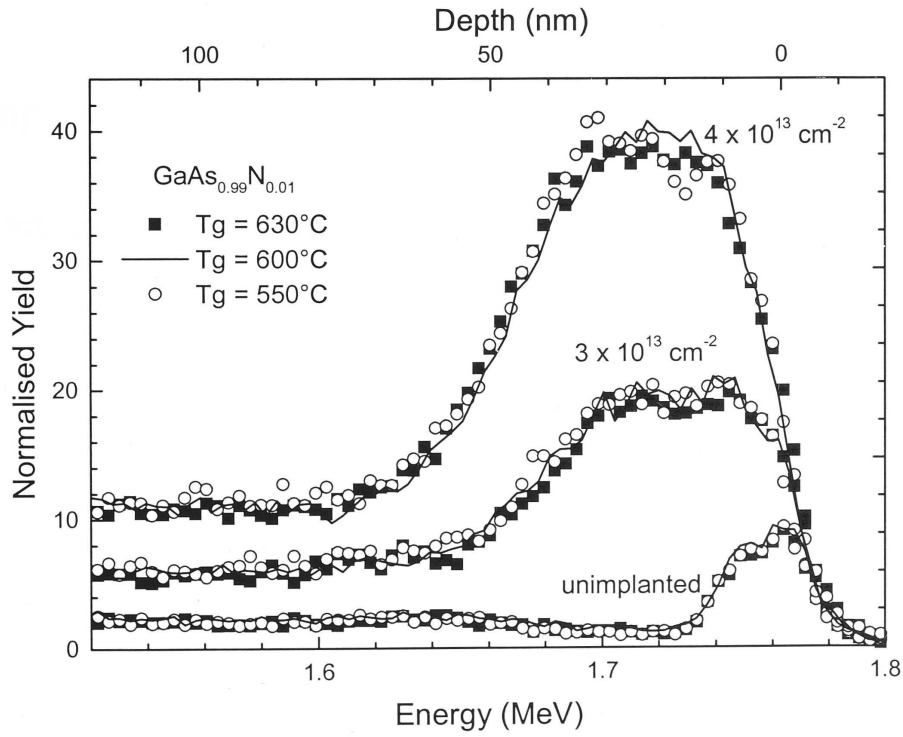

Fig. 5-4 RBS-channeling spectra of unimplanted (square) and implanted $GaAs_{0.99}N_{0.01}$ epilayers grown at different temperatures, Tg, as shown in the graph. Ion fluences for implanted samples are 3 x 10^{13} cm^{-2} and 4 x 10^{13} cm^{-2}, respectively.

observable effects from postgrowth annealing on the damage buildup process for all ion fluences ranging from 0 to 1 x 10^{14} cm^{-2} (RBS-C spectra are not shown). This further evidences that the grown-in defects in GaAsN epilayers do not play a significant role in the damage buildup process, although they affect the optical properties.

5.1.4 Conclusion

In summary, the ion damage buildup process in GaAsN epilayers with different N content and grown at different temperatures was investigated by RBS-channeling technique. Results show that the GaAsN epilayer becomes easier to amorphise with increasing N content, presumably due to the accumulation of ion beam induced defects in the strain field caused by N atoms. It was also demonstrated that the growth temperatures used in this study (550 - 630°C) and postgrowth annealing do not affect the damage buildup process, indicating grown-in defects in GaAsN epilayers do not play a major role in the amorphisation process.

5.2 Implant isolation of GaAsN epilayers

5.2.1 Introduction

Ion implantation induced damage is not always undesirable, in fact, it can be used to render a conducting layer highly resistive (i.e., electrical isolation) through the creation of free carrier trapping centres, and hence the term implant isolation.[14] Electrical isolation of III–V semiconductors is now perhaps the most important application of ion implantation in this group of materials, due to the widespread use of epitaxial growth techniques for obtaining doped layers. Selective masking of the semiconductor surface with photoresist followed by ion implantation has been a practical way to electrically isolate closely spaced electronic devices, including heterojunction bipolar transistors, impact avalanche transit time diodes, and metal-semiconductor field effect transistors (see, for example, Ref. 14). Moreover, implant isolation is also commonly used to manufacture optoelectronic devices, such as the gain guided, graded index separate confinement heterostructure GaAs/AlGaAs QW lasers,[14,15] and the vertical cavity surface emitting lasers.[16,17] In general, there are two mechanisms responsible for implantation-induced electrical isolation, which are carrier trapping at either damage-related

deep level centres (defect isolation) or at chemical deep-level states (chemical isolation).[14] Compared to the chemical isolation which requires high ion fluences and the high-temperature post-implantation annealing to obtain and activate enough chemical species, defect isolation using light ions (H^+, He^+, B^+, Li^+, C^+, or O^+) can be achieved in a single implantation step. Defect isolation is, therefore, the more attractive alternative for device fabrication purposes. Furthermore, implantation produces superior electrical isolation and preserves the semiconductor surface planarity compared to mesa etching.

In this study, single energy MeV ions were used to allow us to separate the effects of defect isolation from chemical isolation because most of the implanted ions are projected into the substrate. Single energy MeV ion implantation induced electrical isolation has worked very well in GaAs and AlGaAs epilayers with their relatively large band gaps.[18,19] However, it is less effective in InGaAs epilayers with smaller band gaps.[14] There has not been any report demonstrating implant isolation in GaAsN epilayers, which are p-type due to background doping during MOCVD growth and have smaller band gap than GaAs. In the following sections, the implant isolation of *p*-GaAsN epilayers is investigated for a wide range of ion species, free carrier concentrations, and N contents of epilayers. The implantation temperature is shown to have a negligible effect on electrical isolation and its thermal stability. The thermal stability of isolation in the unintentionally doped *p*-$GaAs_{0.986}N_{0.014}$ samples implanted with the different fluences and ion species is also discussed alongside the mechanism of defect isolation in p-GaAsN. In order to gain more insight into the mechanism of the isolation process, activation energies were extracted by performing extensive temperature dependent measurements of the sheet resistance of ion implanted samples to reveal the stages in the buildup of a stable implant isolation of *p*-GaAsN.

5.2.2 Experimental

Similar to samples used in previous works, an initial 250 nm thick GaAs buffer layer was grown and followed by a 500 nm thick *p*-type $GaAs_{1-x}N_x$ (x = 0.6%, 1.4%, and 2.3%) epilayer. All layers were grown at 600°C and 76 Torr. Due to the background doping such as carbon from the DMHy source, the undoped GaAsN epilayers are *p*-type in this study. To obtain higher *p*-type carrier concentrations, zinc doping was used during the growth. All the as-grown GaAsN samples were firstly annealed at

750°C for 30 s in a N_2 ambient using RTA to improve their crystal and optical quality.[13] Also, the postgrowth annealing was found to be able to recover the *p*-type free carrier concentration in GaAsN epilayers in our earlier work.[20] In this work, the RTA process at 750 °C for 30 s was used to obtain the highest free carrier concentration in all samples. DCXRD and PL measurements have indicated the high quality of the epilayers used in this study. The free carrier concentration was determined by ECV measurements. The annealed wafers were cleaved into rectangular pieces of 6 x 4 mm^2 for implantation. Ohmic contacts were prepared by manually applying indium (In) strips and sintering at 250°C for 2 minutes. The ohmic behaviour of the sintered In contacts has been verified by their linear current-voltage characteristics. These resistor-like samples were implanted in the ANU 1.7 MV tandem accelerator under ion irradiation conditions given in Table 5.1. The ion energies were chosen to create uniform ion-generated atomic displacement profiles throughout the conductive GaAsN layers and to place the damage peak deep in the SI-GaAs substrates. One example of the atomic displacement profiles calculated by TRIM code[8] is shown in Fig. 5-5. To minimise channeling effects, the samples were tilted by 7° off the surface normal direction. The sheet resistance (R_s) was measured *in-situ* after each fluence step by using a Keithley 617 electrometer. Post-implantation isochronal annealing cycles were carried out in the RTA furnace for 60 s at temperatures ranging from 100 to 700°C in a N_2 ambient. The annealing steps were accumulated in samples and R_s was measured at RT in the dark.

Table 5.1 Irradiation conditions used in this work. Calculated values of projected ion ranges (R_p) and the average numbers of displacement (N_d) produced by irradiated ions within 500 nm GaAsN epilayer using TRIM[8] code are also shown.

Ion	Energy (MeV)	Fluences ($10^{11}cm^{-2}$)	Beam flux (10^{11} $cm^{-2}s^{-1}$)	Irradiation Temperature (°C)	R_p (μm)	N_d (/ion)
$^1H^+$	0.6	2 - 6000	1.8	20	5.77	0.51
$^7Li^+$	0.7	0.5 - 70	1.6	20	1.86	36
$^{12}C^+$	2.0	0.2 - 66	1.3	-196 - 200	2.02	83
$^{16}O^+$	2.0	0.4 – 12	0.32	20	1.72	181

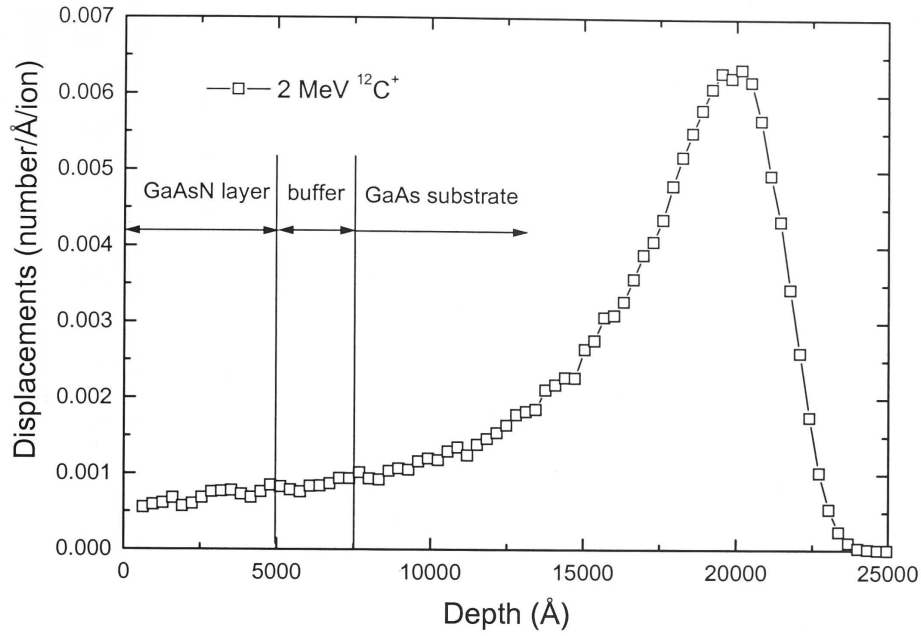

Fig. 5-5 Simulated profile of the displacement distribution in GaAsN/GaAs irradiated with 2 MeV C^{+} by TRIM code.[8]

5.2.3 Results and discussion

Effect of initial free hole concentration

Since it is desirable to have an estimate of the free carrier removal process during isolation for device fabrication purposes, investigating the effect of initial free carrier concentration on the isolation process is crucial. Figure 5-6(a) illustrates the evolution of sheet resistance (R_s) in both unintentionally doped (solid symbols) and Zn-doped (open symbol) GaAsN samples during 2 MeV $^{12}C^{+}$ ion implantation at RT (20°C). Each of the curves in Fig. 5-6(a) presents three distinct regions. The first region comprises the lowest fluences where R_s increases only slightly with fluence. The second region is characterised by a sharp increase of R_s by 5-6 orders of magnitude in a relatively narrow fluence interval. Such an increase of R_s is typically resulted from the carrier trapping and carrier mobility degradation caused by irradiation-induced damage.[14] Similar behaviour was observed in all samples, but the characteristic ion fluence, F_{th} (hereafter called threshold fluence) required to achieve the maximum R_s is shifted to the higher fluences with the increasing initial free hole concentration p. The maximum

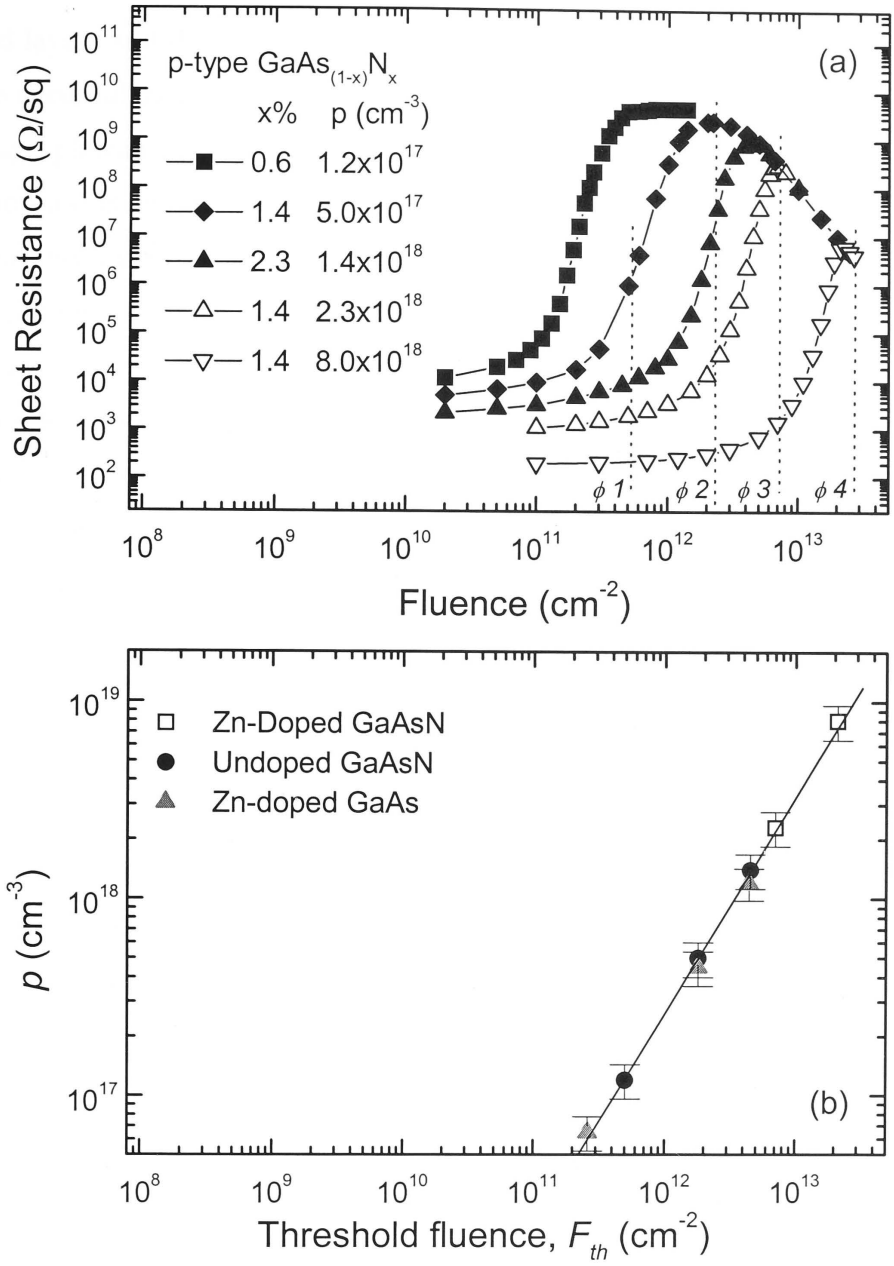

Fig. 5-6 (a) Sheet resistance *vs* accumulated fluence in *p*-type $GaAs_{1-x}N_x$ epilayers with different N contents *x* and free hole concentrations *p* during 2 MeV $^{12}C^+$ implantation. Four final fluences (ϕ_1, ϕ_2, ϕ_3, and ϕ_4) used for the later thermal stability study are also indicated in the graph. (b) Free hole concentration *p* *vs* threshold fluence F_{th} obtained from data in (a). The solid line with a slope of 1.1 ± 0.03 is the best linear fit through the data points. The data from Zn-doped GaAs are also shown for comparison.

value of the sheet resistance results from the parallel association of the resistances in isolated layers and the underneath GaAs substrate. The third region is formed by the fluence accumulation beyond F_{th}. In this region, R_s remains approximately constant forming a plateau up to 1.4 x 10^{12} cm^{-2} for $GaAs_{0.994}N_{0.006}$ sample, where the free hole concentration is about 1.2 x 10^{17} cm^{-3}. However, the plateau was not observed and R_s decreases with further fluence accumulation for all the other samples that have both higher N content (≥ 1.4% N) and higher free hole concentration (≥ 5.0 x 10^{17} cm^{-3}). This is because when the accumulated fluence is high enough, defect assisted hopping conduction[21] leads to reduction in the sheet resistance. It is also worth stressing that the maximum R_s decreases with increasing N content or initial hole concentration, due to the competition between carrier trapping effects and hopping conduction effects from the implantation-induced defects.

The relationship between the initial free carrier concentration and the threshold fluence [taken from Fig. 5-6(a)] for isolation is shown Fig. 5-6(b). The data of Zn-doped GaAs is also shown in Fig. 5-6(b) for comparison. The solid line is the least squares fit through all data points and has a slope of 1.10 ± 0.03. All the data from epilayers including Zn-doped GaAs, unintentionally doped GaAsN and Zn-doped GaAsN fit this straight line very well, indicating that F_{th} depends nearly linearly on the original free carrier concentration does not solely depend on the N content. It is also noticed that F_{th} of GaAs and GaAsN layers with similar free carrier concentration overlaps with each other, further confirming that N content alone does not affect F_{th} in the isolation process. It is worth noting here that the threshold fluence for amorphisation is found to decrease with increasing N content. However, one must note these two facts: (i) the ion beam (50 keV Si^-) used in amorphisation studies produces much denser damage in GaAsN layers than 2 MeV C^+ used here (see Figs. 5-1 and 5-5); (ii) the ion fluences causing amorphisation are much higher than that for isolation. Therefore, the defects responsible for the amorphisation and the electrical isolation processes are expected to be different, hence the different dependencies on N composition. Similar results were also reported in AlGaAs alloy system, where Al content greatly affected the amorphisation process,[4] but did not affect the electrical isolation process.[19]

Effect of ion mass

Figure 5-7(a) shows the evolution of R_s of unintentionally doped GaAsN (1.4% N) epilayers irradiated with 0.6 MeV $^1H^+$, 0.7 MeV $^7Li^+$, 2.0 MeV $^{12}C^+$, or 2.0 MeV $^{16}O^+$ at RT. It is obvious that F_{th} shifts to lower fluences with increasing ion mass. This phenomenon is related to the fact that at a given ion fluence, heavier particles create higher concentrations of atomic displacements in the GaAsN epilayers. The exact nature of this ion mass dependence is better understood by plotting the total number of displacements (N_d, calculated using the TRIM code[8]) created by each ion within the 500 nm thick GaAsN layer as a function of F_{th}, as shown in Fig. 5-7 (b). The best linear-fit line with a slope of -1.07 ± 0.01 indicates that the threshold fluence for isolation is inversely proportional to the total number of defects created by the implanted ions, regardless of ion mass for the conditions used in this study. It is suggested that changing the density of atomic displacements by varying the ion energy should still result in F_{th} falling on this straight line, similar to our recent results on *p*-type GaAs.[22]

The above results show that ion fluences required for an effective electrical isolation of GaAsN epilayers have simple linear and inverse dependencies on the original free carrier concentration and ion-beam-produced atomic displacements, respectively. As a result, implant conditions at RT necessary for an effective electrical isolation of a particular GaAsN-based device can be readily estimated based on experimental data presented here.

Effect of implant temperature

It is well established that the dynamic annealing of point defects in GaAs depends strongly on the implantation temperature.[23,24] Furthermore, isochronal annealing studies indicated that point defects created in electron- and γ-irradiated GaAs at fairly low doses anneal in three well defined stages between 235 and 500 K (i.e., -38 - 227°C).[25-27] On the other hand, the defects created in GaAs by ion implantation to moderate doses (<1 x 10^{14} cm^{-2}) anneal predominantly at the 225°C (stage III) and 400 °C (stage IV) characteristic stages, with the lower annealing temperature related to the mobility of individual point defects, such as the arsenic interstitial, As_i or arsenic vacancy, V_{As}.[25,28,29] Yet another stage in the vicinity of 600-700°C has been observed for defect annealing in high dose ion implanted GaAs.[25] This particular annealing stage can be related to the removal of defect clusters or extended defects, which coincides well with

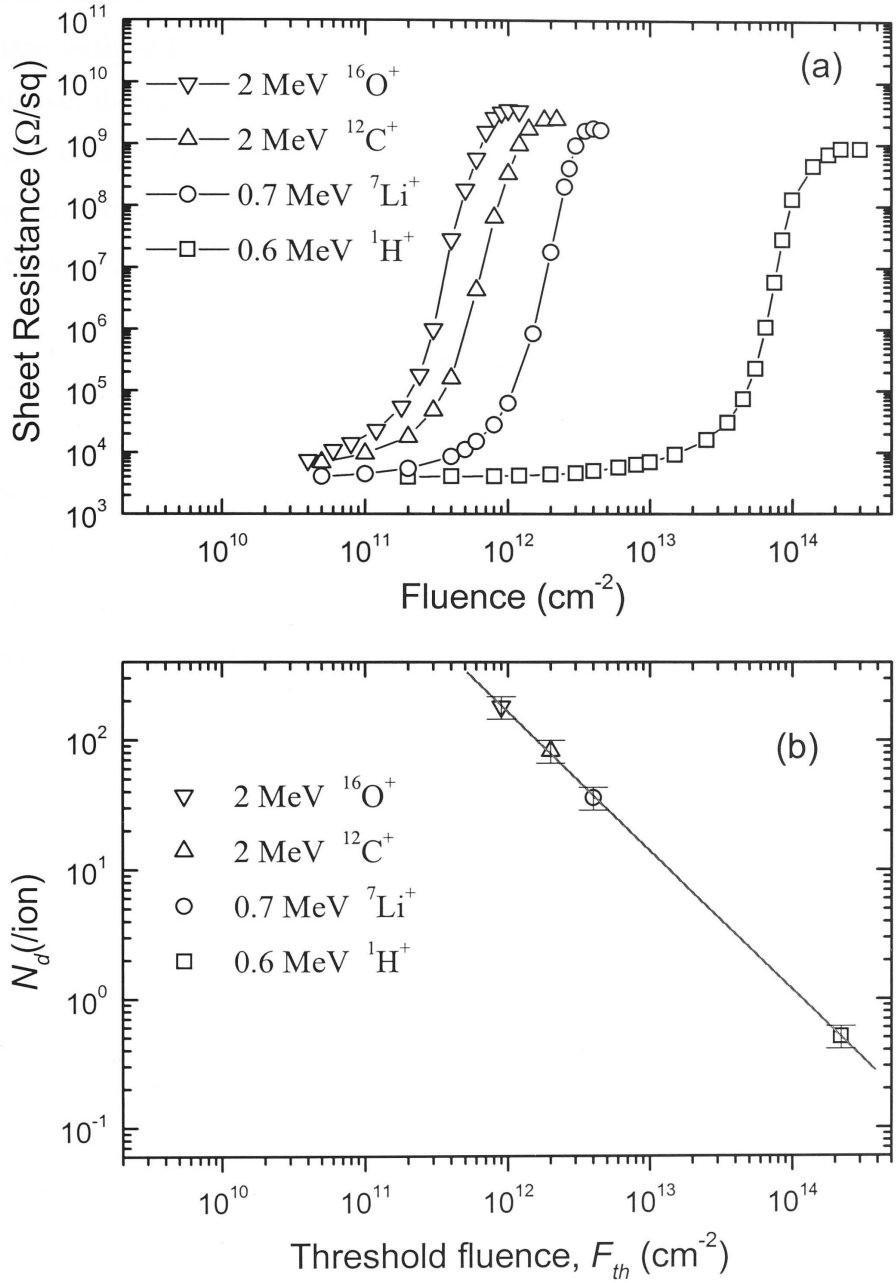

Fig. 5-7 (a) Fluence dependence of sheet resistance in the unintentionally doped $GaAs_{0.986}N_{0.014}$ epilayers with free hole concentration of 5 x 10^{17} cm^{-2} exposed to ^{16}O, ^{12}C, ^{7}Li and ^{1}H ions. (b) Threshold fluence *vs* the number of displacements, N_d, produced by implanted ions. The solid line with a slope of -1.07 ± 0.01 is the best linear fit through the data points.

the second stage of the solid phase epitaxial regrowth of amorphous GaAs produced by ion implantation.[25,30,31] Moreover, because the implant isolation processes are very similar in GaAs and GaAsN, and, we noticed in the earlier RBS-C studies that the implantation with 50 keV Si ions (which produces much higher density of defects in the GaAsN layer than 2 MeV C^+ used here) up to a fluence of $2 \times 10^{13} cm^{-2}$ did not cause any difference in the damage buildup process in GaAsN and GaAs layers, therefore the implantation-induced defects responsible for electrical isolation are assumed to be comparable in GaAs and GaAsN.

With the above general guideline for defect annealing in mind, an investigation of the effect of substrate temperature during implantation is important to understand defect-related isolation mechanisms. Such experiments are able to provide insight into the type of defects (i.e., point defects versus defect clusters) responsible for the electrical isolation of *p*-GaAsN. Figure 5-8 illustrates the evolution of R_s for the unintentionally doped $GaAs_{0.986}N_{0.014}$ samples with free hole concentration of 5.0×10^{17} cm^{-3} exposed to 2 MeV C ions at temperatures ranging from -196 to 200 °C. The reduction in

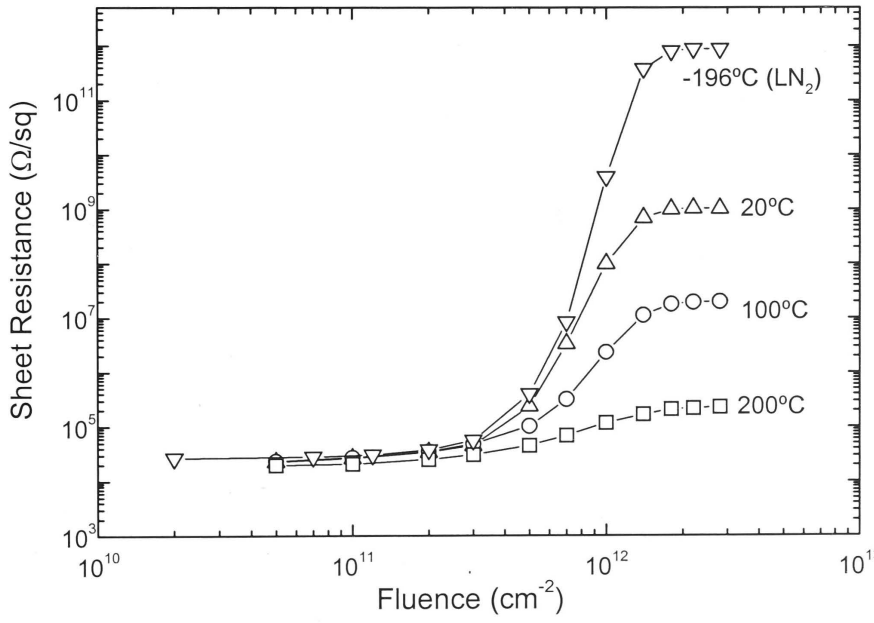

Fig. 5-8 Evolution of sheet resistance for the unintentionally doped *p*-$GaAs_{0.986}N_{0.014}$ samples with free hole concentration of 5.0×10^{17} cm^{-3} exposed to 2 MeV C ions at temperatures ranging from -196 to 200 °C.

the maximum value of R_s that is reached with the increasing substrate temperature during implantation can be attributed to the increased ionisation of holes trapped at defect centres at higher temperatures. After implantation, these samples were measured again at room temperature and the R_s values were similar (~ 2 x 10^9 Ω/sq) for all samples, indicating the similar isolation result has been obtained in all these samples. The curves in Fig. 5-8 clearly show that R_s starts to increase at the same ion fluence of ~ 5 x 10^{11} cm^{-2} irrespective of the substrate temperature during implantation. Furthermore, the saturation in R_s appears to occur in the same ion fluence regime for all the implantation temperatures, i.e., ~(1.8 - 2.2) x 10^{12} cm^{-2}. The results shown in Fig. 5-8 are qualitatively similar to those reported previously for implant isolation of *n*-type GaAs when no significant influence of substrate temperature on the isolation process was observed in the range -100 - 220°C.[23] It can, therefore, be concluded from the above discussion that the defects responsible for the stability of implant isolation in *p*-GaAsN are not simple point defects (i.e., Frenkel-type defects, such as vacancies and interstitials) but rather defect clusters or complexes that have a higher thermal stability.

Thermal stability and stages in the buildup of electrical isolation

The thermal stability of implant isolation is a critical issue to consider in device applications. In particular, maximising the thermal stability of the implant isolation is desirable. In this section, detailed discussions of the effects of ion fluence and ion species on the thermal stability of implant isolation are presented. This study provides much insight into the types of defects that contribute to the isolation based on their annealing behaviour. Further information on the buildup of a stable isolation with the increasing ion fluence is also obtained through temperature dependent measurements of the sheet resistance of implanted samples both before and after annealing. Since the nitrogen is known to mainly affect the conduction band of (In)GaAsN alloys and thus the offset of valence band between GaAsN and GaAs is very small,[32-34] therefore the origins of defects in p-GaAsN are discussed in comparison with those in p-GaAs.

Figure 5-9 illustrates the thermal stability of isolation for layers implanted with 2 MeV C ions at 20 °C to fluences ranging from 0.25F_{th} (1.0 x 10^{12} cm^{-2}) to 12.5F_{th} (2.5 x $10^{13}cm^{-2}$). Each data point on the curves in Fig. 5-9 comprises the cumulative isochronal annealing sequence for 60 s periods in the RTA. It is obvious from Fig. 5-9 that the

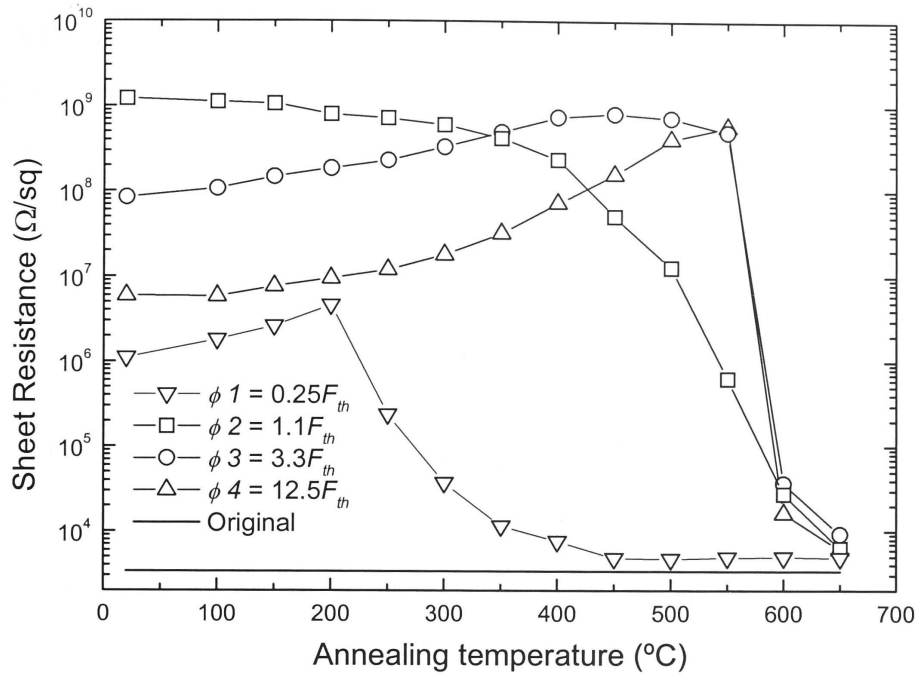

Fig. 5-9 Isochronal annealing stability of the electrical isolation in the unintentionally doped *p*-$GaAs_{0.986}N_{0.014}$ epilayers implanted with 2 MeV $^{12}C^+$ at RT to final fluences ranging from $0.25F_{th}$ to 12.5 F_{th} as indicated in Fig. 5-6.

thermal stability of isolation depends critically on the final ion fluence ϕ. An increase in R_s is observed for the sample bombarded to 0.25 F_{th} in the temperature range 20–200°C. This effect is similar to that observed in a previous report of the thermal stability of isolation in H implanted *p*-GaAs.[35] Two possible scenarios for this increase in R_s during annealing between 20 and 200 °C can be envisaged, namely (a) the formation of more efficient hole trapping centers due to interaction of point-like defects and/or (b) the increase in the concentration of existing hole trapping centers. Indeed, a previous investigation of the annealing of defects created in electron irradiated *p*-GaAs epilayers has demonstrated that a hole trap *P1* (E_V + 0.36 eV) is created upon annealing at the expense of electron traps that are produced initially by primary collisions, and its concentration increased upon annealing up to 280 °C.[26] Annealing of the GaAsN epilayer implanted to $0.25F_{th}$ above 200 °C results in the gradual recovery of free carriers most probably due to annealing of point-like defects similar to the characteristic stage III annealing of defects in *p*-GaAs.[25-29]

The sheet resistance of the GaAsN epilayer implanted to $1.1F_{th}$ is thermally stable up to ~400°C above which it decreases rapidly with the increasing annealing temperature. It becomes clear from the above discussion that the defects responsible for the electrical isolation of the sample bombarded to $1.1F_{th}$ anneal in the characteristic stage IV typical of samples implanted to moderate fluences.[25,28,29] The defects responsible for free carrier trapping in the sample implanted to $1.1F_{th}$ are most probably defect pairs, resulting from the interactions of vacancies, interstitials, and impurities, rather than simple isolated defects.[27] Bombarding the *p*-GaAsN epilayer to $3.3F_{th}$ enhances the thermal stability of isolation up to 550°C, which is sufficient for most device application purposes. The initial increases in sheet resistance of the samples implanted to $3.3F_{th}$ and $12.5F_{th}$ with the increasing temperature are resulted from the recovery of hopping conduction. Defects are removed with the increasing temperature so that the spatial distribution of defect potential wells that trap free carriers decreases. The maximum R_s is reached at 550°C when hopping conduction is completely eliminated, while the concentration of defects responsible for hole trapping is of the same order of magnitude as the initial free carrier concentration. These defects are removed by annealing above 550°C, which would correspond to the annealing of defect clusters or defect complexes in GaAs.[25,27] A recent study has proposed that the double donor As_{Ga} (EL2 defect with an energy position of E_V + 0.54 eV in the band gap) could be a suitable candidate for the defect responsible for the stability of isolation in *p*-GaAs.[18,36] Indeed, it has been reported that the EL2 introduced in neutron-irradiated, plastically deformed, or low-temperature grown GaAs by molecular beam epitaxy, anneal in the temperature range of 450–600 °C.[37,38] More recently, Tan *et al.*[39] have shown that the excess EL2 created by proton implantation of GaAs epilayers grown by MOCVD was stable only up to 500 °C, which correlates very well with the temperature window within which the isolation of C-implanted *p*-GaAsN becomes unstable (Fig. 5–9). These results are in good agreement with those depicted in Fig. 5–8, when it was concluded that the defects responsible for stable isolation could not be simple point-defects. Therefore, it can be concluded from Fig. 5–9 that an ion fluence of $3.3F_{th}$ is sufficient for creating a stable isolation in *p*-GaAsN.

Further insight into the buildup of stable electrical isolation with the increasing ion dose is obtained by measuring the temperature dependence of R_s. Figure 5–10(a) illustrates the Arrhenius-like dependence of R_s on the inverse of measurement

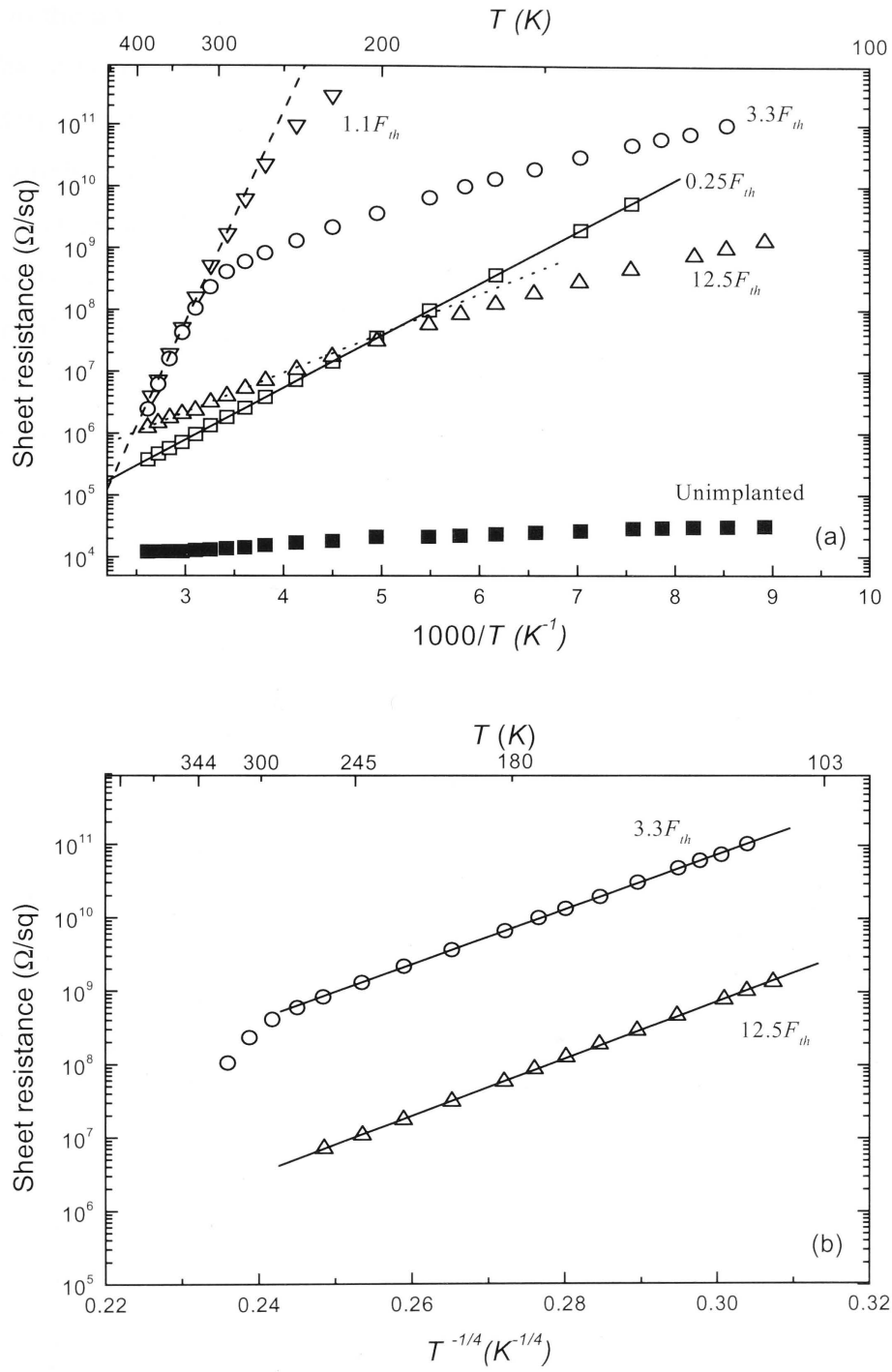

Fig. 5-10 (a) Arrhenius-like dependence of $\ln(R_s)$ of the unintentionally doped *p*-$GaAs_{0.986}N_{0.014}$ epilayers implanted with 2 MeV $^{12}C^+$ *vs* $1/T$ for the different ion fluences marked on the curves, and (b) temperature variation of sheet resistance of C^+-implanted layers to fluences marked on the curves plotted as $\ln(R_s)$ versus $T^{-1/4}$.

temperature, T, for the unintentionally doped p-$GaAs_{0.986}N_{0.014}$ layers implanted with 2 MeV C^+ to different fluences at 20 °C. The data points shown in solid squares correspond to the unimplanted sample, and they do not reveal any striking feature. However, the curve for $0.25F_{th}$ (open squares) exhibits a single regime which can be well described by a least squares fit. This fit yields an activation energy of (0.17 ± 0.01 eV), indicating only one type of defect is responsible for the isolation process of a layer implanted to $0.25F_{th}$. This activation energy is most probably related to the ionisation of holes to the valence band, as opposed to thermally activated inter-defect hopping conduction. Conducting p-GaAsN epilayers implanted to $1.1F_{th}$ or $3.3F_{th}$ exhibit two temperature regimes. An Arrhenius-like dependence of $\ln(R_s)$ on $1/T$ is observed only at T > 280 K for the sample implanted to $1.1F_{th}$ and at T > 310 K for the sample implanted to $3.3F_{th}$, respectively. The dashed line is the linear regression through these data points, which yields an activation energy of (0.68 ± 0.03 eV) for the process. For the sample implanted to $3.3F_{th}$, at T < 310 K, the data points are well described by a linear relationship between $\ln(R_s)$ and $T^{-1/4}$ [Fig. 5-10(b)], which is characteristic of the hopping conduction mechanism between localised defect states near the Fermi level as proposed by Mott.[21,40,41] The GaAsN epilayer implanted to the highest fluence of $12.5F_{th}$ is heavily damaged as demonstrated by the hopping conduction mechanism in it [Fig. 5-10(a) and (b)]. In the higher temperature (T > 250 K) range, the slope of the Arrhenius plot [Fig. 5-10(b)] yields an activation energy of (0.12 ± 0.02 eV), which is in good agreement with the value obtained for Te-implanted GaAs to high doses.[41] At temperatures below 250 K, the R_s curve can be better fitted to the Mott relationship for hopping conduction [Fig. 5-10(b)]. Based on the results (Fig. 5-9 and 5-10) and discussions above, it can be conclude that isolated point defects which are thermally stable up to ~200°C are responsible for free carrier trapping at the low ion fluences (~$0.25F_{th}$), while point defect pairs (stable up to ~400°C) are likely to cause isolation in the intermediate fluence (~F_{th}) regime.

We now turn to the influence of the ion species on the thermal stability of isolation in p-GaAsN. Figure 5-11(a) illustrates the change of R_s for H- (open squares), C- (closed circles), and O-implanted (closed triangles) unintentionally doped p-$GaAs_{0.986}N_{0.014}$ samples to 1.1 times their corresponding threshold fluences, F_{th}. All three samples implanted at 20 °C demonstrate the similar thermal stability of isolation. It is pointed out here that similar annealing behaviour was observed for samples

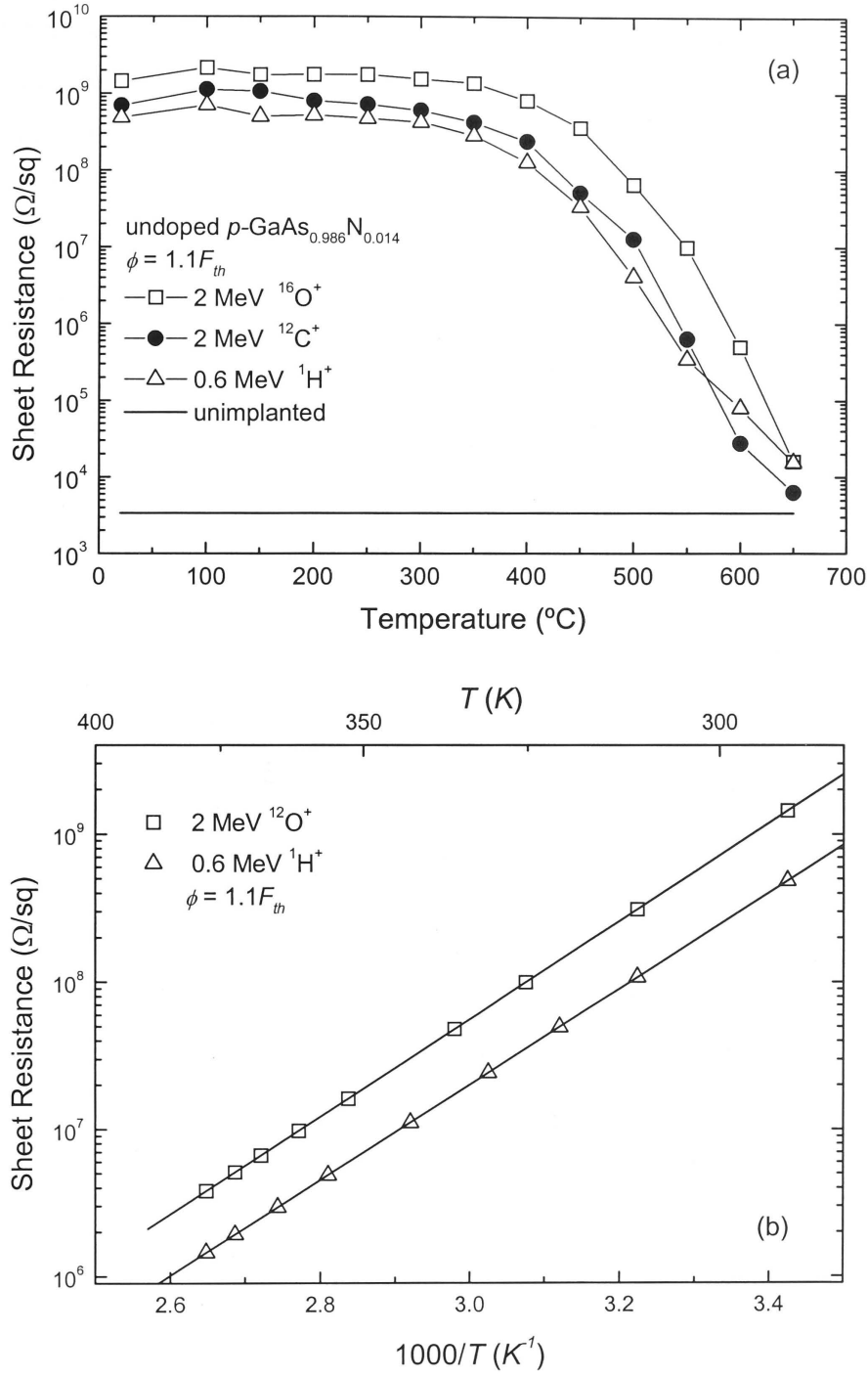

Fig. 5-11 (a) Isochronal annealing stability of isolation in the unintentionally doped p-$GaAs_{0.986}N_{0.014}$ epilayers implanted with 2 MeV O^+, 2 MeV C^+, and 0.6 MeV H^+ at RT to 1.1 times their corresponding threshold fluences, F_{th}. (b) The variation of $\ln(R_s)$ as a function of $1/T$ for H^+- and O^+-implanted samples yielding activation energies of (0.66 ± 0.03 eV) and (0.67 ± 0.03 eV), respectively.

implanted at -196, 20, 100, or 200°C (results are not shown), which was further evidence that the implantation temperature did not play a significant role in the isolation process. Figure 5-11(b) shows the variation of $\ln(R_s)$ as a function of $1/T$ for the H^+- and O^+-implanted samples (i.e., the lightest and heaviest ion species used in this study) for temperatures above 290 K when the trapped carriers become thermally activated. The least squares fits through the data points shown as solid lines in Fig. 5-11(b) yield activation energies of (0.66 ± 0.03 eV) and (0.67 ± 0.03 eV) for the isolation process by H^+ and O^+ implantation, respectively. It is timely here to remind the reader that an activation energy of (0.68 ± 0.03 eV) was obtained from Fig. 5-10(a) for C^+ implantation. The similar activation energies for the different ions indicate the absence of an ion mass effect on the isolation process, which is supported by the earlier discussion of the results in Fig. 5-7. The crux of the implant isolation process is the nuclear energy deposited in elastic recoils within the conducting layer. In a previous study of the long-term thermal stability of implant-isolated *p*-GaAs, Ren et al.[42] extracted different activation energies for the isolation of H- and F-implanted *p*-GaAs. Following their results, it was concluded that the ion mass played a role in the thermal stability of isolation. The discrepancy between the results reported here and those in Ref. 42 can be explained by the different implantation schemes employed in the two studies. It is believed that the types and concentration of defects created by the multiple implantations in Ref. 42 were different for H- and F-ion implantation, as opposed to the single ion implantation scheme used here to create a uniform defect profile within the conducting *p*-GaAsN layers. The absence of an ion mass effect has previously been reported for the implantation isolation of *n*-GaAs layers.[43]

5.2.4 Conclusion

In summary, *p*-GaAsN epilayers grown by MOCVD with different N contents and doped to different concentrations of Zn were used to study the formation of implant isolation for a wide range of ions. The result clearly demonstrated that the threshold fluence for implant isolation in *p*-GaAsN epilayers depends close-to-linearly on the initial free hole concentration and inversely on the concentration of atomic displacements produced by the ion beams. It was also found that the threshold fluence does not solely depend on the N composition, indicating the defects responsible for the electrical isolation are different from the defects causing amorphisation in the GaAsN epilayers.

The isolation process was determined predominantly by the nuclear energy deposited in elastic recoils during implantation. This is evidenced by the similar activation energy for isolation obtained by H, C, and O ion implantation, and the similar thermal stability of isolation of *p*-GaAsN epilayers bombarded with different ions during post-implantation isochronal annealing. The buildup of isolation with the fluence of 2 MeV C ions follows the creation of (i) point defects for $\phi \sim 0.25F_{th}$, (ii) defect pairs for $\phi \sim 1.1F_{th}$, and (iii) defect clusters or complexes (e.g., As_{Ga}) that are stable at 550°C for the higher ion fluences. The substrate temperature (-196–200°C) during implantation did not have any bearing on the isolation process, demonstrating that point-like defects do not contribute to the stability of implant isolation of *p*-GaAsN.

References

1 K. Matsui, T. Takamori, T. Fukunaga, T. Narusawa, Y. Bamba, and H. Nakashima, Jpn. J. Appl. Phys. **25,** L391 (1986).

2 I. Jencic, M. W. Bench, I. M. Robertson, and M. A. Kirk, J. Appl. Phys. **69,** 1287 (1991).

3 B. A. Turkot, D. V. Forbes, I. M. Robertson, J. J. Coleman, L. E. Rehn, M. A. Kirk, and P. M. Baldo, J. Appl. Phys. **78,** 97 (1995).

4 H. H. Tan, C. Jagadish, J. S. Williams, J. Zou, D. J. H. Cockayne, and A. Sikorski, J. Appl. Phys. **77,** 87 (1995).

5 H. H. Tan, C. Jagadish, J. S. Williams, J. Zou, and D. J. H. Cockayne, J. Appl. Phys. **80,** 2691 (1996).

6 S. O. Kucheyev, J. S. Williams, C. Jagadish, J. Zou, and G. Li, Phys. Rev. B **62,** 7510 (2000).

7 I. A. Buyanova, W. M. Chen, G. Pozina, P. N. Hai, B. Monemar, H. P. Xin, and C. W. Tu, Mater. Sci. Eng. B **82,** 143 (2001).

8 J. F. Ziegler, J. P. Biersack, and U. Littmark, *The Stopping and Range of Ions in Solids,* Vol. 1 (Pergamon, Oxford, 1985).

9 L. C. Feldman, J. W. Mayer, and S. T. Picraux, *Materials Analysis by Ion Channeling* (Academic Press, New York, 1982).

10 S. Francoeur, G. Sivaraman, Y. Qiu, S. Nikishin, and H. Temkin, Appl. Phys. Lett. **72,** 1857 (1998).

11 A. Moto, M. Takahashi, and S. Takagishi, J. Cryst. Growth **221,** 485 (2000).

12 A. Moto, S. Tanaka, N. Ikoma, T. Tanabe, S. Takagishi, M. Takahashi, and T. Katsuyama, Jpn. J. Appl. Phys. Part 1 **38,** 1015 (1999).

13 E. V. K. Rao, A. Ougazzaden, Y. Lebellego, and M. Juhel, Appl. Phys. Lett. **72,** 1409 (1998).

14 S. J. Pearton, Mater. Sci. Rep. **4,** 313 (1990), and references therein.

15 K. Berthold, A. F. J. Levi, S. J. Pearton, R. J. Malik, W. Y. Jan, and J. E. Cunningham, Appl. Phys. Lett. **55,** 1382 (1989).

16 G. Dang, B. Luo, F. Ren, W. S. Hobson, J. Lopata, S. N. G. Chu, and S. J. Pearton, Electrochem. Solid-State Lett. **4,** G112 (2001).

17 M. Y. A. Raja, Y. Cao, G. H. Cooper, A. S. Al-Dwayyan, and C. X. Wang, Opt. Eng. (Bellingham) **41,** 704 (2002).

18 H. Boudinov, A. V. P. Coelho, and J. P. de Souza, J. Appl. Phys. **91,** 6585 (2002).

[19] T. v. Lippen, H. Boudinov, H. H. Tan, and C. Jagadish, Appl. Phys. Lett. **80,** 264 (2002).

[20] Q. Gao, H. H. Tan, C. Jagadish, and P. N. K. Deenapanray, Jpn. J. Appl. Phys., Part 1 **42,** 6827 (2003).

[21] Y. Kato, T. Shimada, Y. Shiraki, and K. F. Komatsubara, J. Appl. Phys. **45,** 1044 (1974).

[22] P. N. K. Deenapanray, Q. Gao, and C. Jagadish, J. Appl. Phys. **93,** 9123 (2003).

[23] J. P. de Souza, I. Danilov, and H. Boudinov, J. Appl. Phys. **84,** 4757 (1998).

[24] T. E. Hayes and O. W. Holland, Appl. Phys. Lett. **59,** 452 (1991).

[25] D. V. Lang, Inst. Phys. Conf. Ser. **31,** 70 (1977).

[26] D. Pons, A. Mircea, and J. Bourgoin, J. Appl. Phys. **51,** 4150 (1980).

[27] D. Pons and J. C. Bourgoin, J. Phys. C **18,** 3839 (1985).

[28] J. C. Bourgoin, H. J. von Bardeleben, and D. Stiévenard, J. Appl. Phys. **64,** R65 (1988).

[29] D. Stiévenard, X. Boddaert, and J. C. Bourgoin, Phys. Rev. B **34,** 4048 (1986).

[30] J. S. Williams, in *Laser Annealing of Semiconductors,* edited by J. M. Poate and J. W. Mayer (Academic, New York, 1982), p. 383, and references therein.

[31] S. S. Kular, B. J. Sealy, K. G. Stephens, D. K. Sadana, and G. R. Booker, Solid-State Electron. **23,** 831 (1980).

[32] M. Kondow, K. Uomi, A. Niwa, T. Kitatani, S. Watahiki, and Y. Yazawa, Jpn. J. Appl. Phys., Part 1 **35,** 1273 (1996).

[33] P. Krispin, S. G. Spruytte, J. S. Harris, and K. H. Ploog, J. Appl. Phys. **89,** 6294 (2001).

[34] B. Q. Sun, D. S. Jiang, Z. Pan, L. H. Li, and R. H. Wu, Journal of Crystal Growth **227,** 501 (2001).

[35] J. P. de Souza, I. Danilov, and H. Boudinov, Radiat. Eff. Defects Solids **147,** 109 (1998).

[36] J. Lagowski, D. G. Lin, T.-P. Chen, M. Skowronski, and H. C. Gatos, Appl. Phys. Lett. **47,** 929 (1985).

[37] R. Wörner, U. Kaufman, and J. Schneider, Appl. Phys. Lett. **40,** 141 (1982).

[38] M. Kaminska and E. R. Weber, Mater. Sci. Forum **83-87,** 1033 (1992).

[39] H. H. Tan, J. S. Williams, and C. Jagadish, J. Appl. Phys. **78,** 1481 (1995).

[40] N. F. Mott, J. Non-Cryst. Solids **1,** 1 (1968).

[41] B. K. Shin, J. Appl. Phys. **47,** 3612 (1976).

[42] F. Ren, S. J. Pearton, C. R. Abernathy, P. W. Wisk, T. R. Fullowan, J. R. Lothian, and R. Esagui, Semicond. Sci. Technol. **8,** 605 (1993).

[43] J. P. de Souza, I. Danilov, and H. Boudinov, J. Appl. Phys. **81,** 650 (1997).

CHAPTER 6

Intermixing in InGaAsN quantum dots

6.1 Introduction

It is well known that for monolithic integration of optoelectronic devices, the ability to selectively engineer the bandgap of the semiconductor heterostructure, such as QW and QD, across a wafer is of prime importance. There are two approaches to achieve this purpose. One option is to use masking, etching, and regrowth techniques to achieve different material structure in selected areas. The growth and processing conditions are very critical to achieve high quality heterostructures and reproducible results. A different approach is to use postgrowth intermixing/interdiffusion technique, which is a powerful tool and much easier to realise compared with the regrowth technique. This technique relies on the interdiffusion of atoms of the QW and barrier layers, leading to the modification of QW potential profile,[1] as shown schematically in Fig. 6-1. Various methods have been used to create the atomic interdiffusion, such as impurity-induced intermixing,[2] implantation-induced intermixing,[3,4] and impurity free vacancy disordering (IFVD).[5-7] Among these techniques, IFVD is probably the most widely used method because it does not create excessive damage and retain the high crystal quality of the sample.[6]

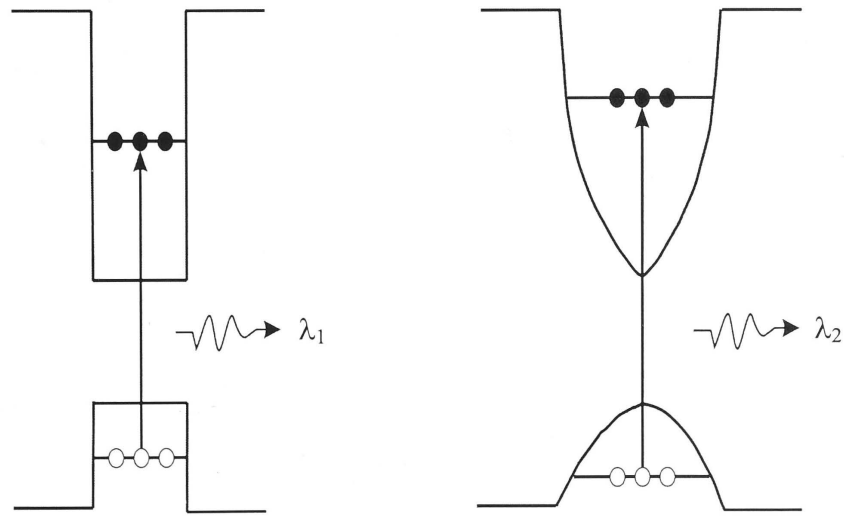

Fig. 6-1 Modification of the shape of a QW potential profile due to intermixing, which results in an increased transition energy from the conduction band to the valence band. (i.e., $\lambda_1 > \lambda_2$).

In most cases, intermixing is an approach to achieve a blueshift of the bandgap. However, it has been found that post-growth annealing leads to a significant blueshift of the emission wavelength from InGaAs/GaAs QDs.[8,9] Similar behaviour was also observed for InGaAsN QDs during rapid thermal annealing (RTA) in this work. This uncontrolled thermal interdiffusion is problematic when fairly precise wavelength is required and is not favourable for the device integration, which needs spatially controlled bandgap modification. So it is highly desirable to suppress the thermal interdiffusion in InGaAsN/GaAs QD structures.

In this chapter, TiO_2 and SiO_2 layers of different thicknesses were deposited on the surface of the InGaAsN/GaAs QD samples. After RTA at various temperatures for 30 s, effective suppression of thermal interdiffusion and controlled blueshift of the PL peak have been observed by using the cap of TiO_2 layer. Enhancement of interdiffusion by SiO_2 layer was only observed after the annealing temperature is higher than 800 °C.

6.2 Experimental

As described in Chapter 3, the InGaAsN/GaAs QD samples used in this study were grown on the SI-GaAs (100) substrate. First, a 500 nm GaAs buffer was deposited at 600 °C. The temperature was then lowered to 550 °C prior to the growth of a 12 monolayers (MLs) thick InGaAsN QDs. The nominal In and N mole fractions for the QDs are 40% and 3%, respectively. Immediately after the QD layer, the temperature was ramped back to 600 °C whilst depositing a 200 nm GaAs barrier/capping layer. The whole structure was nominally undoped and grown at 76 Torr. The as-grown wafer was then cleaved into small pieces and deposited with different dielectric films. One set of samples were deposited with TiO_2 by electron-beam evaporation. The second set of samples were deposited with SiO_2 by plasma enhanced chemical vapour deposition at RT using N_2O/SiH_4. One half of each SiO_2 capped sample was then deposited with a 180 nm thick TiO_2 film to form a bilayer cap. The thickness was 190 nm for SiO_2 layers and varied from 60 to 600 nm for TiO_2 layers, as measured by α-step profiler. These samples including the reference (as-grown) sample were then cleaved into smaller pieces and subjected to RTA for 30 s at various temperatures under N_2 flow. During RTA, the samples were sandwiched between two pieces of fresh GaAs

wafers to minimise the preferential loss of arsenic from the surface. To minimise the effects of compositional fluctuations, photoluminescence (PL) of each sample was first measured prior to annealing to confirm all samples have the same composition. PL measurements were performed at both room temperature (RT) and low temperature (77 K).

6.3 Results and discussion

6.3.1 Effect of the TiO_2 film

Figure 6-2 shows the low-temperature (77 K) PL spectra of two annealed (750°C for 30s) InGaAsN QD samples capped with TiO_2 films of different thicknesses. The spectra of the sample annealed without cap and the as-grown sample are also shown for reference. After RTA at 750 °C for 30 s, a significant blueshift of the PL peak was observed for the reference sample [curve (d) in Fig. 6-2]. It was accompanied by a narrowing in spectral linewidth and an improvement in PL intensity, similar to observations in the InGaAs/GaAs QD structures[8,9]. There have been many investigations on the effect of thermal annealing on PL properties of the InGaAsN/GaAs QW structures. Improvement of the PL intensity, blueshift of the PL peak wavelength and narrowing of the spectral linewidth after RTA have been reported in these studies.[10-12] These effects have been generally attributed to the reduction of the number of non-radiative recombination centres, the interdiffusion of the In-Ga and As-N atoms across the QW-barrier interface, and the compositional homogenisation, respectively.[10-12] It is well known that in the quantum confined heterostructures, the interdiffusion process is mainly promoted by the diffusion of point defects, such as vacancies and interstitials.[2,7] Since low growth temperature is required to incorporate sufficient N into InGaAs to obtain 1.3 μm or longer PL emission without phase separation,[13] it is expected that there are more grown-in defects incorporated in the InGaAsN layer and its vicinity during growth than in other III-V materials grown at higher temperatures. In addition, due to the larger strain and interfacial area in the QD structure than in the QW structure, more defects could form at the interface between QDs and the surrounding barriers,[14,15] leading to enhanced interdiffusion. Hence, a very large energy shift was observed in the reference InGaAsN/GaAs QD structure after annealing. Moreover, the

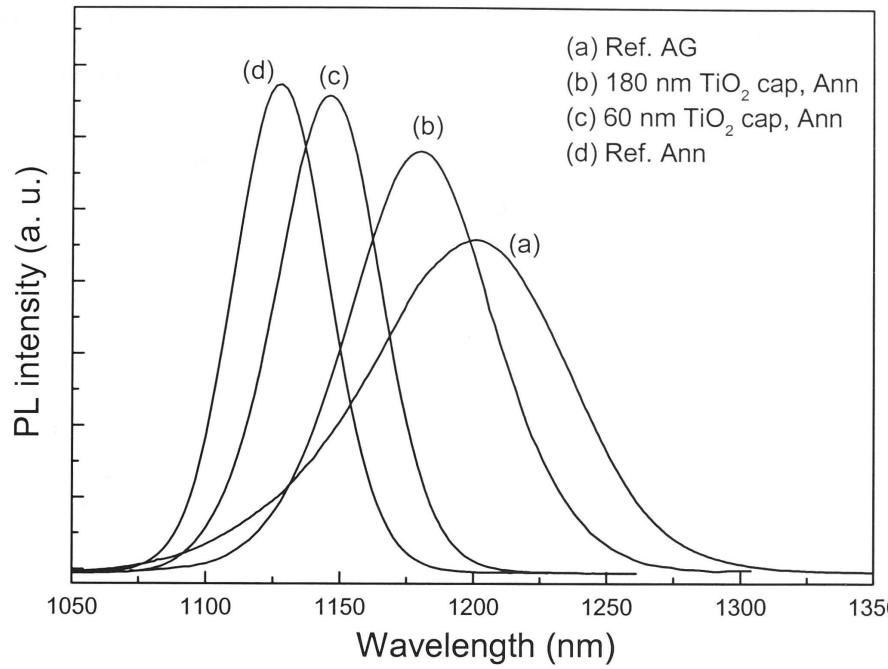

Fig. 6-2 Low temperature (77 K) PL spectra of a reference and two TiO_2-capped InGaAsN QD samples annealed (Ann) at 750 °C for 30 s. A PL spectrum from a reference as-grown (AG) sample is also included.

broad PL emission from the as-grown QD sample reflects the QD size distribution and the composition fluctuation. In addition to the possible inhomogeneous distribution of In and Ga, since N has a very small atomic size and a very large electronegativity compared with As, it could easily lead to more local strain and composition fluctuation during growth. Annealing leads to the removal of these local strain/compositional variation via interdiffusion and hence a more 'uniform' QD distribution, resulting in a narrowing of PL linewidth. Moreover, a shallower confining potential caused by the interdiffusion also leads to a smaller variation in emission from dots of different sizes.[8,16]

However, when a layer of TiO_2 was deposited on the sample's surface, the blueshift of the PL peak was much suppressed after annealing [curves (b) and (c) in Fig. 6-2]. The thicker the layer is, the more effective it is in suppressing the blueshift of the PL spectrum. The PL intensity of the sample annealed with TiO_2 cap increased and the PL linewidth decreased compared with those of the as-grown sample, respectively,

suggesting that there was no defect injection into the QD from the TiO_2/semiconductor interface. The mechanism of this suppression of PL blueshift is proposed to be the tensile stress field exerted on the semiconductor (GaAs) by the TiO_2 layer during annealing due to the larger thermal expansion coefficient of TiO_2, as shown in table 6.1. For a thin homogeneous film (e.g., TiO_2) deposited on a thick substrate (e.g., GaAs), the thermal stress generated by the thin film can be expressed as:

$$\sigma_{th} = \left(\frac{E_f}{1-\nu_f}\right) \cdot \Delta\alpha \cdot \Delta T \tag{6.1}$$

where E_f and ν_f are, respectively, Young's modulus and Poisson coefficient of the thin film, $\Delta\alpha$ is the mismatch of the linear thermal expansion coefficient between the film and the substrate, and ΔT is the temperature variation.

Table 6.1 Thermal expansion coefficients of the different materials used in this study.

Material	α ($°C^{-1}$)
GaAs	6.8×10^{-6}
TiO_2	8.2×10^{-6}
SiO_2	0.55×10^{-6}

Unlike in the cases of SiO_2-capped GaAs-based QW structures where the compressive stress is imposed on GaAs during annealing and enhanced interdiffusion was observed,[5-7] the layer of TiO_2 exerts a tensile stress on GaAs and suppresses the atomic interdiffusion in the InGaAsN QD samples. In the case of SiO_2, the oxide layer has a strong affinity for Ga atoms and consequently, results in the outdiffusion of Ga atoms into SiO_2 during annealing, leaving behind Ga vacancies at the semiconductor surface. Under the compressive stress generated by SiO_2 during annealing, which is expected to promote the diffusion of vacancies,[5,7] these Ga vacancies then diffuse across the QW region and enhance the intermixing. However, in the case of TiO_2, even though some Ga atoms might outdiffuse into the TiO_2 layer during annealing, these Ga vacancies are trapped by the tensile strain and make little contribution to the interdiffusion process.

Furthermore, the tensile stress generated by TiO_2 can be large enough to penetrate into the QD region, which can compensate for the compressive stress experienced by the InGaAsN QDs and thus inhibits or lessen the mobility of the grown-in defects in the QDs, and suppresses the intermixing.

Fig. 6-3(a) shows the amount of blueshift at 77 K relative to the as-grown sample as a function of annealing temperature for samples capped with 60 and 600 nm thick TiO_2 films. The shifts for the reference sample (uncapped) are also shown for comparison. As expected, the amount of shift for the reference sample increased with increasing annealing temperature. After annealing at 850 °C for 30 s, the reference sample showed a very large shift of ~147 meV. However, for samples capped with the TiO_2 film, the thermal shift was reduced to 115 meV for 60 nm film and 85 meV for 600 nm film. Assuming that the 60 nm TiO_2 has the same film quality with the 600 nm TiO_2, it is expected that the thicker oxide layer imposes a stronger stress field in the QD region to suppress interdiffusion. The results in Fig. 6-3(a) further confirm that the thermal stress exerted by the oxide layer on GaAs during annealing plays an important role in the interdiffusion process. The ratio of the full width at half maximum (FWHM) of the annealed samples to the as-grown sample *vs* annealing temperature is shown in Fig. 6-3(b). For the samples capped with 60 nm TiO_2 layer, the linewidth is similar to that of the reference samples but much broader for the samples capped with 600 nm TiO_2. This is not surprising because when the interdiffusion is significantly suppressed, the 'averaging' effect of the local strain/compositional fluctuation is also reduced.

The results from thickness dependence study of the PL energy shift at 77 K are depicted in Fig. 6-4 for four annealing temperatures. Two main features can be clearly identified from this figure. The suppression of the PL energy shift was obtained in all TiO_2 capped samples in the temperature range studied here. Secondly, all curves followed the same decaying trend. When the thickness of the layer was greater than 320nm, the interdiffusion was completely suppressed during RTA up to 700°C for 30 s. However above 750 °C, it seemed that interdiffusion could not be completely suppressed even for the thickest TiO_2 layer (600 nm).

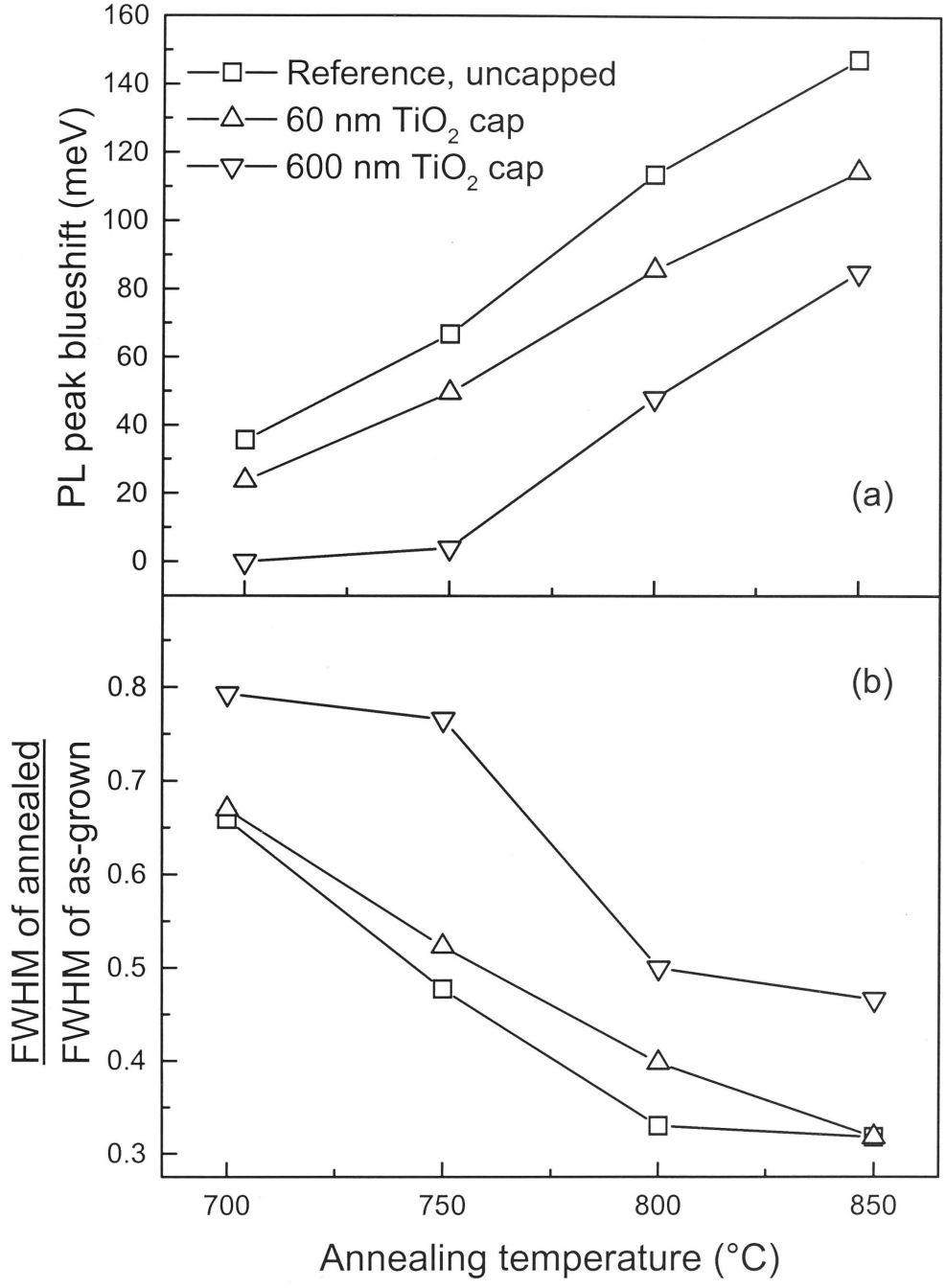

Fig. 6-3 (a) Blueshift of the PL peak energy and (b) the ratio of FWHM of PL spectra at 77 K between the annealed samples (with and without TiO_2 capping layer) and as-grown sample as a function of annealing temperature.

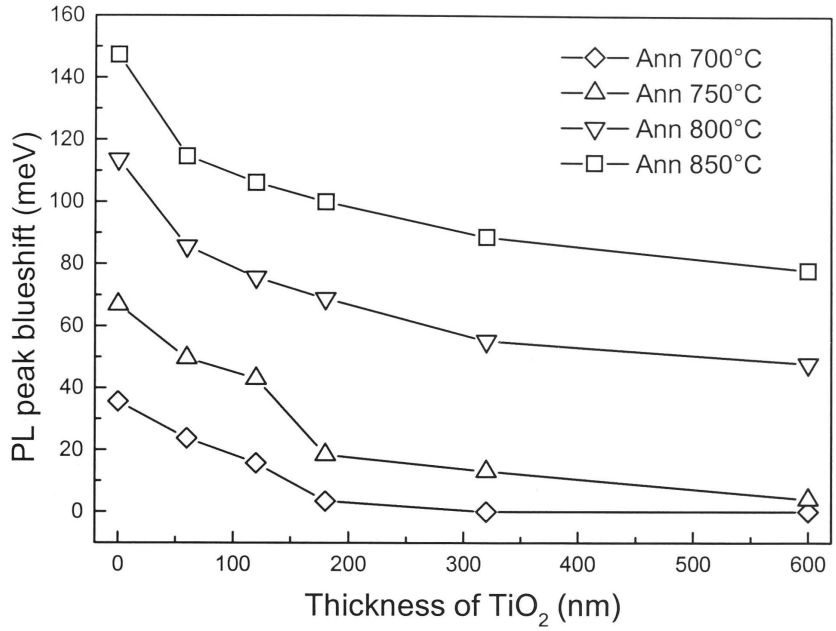

Fig. 6-4 Blueshift of the PL peak energy at 77 K between the annealed samples (with TiO_2 cap) and the as-grown sample as a function of TiO_2 thickness at various annealing temperatures.

As explained earlier, the suppression of the PL blueshift is due to the tensile stress imposed on GaAs generated by the TiO_2 film during annealing. Furthermore, this suppression effect relies on the fine balance among (a) the tensile stress imposed by the dielectric film, (b) the thermal energy of the defects, and (c) the strain gradient of the QDs. As the thickness of the TiO_2 layer is increased, the tensile stress exerted on the semiconductor is increased. Consequently the amount of interdiffusion is reduced. However, with increasing annealing temperature, not only these defects would have acquired more energy but also the strain gradient of the QDs would become more unstable to overcome the suppression effect of the TiO_2 layer. These results are promising in the sense that precise control of the amount of interdiffusion could be achieved by using the appropriate TiO_2 thickness and annealing temperature.

6.3.2 Effect of the SiO_2 film

Even though the thermal interdiffusion in the InGaAsN QD structure is already very large, it might be necessary to obtain more blueshift of the bandgap in some ap-

plications. Here we examine the ability of SiO_2 to promote the intermixing in the InGaAsN QD structure. Figure 6-5 shows the amount of blueshift of PL peak energy for the sample capped with 190 nm SiO_2 relative to the as-grown sample as a function of annealing temperature. The shifts for the reference sample (uncapped) are also shown for comparison. As expected, the SiO_2 film does promote the intermixing in the QDs when the annealing temperature is higher than 800 °C due to the Ga outdiffusion and the compressive strain enhanced diffusion of Ga vacancies.[5-7] However, at low annealing temperatures (< 800 °C), no enhancement of blueshift was observed from the SiO_2. It is assumed that at low annealing temperatures (650-800 °C), even though some Ga vacancies are created at the SiO_2/GaAs interface, they do not have enough energy to diffuse across the QD region. Thus the effect of SiO_2 films on intermixing is negligible at low annealing temperatures compared with the large thermal interdiffusion in the InGaAsN QDs.

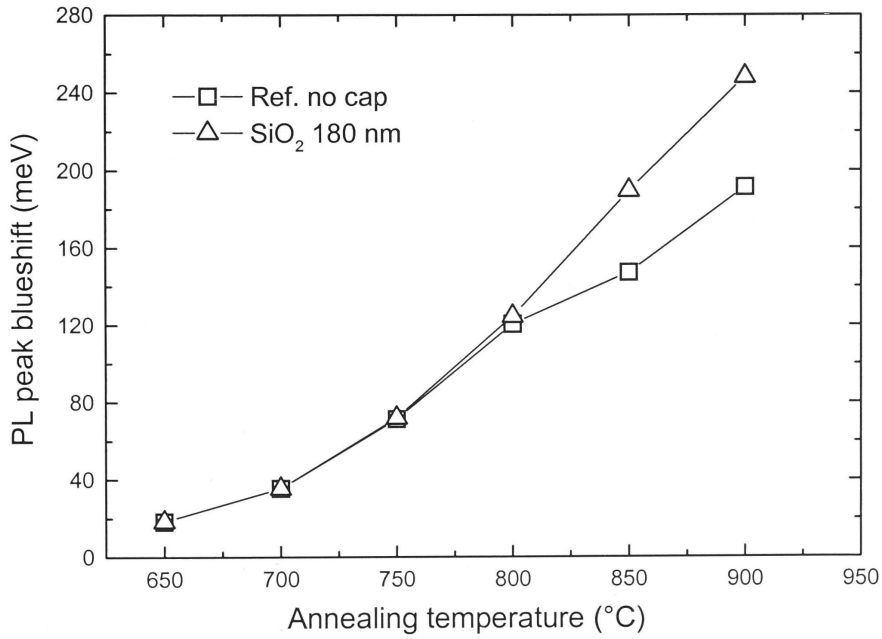

Fig. 6-5 Blueshift of the PL peak energy between the annealed samples (with and without SiO_2 cap) and the as-grown sample as a function of annealing temperature.

6.4 Conclusion

In summary, it has been shown that the thermal interdiffusion in the InGaAsN/GaAs QD structure can be suppressed controlled by deposition of a thin TiO_2 layer. The interdiffusion can also be enhanced by deposition of a thin SiO_2 layer combined with RTA at a high temperature (> 800 °C), similar to the results reported in other GaAs-based heterostructures.[5-7] The mechanism of the suppression effect from TiO_2 films on intermixing is proposed to be the tensile stress imposed by the TiO_2 layer on GaAs during annealing. By choosing a specific dielectric film followed by the proper annealing, the effective bandgap of the InGaAsN QDs could be finely tuned. This approach has a significant potential to realise the selective-area band-gap engineering for optoelectronic device integration.

References:

1 *Semiconductor Quantum Well Intermixing*, edited by E. H. Li (Gordon and Breach, Amsterdam, 2000).

2 D. G. Deppe and N. Holonyak, Jr., J. Appl. Phys. **64,** R93 (1998).

3 P. Gavrilovic, D. G. Deppe, K. Meehan, N. J. Holonyak, J. J. Coleman, and R. D. Burnham, Appl. Phys. Lett. **47,** 130 (1985).

4 L. Fu, H. H. Tan, M. B. Johnston, M. Gal, and C. Jagadish, J. Appl. Phys. **85,** 6786 (1999).

5 L. Fu, J. Wong-Leung, P. N. K. Deenapanray, H. H. Tan, C. Jagadish, B. Gong, R. N. Lamb, R. M. Cohen, W. Reichert, L. V. Dao, and M. Gal, J. Appl. Phys. **92,** 3579 (2002).

6 A. C. Bryce, F. Camacho, P. Cusumano, and J. H. Marsh, IEEE J. Sel. Top. Quantum Electron. **3,** 885 (1997).

7 A. Pépin, C. Vieu, M. Schneider, H. Launois, and Y. Nissim, J. Vac. Sci. Technol. B **15,** 142 (1997).

8 R. Leon, Y. Kim, C. Jagadish, M. Gal, J. Zou, and D. J. H. Cockayne, Appl. Phys. Lett. **69,** 1888 (1996).

9 S. Malik, C. Roberts, R. Murray, and M. Pate, Appl. Phys. Lett. **71,** 1987 (1997).

10 W. Li, J. Turpeinen, P. Melanen, P. Savolainen, P. Uusimaa, and M. Pessa, Appl. Phys. Lett. **78,** 91 (2001).

11 D. E. Mars, D. I. Babic, Y. Kaneko, Y. L. Chang, S. Subramanya, J. Kruger, P. Perlin, and E. R. Weber, J. Vac. Sci. Technol. B **17,** 1272 (1999).

12 H. P. Xin, K. L. Kavanagh, and C. W. Tu, J. Crystal Growth **208,** 145 (2000).

13 M. Kondow, K. Uomi, A. Niwa, T. Kitatani, S. Watahiki, and Y. Yazawa, Jpn. J. Appl. Phys., Part 1 **35,** 1273 (1996).

14 A. Babinski, J. Jasinski, R. Boek, A. Szepielow, and J. M. Baranowski, Appl. Phys. Lett. **79,** 2576 (2001).

15 T. Surkova, A. Patanè, L. Eaves, P. C. Main, M. Henini, A. Polimeni, A. P. Knights, and C. Jeynes, J. Appl. Phys. **89,** 6044 (2001).

16 T. M. Hsu, Y. S. Lan, W.-H. Chang, N. T. Yeh, and J.-I. Chyi, Appl. Phys. Lett. **76,** 691 (2000).

CHAPTER 7

InGaAsN quantum-dot lasers

7.1 Introduction

Long wavelength (1.3 or 1.55 μm) semiconductor laser diodes (LDs) are key devices for optical fibre communications and have attracted much attention in recent years due to their zero dispersion and minimal absorption in currently installed silica fibres. Up to now lasers at these wavelengths are almost exclusively made from InGaAsP or AlInGaAs heterostructures on InP. However, the conventional InGaAsP/InP system exhibits a relatively low characteristic temperature (T_0), which results from the relatively small conduction band offset between InGaAsP and InP: $\Delta E_c = 0.4\ \Delta E_g$. The typical T_0 value for InGaAsP/InP laser diodes is around 60 K, and only improved to 80 K by using an AlInGaAs/InP material system recently.[1] Moreover, the low refractive index contrast of InP/InGaAsP makes it almost impractical to meet the requirements for growth of distributed Bragg reflector (DBR) mirrors for vertical cavity surface emitting lasers (VCSELs), which are potentially low-cost sources for optical-fibre systems and can be directly modulated and easily coupled to fibre. For these reasons, a wide variety of research and development activities of GaAs based long-wavelength lasers have been started in last few years. Based on these research efforts, InGaAsN/GaAs system has revealed several advantages over InGaAsP/InP system: (i) For the same bandgap material, the conduction band well is deeper and the electron effective mass is larger in InGaAsN,[2-4] thus providing better confinement for electrons and better match of the valence and conduction-band densities of states. This leads to a higher T_0, higher operating temperature, higher efficiency and higher output power. For example, a high characteristic temperature of 215 K has been reported for InGaAsN/GaAs single-quantum-well LD emitting at 1.3 μm.[5] (ii) VCSELs can be straightforwardly fabricated using the well-developed GaAs/Al(Ga)As DBR mirrors and AlAs oxidation for current and optical aperture confinement technologies. (iii) InGaAsN on GaAs provides easy monolithic integration with GaAs high-speed electronics that will be essential to provide low-cost, high-speed integrated electrical drivers for direct laser modulation in high-speed networks. Recently, a variety of InGaAsN/GaAs QW based ridge-waveguide LDs[2,5-15] and VCSELs[16,17] grown by either MOCVD,[6-11,17] or MBE[2,5,12-17] have been demonstrated by different groups, showing very promising results of both low threshold current density and high characteristic temperature.[5,8-10,14] In particular, Tansu *et al*[9] reported that the cw lasing threshold current densities of MOCVD grown

InGaAsN laser devices (L_{cav} = 2000 μm, with HR/AR coating) are 200 and 615 A/cm^2, at temperatures of 20 and 100 °C, respectively. This result represents the lowest threshold current density for 1.3 μm QW lasers under cw operation at temperatures up to 100 °C, in comparison with reported results of the conventional InGaAsP and AlInGaAs 1.3 μm QW lasers.

However, the lasing wavelength of most of these QW based lasers has been limited to around 1.3 μm, due to the difficulty in growth of high-quality InGaAsN/GaAs QW structures with high composition of In or N. Even though much effort has been made to extend the wavelength of InGaAsN/GaAs based QW lasers above 1.3 μm, the threshold current density was found to be drastically increased to values around 2 kA/cm^2 at 1.4 μm[11,15] or above 10 kA/cm^2 with a decrease of the external efficiency to 0.1 W/A at 1.5 μm[12], which makes these devices impractical. It is well known that quantum-dot (QD) lasers were anticipated to have many advantages, such as largely extended emission wavelength, decreased transparency current density, increased material and differential gain, and a large characteristic temperature, T_0.[18,19] Some of these predictions have been verified today on the In(Ga)As QD devices, such as long-wavelength (~1.3 μm) emission,[20,21] low threshold,[22] high differential gain,[23] and high T_0.[24] Therefore, an alternative approach to extend the wavelength and improve the performance of laser devices based on the InGaAsN active region is to use the self-assembled InGaAsN-QD structure. Compared to the large amounts of studies on InGaAsN/GaAs QW lasers, there have been relatively few reports on the InGaAsN/GaAs QD laser structures.[25] Recent reports have shown the operational InGaAsN QD laser devices[25] and the photoluminescence (PL) emission at the 1.5 μm range from the InGaAsN QDs,[26,27] indicating that the InGaAsN QDs are very promising for long-wavelength laser devices.

In this chapter, a *p-i-n* InGaAsN QD-based graded-index separate-confinement heterostructure (GRINSCH) was designed and fabricated into the ridge waveguide laser devices. The detailed description of GRINSCH lasers is beyond the scope of this thesis and can be found in several textbooks.[28-30] The final devices were characterised using absorption and electroluminescence spectra, and light output power *versus* injection current (*L-I*) measurements. These experiments provide several key parameters of the devices, such as threshold current density, modal absorption, external quantum efficiency, and internal quantum efficiency.

7.2 Structure design and experimental

The structure of the InGaAsN QD laser structure is listed in table 7.1. To minimise the threshold current density for the InGaAsN QD laser, a small spot size laser structure was used with d/Γ = 0.3 μm (where d is the thickness of the active layer, Γ is the confinement factor). In addition, to reduce the blueshift of the emission wavelength due to the intermixing in the QDs during growth of the top AlGaAs cladding layer, a thin p-cladding layer consisting of a 0.45 μm thick $Al_{0.40}Ga_{0.60}As$ layer was adopted. The relatively low Al content (40%) in the p-cladding layer also allows for lower growth temperature to minimise the thermal interdiffusion in QDs. The whole laser structure was grown by two separate MOCVD reactors at 76 Torr in three steps to avoid the memory effect of Al precursor. Any residual Al precursor in the reactor

Table 7.1 Thin p-clad InGaAsN quantum dot laser structure.

Layer type	Al composition index	Thickness (nm)	Doping (cm^{-3})	
p^{++} GaAs	0.00	100	C: >5 × 10^{18}	Part-III
p $Al_xGa_{1-x}As$	0.40	450	C: 5 × 10^{17}	
Grading $Al_xGa_{1-x}As$	0.30→0.00	150	undoped	
GaAs	0.00	20	undoped	
GaAs	0.00	30	undoped	Part-II
InGaAsN QD	0.00	3.5	undoped	
GaAs	0.00	20	undoped	
GaAs	0.00	30	undoped	Part-I
Grading $Al_xGa_{1-x}As$	0.00→0.30	150	undoped	
n $Al_xGa_{1-x}As$	0.30	250	Si: 4 × 10^{17}	
n $Al_xGa_{1-x}As$	0.37	400	Si: 4 × 10^{17}	
n $Al_xGa_{1-x}As$	0.40	1800	Si: 1 × 10^{18}	
n^+ GaAs buffer	0.00	500	Si: 1 × 10^{18}	
n^+ GaAs substrate	0.00			

could cause the direct chemical reaction between Al and N, resulting in poor quality InGaAsN QDs. Therefore, the active region (part-II) consisting of layers without Al was grown in a modified Thomson-Swan reactor. The Al-containing cladding layers, part-I and part-III, were grown in an AIXTRON reactor. In the first growth step (part-I), the growth temperature was maintained at 750 °C. In the second growth step (part-II), GaAs was grown firstly at 600 °C. The wafer was then cooled down to 550 °C to commence the growth of InGaAsN QDs, in which the nominal In content and N content are 40% and 3%, respectively. As described in Chapter 3, the lateral size and the density of these dots are about 35 nm and 5 x 10^{10} cm^{-2}, respectively. The growth temperature was then ramped back to 600 °C during the growth of the capping GaAs layer to finish the second growth step. In the third growth step (part-III), the structure was grown at 650 °C to minimise the thermal interdiffusion in the QD active layer. The *p*-type doping and *n*-type doping were obtained by using carbon and silicon, respectively. In addition to the InGaAsN QD laser structure, an InGaAs QW laser structure was also grown as a reference in the same steps except for switching off the N precursor.

The structure mentioned above is essentially a *p-i-n* structure, where the active region is in the middle of the undoped region. After growth, the as-grown wafers were then processed into the ridge waveguide laser devices, as described in Chapter 2 (section 2.4.10). When the device is reverse biased, it can be used to measure the photocurrent generated by a spectrally resolved light, as described in Chapter 2 (section 2.4.4). This configuration takes advantage of the small internal loss in the carefully designed vertical and lateral waveguides existing in the device, thus allowing the spectrally resolved input light to travel along the device length of 0.5 - 3 mm with very small attenuation during the photocurrent measurements. This allows for the QD contribution to be clearly observed in the photocurrent spectra and distinguished from the wetting layer, in spite of the small value of the absorption coefficient in the QD sheet. In addition, it allows for the separate measurements of the contribution of the in-plane transverse-electric (TE) polarisation and the transverse-magnetic (TM) polarisation, along the growth direction. In this way, information about the contribution of transitions from the heavy hole states and the light hole states can be obtained from the photocurrent spectrum.

In addition to the photocurrent measurements, the light absorption behaviour of the laser device was also measured using a multisection-device technique. The light output power *versus* current (*L-I*) characteristics of the laser devices were measured using a calibrated optical multimeter. The electroluminescence and lasing spectra were also collected as described in Chapter 2.

7.3 Results and discussions

In general, the lasing and spontaneous emission spectra of the QD LDs are generally significantly broader than for similar QW devices, due to the inhomogeneous spectral broadening caused by the Gaussian dot size distribution, which generates an average ground state (excited) energy with a certain standard deviation, depending on the uniformity of dot size in the self assembled layer and thus upon growth conditions. In addition to this effect, when the thermal equilibrium between the carriers in different dots in the lateral direction cannot be generally assumed, especially at low temperatures and for the high dot confinement energy, carriers localised in different dots cannot escape fast enough to allow for a description by a global Fermi-function, resulting in an even broader spectrum.[31,32] With these fundamental issues in mind, the results and discussions are presented in the following sections.

7.3.1 Photocurrent measurements

Photocurrent at 0 V bias

The photocurrent spectra taken at 0 V external bias gives insight into the transition strength of the quantum dots relative to the wetting layer, the In composition of the wetting layer and the contribution of heavy hole/light hole to the transition. Figures 7-1(a) - (c) show such spectra measured at room temperature (RT) with polarised (TE or TM) light and without polarisation (total) for both the InGaAsN QD and the InGaAs QW laser LDs. The common transitions in the wavelength range of 700- 870 nm in these spectra belong to either the GaAs barriers or to the graded $Al_xGa_{1-x}As$ surrounding the active region, and are not of interest. In addition to these common features, there is an obvious difference between the QD [Fig. 7-1(a)] and the QW structures [Fig. 7-1(b)]. The QD structure exhibits a low energy signal around 1170 nm

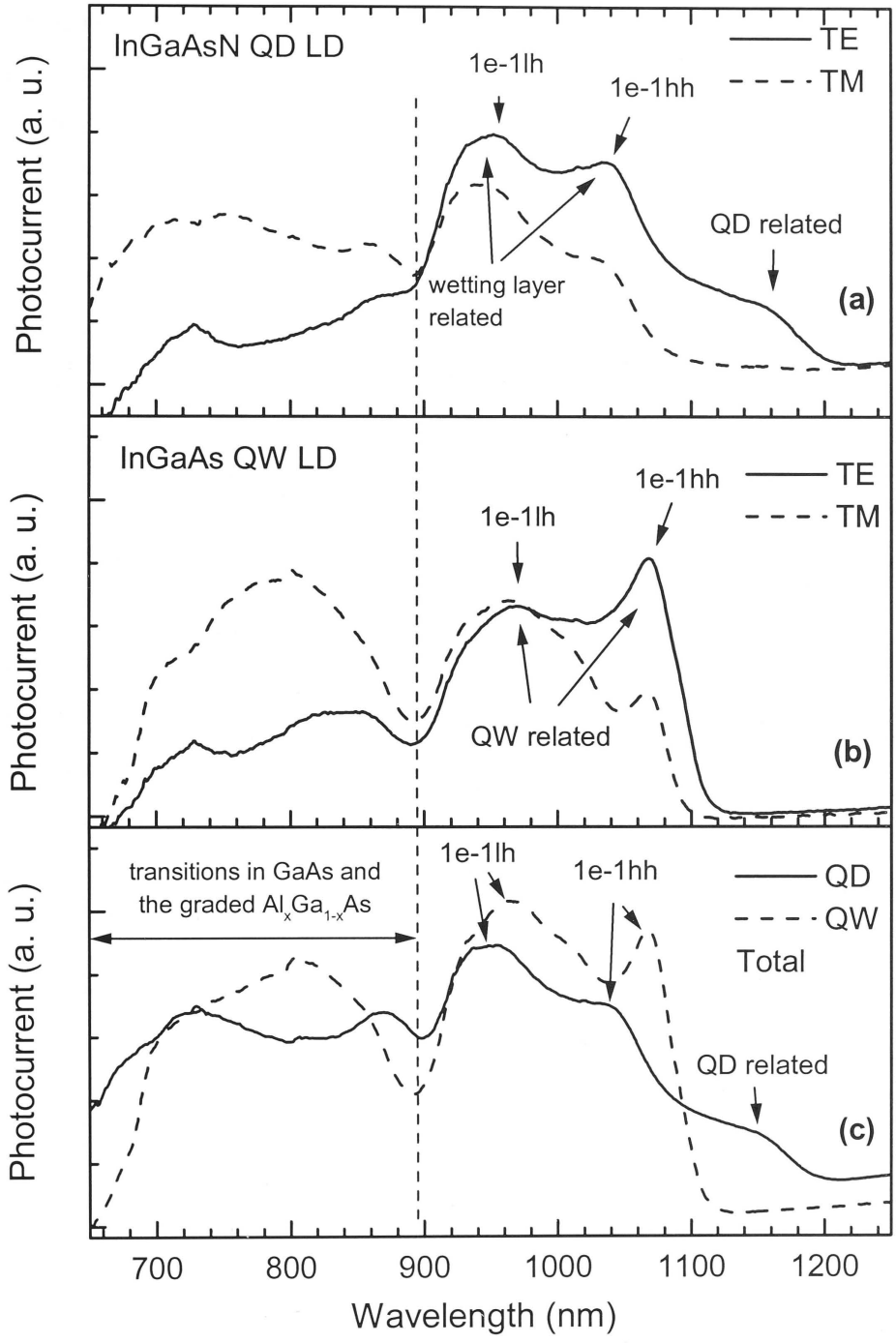

Fig. 7-1 Photocurrent spectra of (a) the InGaAsN QD LD with TE/TM light, (b) the InGaAs QW LD with TE/TM light, and (c) the InGaAsN QD and the InGaAs QW LDs without polarisation measured at RT with 0 V external bias. Both devices have a stripe width of 4 μm and a cavity length of about 1 mm.

which is not seen in QW structure and is believed to be related to transitions in the dots. This signal is more clearly seen in Fig. 7-1(c), it is lower in intensity and broader than the QW peaks due to the smaller volume occupied by the QDs relative to the QW. The dot transitions are clearly TE-polarised, which means that these transitions are mainly due to emissions from the electronic levels to the heavy hole states. Similarly, emissions from the electronic levels to the heavy hole (hh) states and to the light hole (lh) states in the wetting layer of the InGaAsN QD structure [Fig. 7-1(a)] or in the InGaAs QW structure [Fig. 7-1(b)] can be easily distinguished by comparing the TE mode and the TM mode photocurrent spectra. These transitions such as 1e–1hh and 1e–1lh are indicated in Fig. 7-1(a) - (c).

It can also be seen that the energies of electron-hole (both heavy and light hole states) transitions in the wetting layer of the InGaAsN QD structure are at higher energies than those in InGaAs QW structure, indicating a lower In content in the wetting layer of the QD structure than in the InGaAs QW structure, presumably due to the In outdiffusion from the wetting layer into the QDs. Apart from the blueshift of the QW peaks as a whole, the fact that the photocurrent peaks are broader for the QD structure also confirms a rougher interface between the wetting layer and the GaAs barriers, due to the QD formation.

Bias and temperature dependence of the photocurrent

Even if the externally applied bias is 0 V, the electric field inside the *p-i-n* structure is nonzero. The internal electric field is well approximated by:

$$E = (V + V_i) / d_{undoped} \tag{7.1}$$

where V_i is the built-in potential in the p-n junction, taken to be –1.8 V, corresponding to 30 % Al in the *p* and *n* doped $Al_{0.30}Ga_{0.70}As$ confinement layers; $d_{undoped}$ is 0.4 μm, corresponding to the thickness of the undoped waveguide layers; and V is the externally applied bias. The advantage of using a *p-i-n* structure is that it provides a very low dark current, but the disadvantage is that it does not allow the measurement of spectrum under positive internal field, thus limiting the range of fields available for characterisation in the range of –200 to 0 kV/cm, corresponding to the externally applied bias of –6 to +1.8 V.

Figures 7-2(a)-(c) show the photocurrent spectra at different biases (without polarisation) of the InGaAsN QD LD measured at 77 K and RT, and of the InGaAs QW LD measured at RT, respectively. At RT, the thermal escape rate is high enough to allow the QD transitions to be visible in the photocurrent spectra without external applied bias [Fig. 7-2(b)]. However, at low temperature the predominant escape mechanism of the photoexcited carriers from the QD levels is tunnelling,[33] which is much less efficient than the thermal escape at RT and could only be significantly enhanced by the applied electric field. Thus, at 77 K, without external bias, not only the quantum-dot peaks are absent from the spectrum, but also the peak corresponding to the 1e-1hh transition in the wetting layer [Fig. 7-2(a)]. These peaks start to appear in the spectra after external bias is applied, starting with the higher energy transitions, which have a higher tunnelling rate under applied bias.

At RT, for a small internal field (without external bias), the photoexcited carriers are mainly captured in the active region and recombine radiatively before being swept away by the internal electric field towards the n^{++} and p^{++} highly doped layers to become observable as photocurrent. For a certain applied bias (about -2 to -3 V), the photocurrent saturates, corresponding to the regime where almost all photo-generated carriers are swept away by the internal electric field before being captured by the active region. In this regime, the relative differences between the photocurrent intensities at different wavelengths reflect differences in the absorption strength of different transitions. It is interesting to notice in Figure 7-2(b) that, even though different wavelengths in the range 700-1200 nm correspond to transitions occurring in different regions of the device, i.e. GaAs barrier layers, graded waveguide layers, the wetting layer, and the QD layer, they all saturate at the same bias. That means that the photo-generated electrons, before being swept away by the electric field, they relax very fast to the same level, presumably the ground state of the quantum dots. This observation is in agreement with Ref. 34, where the photocurrent spectra from the ground states and the excited dot states show the same temperature and bias dependency, thus leading to the conclusion that the relaxation rates from the excited states to the ground state are faster than any competing thermal or tunnelling escape rates. This is good news for a LD device, for which a fast relaxation rate to the ground states is an important ingredient for good device performance.

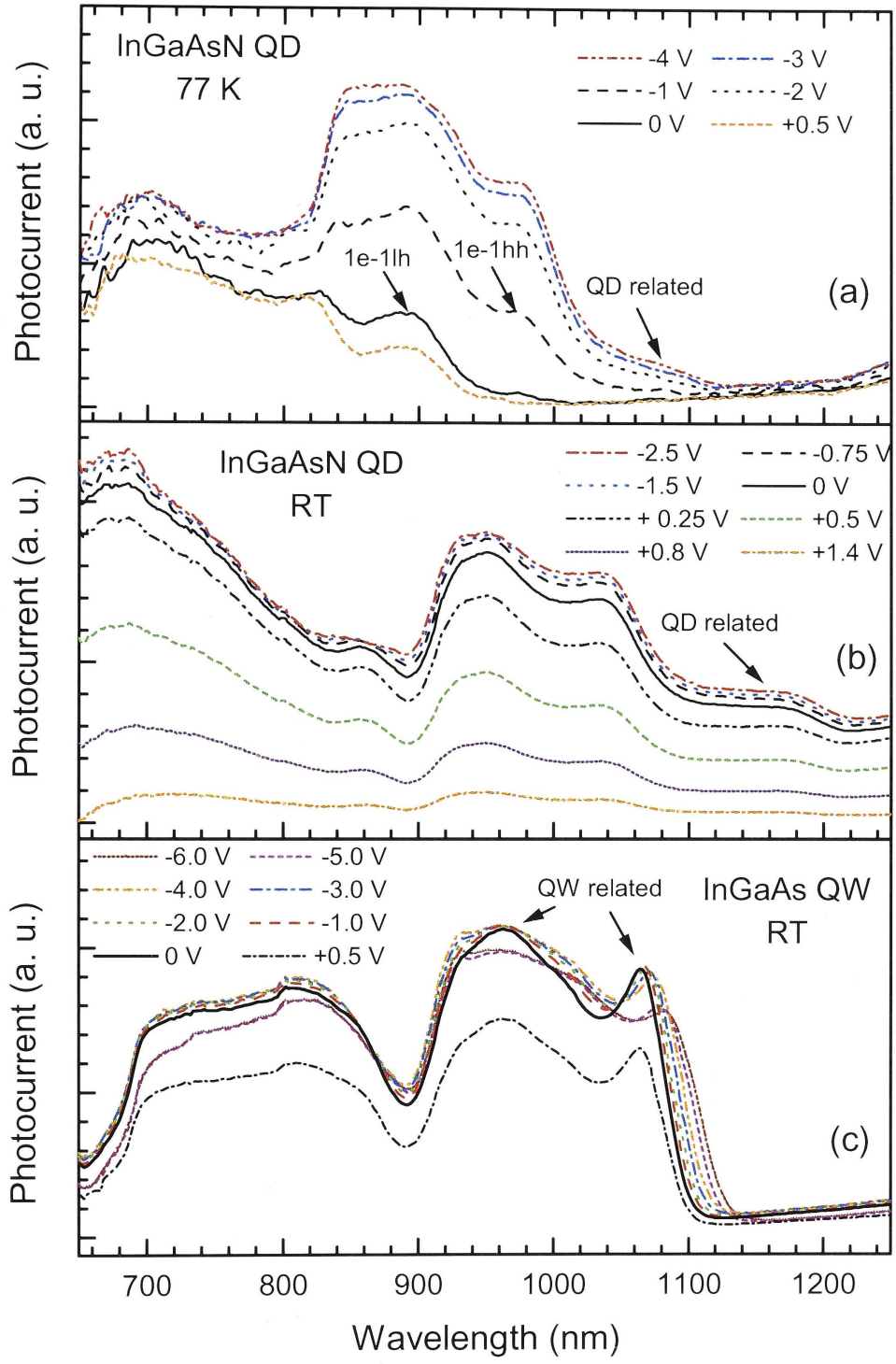

Fig. 7-2 Photocurrent spectra (without polarisation) of the InGaAsN QD LD measured at (a) 77 K, (b) RT, and (c) of the InGaAs QW LD measured at RT.

Quantum-confined Stark shift in photocurrent spectra of the QD and the QW structures

Applying an electric field along the growth direction in a QW *p-i-n* structure has two main effects: first, the transition energy shifts towards lower energy quadratically with the applied field (so called quantum-confined Stark shift[35-37]). The magnitude of this shift strongly depends on the potential depth, the effect being stronger for deeper confining potential wells. Second, the electric field induces a spatial shift of the electron and hole wave function in opposite directions, decreasing their spatial overlap and thus the oscillator strength of the transitions.[37] These effects are symmetric for the positive and negative electric fields in a QW structure with uniform composition, reflecting the symmetry along the growth direction. Thus based on the Stark shift, any asymmetry in a QW/QD structure due to the composition enrichment, e.g., In enrichment on the top of the InGaAs QDs,[38] or due to the strain caused by the pyramidal shape of the QDs, will be reflected by the asymmetric Stark shift for positive and negative electric fields.

The question of a built-in electric field in a QD structure is crucial for the device performance. Especially for the MOCVD grown QD LDs, it was shown that the gain of the ground state can be very small and the lasing occurs only from the excited states due to the depletion of the ground-state transition by the internal fields (piezoelectric, dipole, and junction fields).[39] Eventually, these electric fields will be screened by the injected carriers under forward bias but when this happens, the ground state is already occupied and the lasing would occur only from an excited state in the dots.[39] Since the built-in electric field seems to be highly dependent on growth conditions and can have profound effects on device performance, both as a laser and a modulator, it is worth investigating it further. It was also recently shown that, contrary to the case of a QW, in a highly pyramidal QD the Stark shift cannot be described by a unique quadratic function of the applied electric field for both positive and negative values of this field.[40] This is because the confining potential for holes in the vertical direction cannot be approximated by a simple gradient corresponding to a constant built-in electric field. However, this approximation may still be acceptable for very truncated pyramidal dot shapes.

The Stark shifts of the InGaAsN QD and the reference InGaAs QW LDs at RT obtained from Fig. 7-2(b) and (c) as a function of electric field E are shown in Fig. 7-3(a) and 7-3(b), respectively. As observed from Fig. 7-3, the Stark shift of the InGaAsN QD

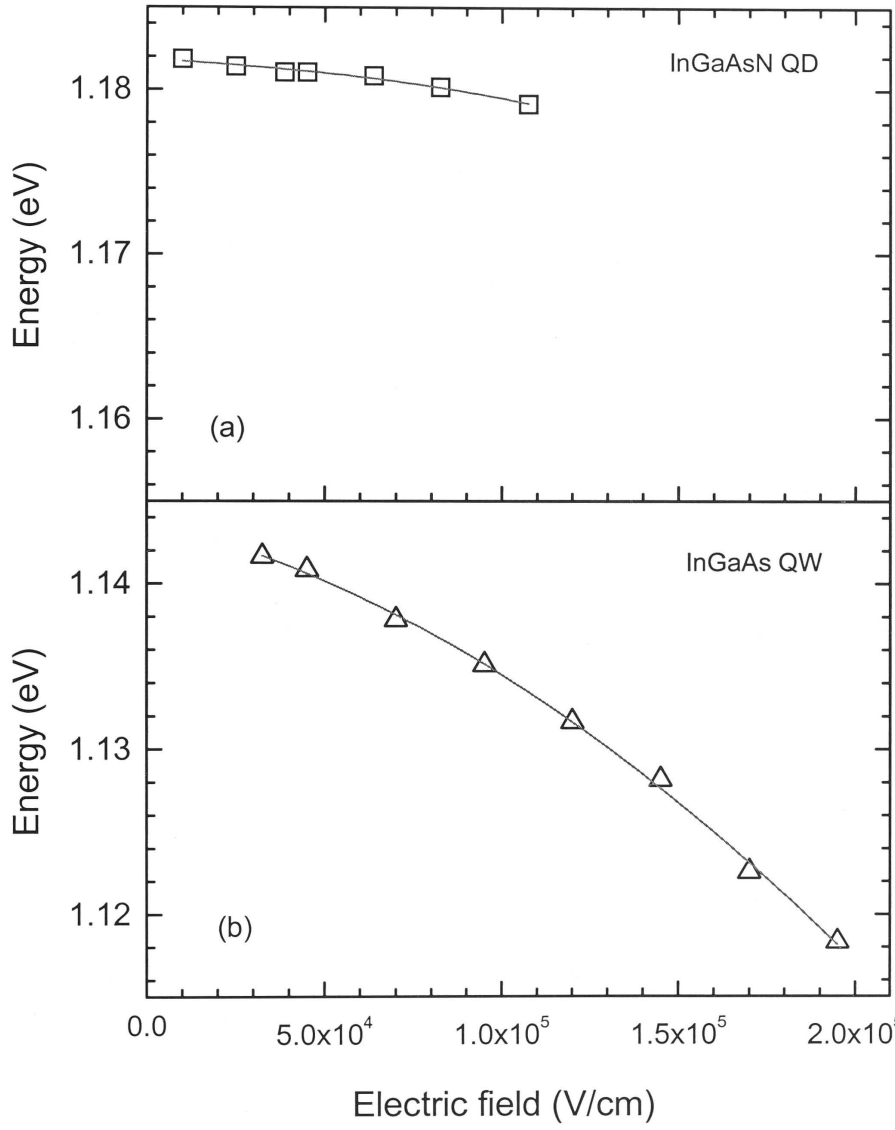

Fig. 7-3 Stark shift as a function of the electric field: (a) InGaAsN QD LD, and (b) reference InGaAs QW LDs. The solid lines are quadratic function fits.

LD (about 2.3 meV from 10 to 100 kV/cm) is much smaller than that of the InGaAs QW LD (about 7.4 meV from 32 to 100 kV/cm) due to the increase of the electron-heavy hole displacement, which is consistent with many other publications.[38,41,42] However, the Stark shift of the InGaAsN QD structure [Fig. 7-3(a)] can be fitted with a single quadratic function and does not show an average built-in internal electric field which is often observed in many In(Ga)As QD structures.[38,41,43] This indicates that the internal field in InGaAsN QDs is much less than that in the typical In(Ga)As QD structure, might be due to the reduction of strain in the QDs caused by N incorporation.

7.3.2 Absorption spectra

Figures 7-4(a) and 7-4(b) show the typical absorption spectra measured by the multisection-device technique (solid lines, called absorption spectrum hereafter) and the photocurrent at 0 V external bias (dashed lines, called photocurrent spectrum hereafter) for the InGaAsN QD and the InGaAs QW structures, respectively. The absolute values of the absorption coefficient are only valid for the absorption spectra. The photocurrent spectra only have arbitrary values and were normalised for comparison with the absorption spectra. It is worth mentioning here that in the photocurrent measurements, the light from the tungsten-filament lamp has to pass through the monochromator and the optical system, and has consequently been significantly attenuated by the time it reaches the device. However, by using a multisection device, the spontaneous light generated in the second section is efficiently guided in the first section by the lateral and the vertical waveguide without significant loss. Therefore, the excitation intensity for the target QD structure is much higher in the multisection device than in the photocurrent measurements.

It can be clearly seen that the shapes of the absorption spectra measured by these two methods are different for the InGaAsN QD sample [Fig. 7-4(a)], but are very much similar for the InGaAs QW sample [Fig. 7-4(b)]. For the QW sample, a small red shift of the absorption spectrum measured using the multisection device with respect to the photocurrent spectrum was observed mainly due to the bandgap narrowing caused by the heating of the device and the higher concentration of photoexcited carriers. For the QD sample, however, such a red shift was not observed. Instead, a clear enhancement

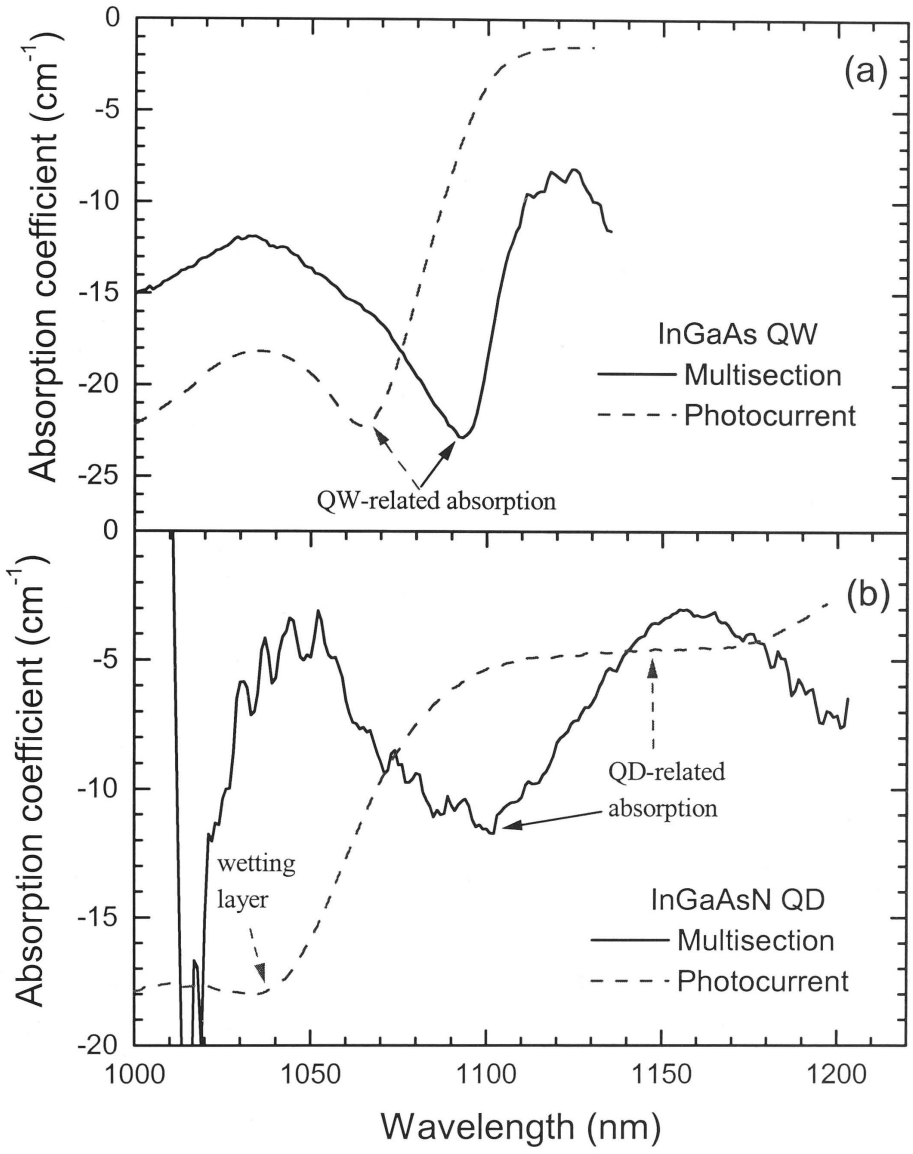

Fig. 7-4 Absorption spectra measured by the multisection-device technique (solid lines) and the photocurrent at 0 V external bias (dashed lines) for (a) reference InGaAs QW structure, and (b) InGaAsN QD structure, respectively. The absorptions peaks related to different layers are shown by arrows.

of the QD excited-state absorption was observed when measured using the multisection device compared with the relatively flat absorption in the photocurrent spectrum.

Although not observed in exactly the same way in our samples, a broad background photocurrent from a InAs/GaAs QD structure was reported in Ref. 34. A high continuum background was also observed by Vasanelli *et al*[44] in the photocurrent spectrum from the InAs/GaAs QD structure and was attributed to the cross transitions between the discrete dot levels and the unlocalised states in the wetting or barrier layers.[44] It is important to note that this absorption continuum background was not observed in emission mode, either electroluminescence or photoluminescence,[34] suggesting that carriers in these states have a low radiative efficiency.

Such a clear continuous background on which the ground and excited QD states are superposed was not observed in the experiments here. Instead, the photocurrent spectra reveal an almost flat absorption until a continuous background merges with the absorption spectrum of the wetting layer. In the absorption spectrum measured under the incident light with a larger excitation density (using the multisection device), however, the relative amplitude of the excited states increases compared with the absorption of both the background and ground states. It is proposed that under the excitation of the light generated in the second section of the multisection device, the photoexcited carriers created in the first section modify the potential profile in the QDs such that the oscillator strength of the excited-state transitions increases compared with the ground-state transitions in the absorption spectrum. This could also explain the fact that the LD devices lase from the excited states and not from the ground state (results are discussed later).

7.3.3 Electroluminescence and lasing spectra

Figures 7-5(a), (b), and (c) show typical electroluminescence (EL) spectra under the pulsed operation (with a pulse width of 2 μs and a repetition rate of 28 kHz) for the InGaAsN QD LDs measured at 77 K and RT, and a reference InGaAs QW LD measured at RT, respectively. For comparison, the photocurrent spectra measured at the corresponding temperatures are also shown in the same figures. All devices used here are as cleaved with a cavity length of about 0.8 mm and a stripe width of 4 μm. It is clearly seen that for the InGaAsN QD LD, lasing occurs at about 45 mA at 77 K and

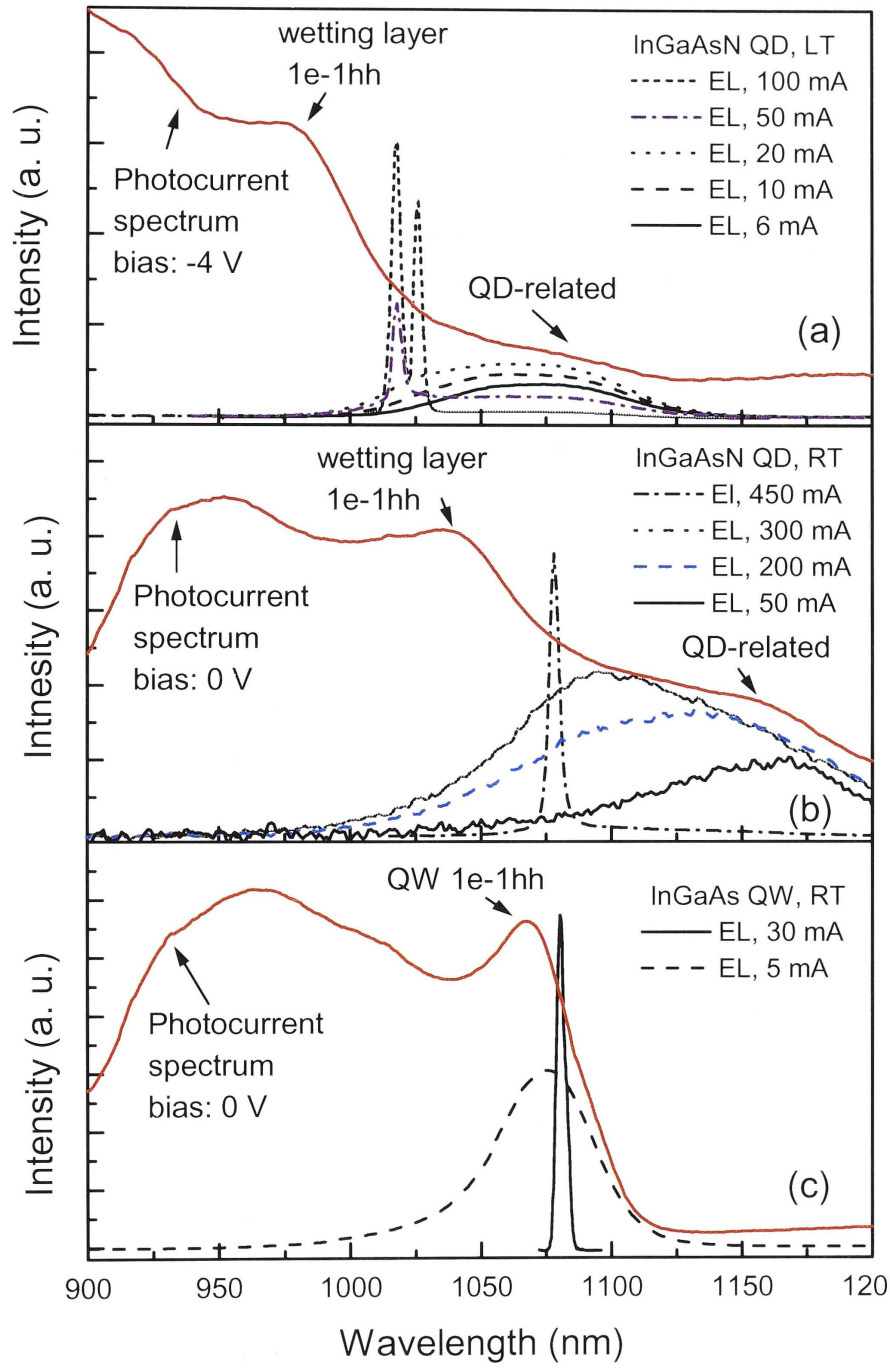

Fig. 7-5 Electroluminescence (EL) spectra at different injecting current for (a) an InGaAsN QD LD at 77 K, (b) an InGaAsN QD LD at RT, and (c) a reference InGaAs QW LD at RT. The photocurrent spectra are also shown for comparison and are shifted vertically for clarity.

about 450 mA at RT. At very low current injection levels, such as 6 mA at 77 K and 50 mA at RT, the maximum of the spontaneous emission is at about 1082 nm at 77 K and about 1168 nm at RT. However, the emission wavelength shifts to 1018 nm at 77 K and 1078 nm at RT when lasing takes place. This behaviour is typical for a QD active region that provides enough gain for lasing only after the excited states occupation rate becomes important, due to the limited volume of the QDs.[45,46] Nevertheless, the devices are lasing from the QD transition, as evidenced by the comparison between the lasing spectrum and the photocurrent spectra in Fig. 7-5(a) and (b), even though this transition is probably from an excited state, possibly involving one bound QD state and one delocalised state in the InGaAsN wetting layer. In contrast, the InGaAs QW LD does not show a similar behaviour and the lasing occurs at a current injection of about 30 mA at RT with a wavelength of 1080 nm. The small red shift of the lasing spectrum with respect to the photocurrent and low-injection EL spectra is mainly due to the heating and the band-gap narrowing due to the high concentration of carrier injection.

7.3.4 Characterisation of the laser device

All the laser devices tested here were cleaved from the wafer without any coating. The stripe width is 4 μm for all the InGaAsN QD LDs, and 4 μm or 50 μm for the InGaAs QW LDs. The *L-I* characteristics of the InGaAsN QD and the InGaAs QW LDs were tested in pulsed condition with a pulse width of 2 μs and a repetition rate of 28 kHz. The typical *L-I* curves of an InGaAsN QD LD with a cavity length L = 0.42 mm and an InGaAs QW LD with L = 1.5 mm measured at RT are shown in Fig. 7-6. From the *L-I* curves, the threshold current density J_{th} (as shown in Fig. 7-7) of the laser devices was calculated by dividing the threshold current by the stripe width and the cavity length L. The external differential quantum efficiency η_d can also be extracted from the slope of the *L-I* curves. Theoretically, $1/\eta_d$ can be described by the expression:

$$\frac{1}{\eta_d} = \frac{1}{\eta_i}\left[1 + \frac{\alpha_i L}{\ln(1/R)}\right] \tag{7.2}$$

where η_i is the internal quantum efficiency, α_i is the internal loss, and R is the facet reflectivity. From this equation, using a value of R = 33% which is the typical value for

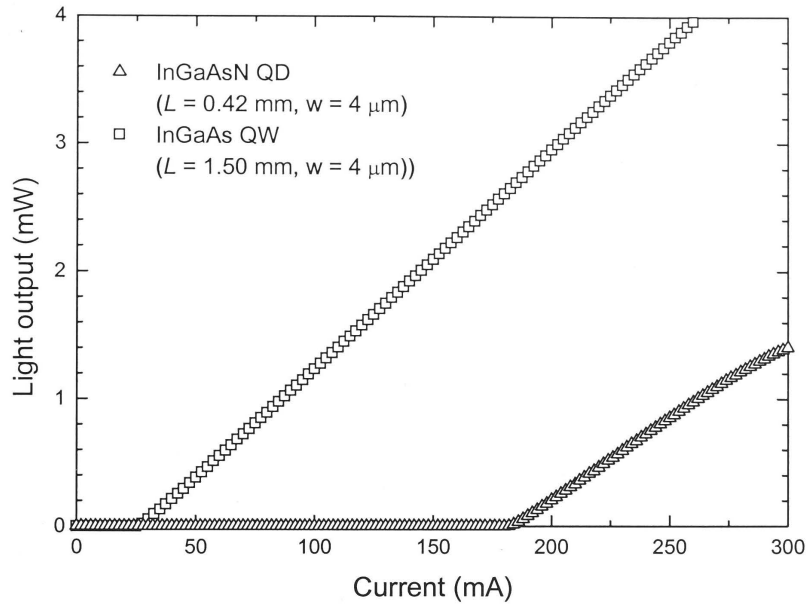

Fig. 7-6 RT *L-I* curves of an InGaAsN QD LD (triangle) and a reference InGaAs QW LD (square) under pulsed operation (2 μs pulse width, 28 kHz repetition rate). The cavity length (L) and ridge width (w) are also shown in the legend.

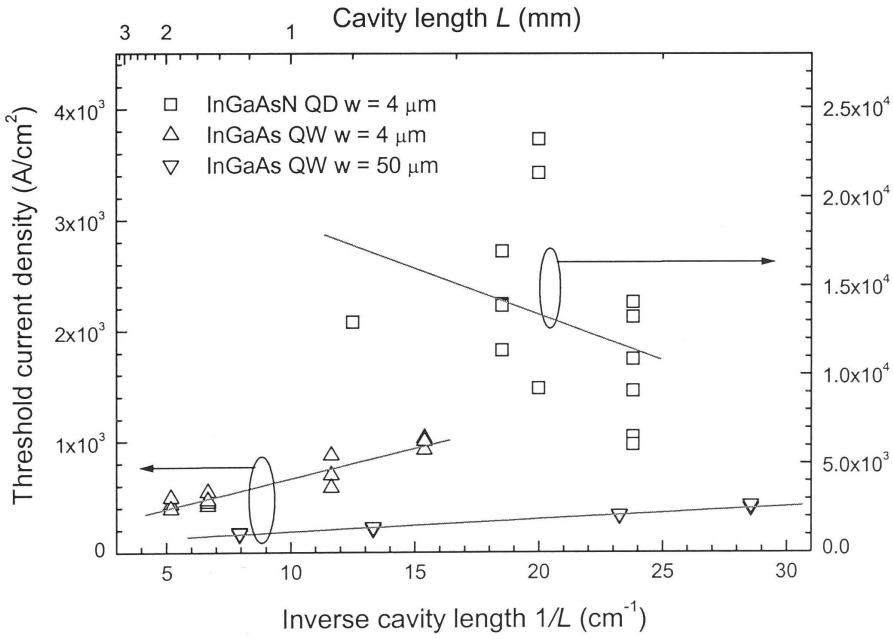

Fig. 7-7 The threshold current density (J_{th}) of the InGaAsN QD (square) and the InGaAs QW (up & down triangles) LDs as a function of inverse cavity length ($1/L$) at RT. The ridge width of the LDs w is shown in the legend. The lines are just a guide for eyes.

a GaAs/AlGaAs LD with cleaved facets, η_i and α_i can be deduced from the intercept and slope of the $1/\eta_d$ *vs* L plot, respectively. The $1/\eta_d$ *vs* L plots for InGaAs QW and InGaAsN QD LDs are shown in figures 7-8(a) and (b), respectively.

It can be seen from Fig. 7-7 that for the InGaAs QW LDs, J_{th} exhibits the normal decrease with increasing L due to the decrease of mirror losses and its value is as low as 166 A/cm^2 for long devices (1.26 mm) with a ridge width of 50 μm at RT. It is worth stressing here that J_{th} of the devices with a 4 μm ridge width is higher than that of the devices with a 50 μm ridge width by a factor of 2-3. This is because of the effects of the current spreading in the *p*-AlGaAs cladding layer under the ridge and the carrier diffusion in the active region. These effects are much more prominent in the 4 μm-ridge devices due to their relatively narrower ridge width than in the 50 μm-ridge devices where the measured J_{th} values can be taken as the real ones of these QW devices. Therefore, the real value of J_{th} for the 4 μm-ridge laser devices can be estimated by dividing the measured values by a correction factor of 2-3. Furthermore, the internal efficiency η_i of the QW LDs is nearly 100% [Fig. 7-8(a)], which means a negligible contribution of the nonradiative recombination in this QW laser structure.

However, for InGaAsN QD LDs, only short devices with L~ 0.4 - 0.8 mm lased at RT under the current injection (≤ 500 mA) used here, as seen in Fig. 7-7. Moreover, J_{th} increases rapidly with the cavity length L at RT instead of decreasing which is normally observed for the ridge-waveguide laser devices. These results strongly suggest the overwhelming influence of nonradiative recombinations in the QD structure, which are expected to increase with the device length. These nonradiative recombinations are most likely due to defects such as dislocations, which could be further evidenced by the low internal efficiency η_i ~75% [Fig. 7-8(b)]. The shorter the device is, the number of such defects is lower. Thus the devices lase at RT, even though J_{th} is very large, exceeding 5000 A/cm^2 for 0.4 - 0.8 mm long devices. The nonradiative recombinations will be strongly diminished at low temperature (e.g. 77 K), when carriers are localised in the QDs and their escape rate in the wetting layer or GaAs barrier layers is very low. It was indeed observed in the experiments, where J_{th} decreases considerably at 77 K, reaching values of 184 A/cm^2 for 1.36 mm long devices and 58.7 A/cm^2 for the 2.3 mm long devices (results are not shown). A similar temperature effect was also reported in Ref. 47 for the InGaAs QD lasers. Considering the correction factor of 2-3, it can be

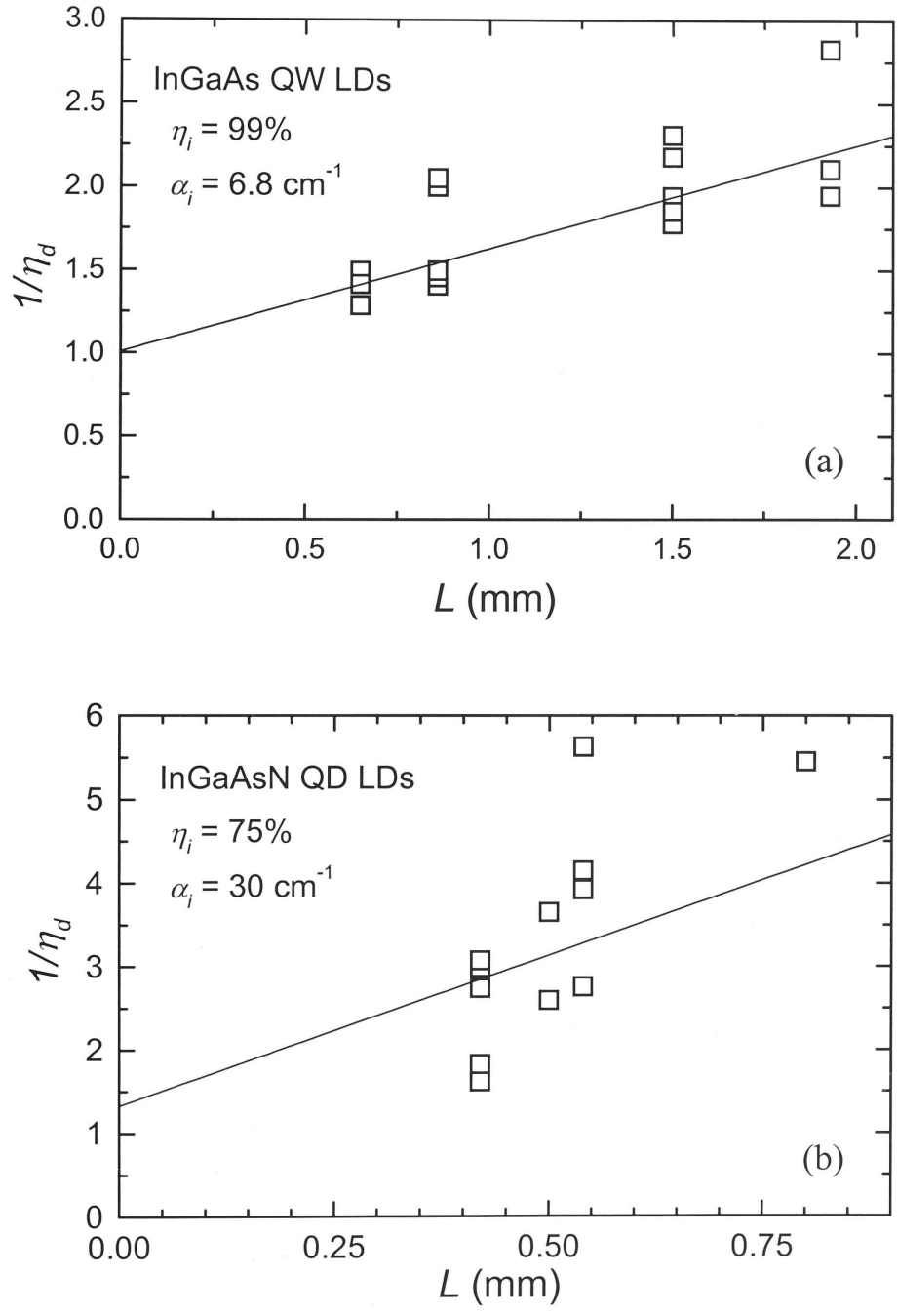

Fig. 7-8 Reciprocal external quantum efficiency ($1/\eta_d$) *vs* cavity length L for (a) the InGaAsN QD and (b) the InGaAs QW LDs. All devices have a ridge width of 4 μm. The solid line is the linear fit of the data.

estimated that the real value of J_{th} is about 23 A/cm^2 for a 2.3 mm long device at 77 K. This value is much lower than that of the In(Ga)As QD laser devices at their early stages,[23,45,48] indicating that the InGaAsN QDs are very promising for the long-wavelength semiconductor lasers.

Comparing the internal loss α_i between the QD and the QW LDs, it is clearly seen that α_i ~30 cm^{-1} for the QD LD is much higher than α_i ~7 cm^{-1} for the QW LD, presumably due to the optical scattering at the InGaAsN/GaAs interfaces, alloy fluctuations, and free carrier absorption in the GaAs or the wetting layers under high current injection, which are expected to be larger for a InGaAsN QD structure than for a InGaAs QW structure. It is also worth mentioning that the range of available cavity lengths for the InGaAsN QD devices is very narrow [see Fig. 7-8(a)], therefore, the extrapolative values of η_i and α_i can vary from the real values.

7.4 Conclusion

In summary, the InGaAsN QD and reference InGaAs QW laser devices were characterised by using absorption spectroscopy, electroluminescence spectra, and *L-I* curves. The photocurrent spectra measured with polarisation at 0 V external bias show that the dot transitions are clearly TE-polarised, which means these transitions are mainly involving the electronic levels and the heavy hole states. Moreover, the photocurrent peaks of the wetting layer in the InGaAsN QD structure show a blueshift and are broader compared with those of the reference InGaAs QW structure, due to the possible In segregation in the QDs and a QD-induced rougher interface between the wetting layer and the GaAs barriers, respectively. The QD transitions are suppressed at 77 K and can only be observed in the photocurrent spectra measured with external bias, which is because the predominant escape mechanism of the photoexcited carriers from the QD levels is tunnelling at 77 K. The quantum-confined Stark shift does not show an average built-in electric field in the InGaAsN QD laser structure, presumably due to the presence of N which influences the strain in the QDs such that the internal field is less than that in the typical InGaAs QD structures. It is also evident from the electroluminescence spectra as a function of injection current that the InGaAsN QD LDs lase at 1078 nm from the excited states of the QDs at RT. Comparing the absorp-

tion spectra measured by the multisection-device technique and the photocurrent, it is proposed that the photoexcited carriers in the multisection device modify the potential profile in the QDs such that the oscillator strength of the excited-state transitions increases compared with the ground-state transitions in the absorption spectrum, which also explain the fact that the InGaAsN QD LDs lase from the excited states. Finally, from the *L-I* curve characterisation, only the short InGaAsN QD LDs lased at RT. The dependency of J_{th} on L at RT strongly suggests the overwhelming influence of nonradiative recombinations in the QD structure. The threshold current density of the InGaAsN QD laser devices is estimated to be about 23 A/cm^2 for a 2.3 mm long device at 77 K. This value is much lower than that of the In(Ga)As QD laser devices at their early stages,[23,45,48] indicating that the InGaAsN QDs have a great potential for the long-wavelength semiconductor lasers.

Reference:

1 C. E. Zah, R. Bhat, B. N. Pathak, F. Favier, W. Lin, M. C. Wang, N. C. Andreadakis, D. M. Hwang, M. A. Loza, T. P. Lee, Z. Wang, D. Darby, and J. J. Hsieh, IEEE J. Quantum Electron. **30,** 511 (1994).

2 M. Kondow, K. Uomi, A. Niwa, T. Kitatani, S. Watahiki, and Y. Yazawa, Jpn. J. Appl. Phys., Part 1 **35,** 1273 (1996).

3 K. Chang Kyu and L. Yong Hee, Applied Physics Letters **79,** 3038 (2001).

4 C. Skierbiszewski, P. Perlin, P. Wisniewski, W. Knap, T. Suski, W. Walukiewicz, W. Shan, K. M. Yu, J. W. Ager, E. E. Haller, J. F. Geisz, and J. M. Olson, Appl. Phys. Lett. **76,** 2409 (2000).

5 T. Kitatani, K. Nakahara, M. Kondow, K. Uomi, and T. Tanaka, Jpn. J. Appl. Phys., Part 2 **39,** L86 (2000).

6 S. Sato and S. Satoh, IEEE Photonics Technol. Lett. **11,** 1560 (1999).

7 K. Yang, C. P. Hains, and J. L. Cheng, IEEE Photonics Technol. Lett. **12,** 7 (2000).

8 M. Kawaguchi, T. Miyamoto, E. Gouardes, D. Schlenker, T. Kondo, F. Koyama, and K. Iga, Jpn. J. Appl. Phys., Part 2 **40,** L744 (2001).

9 N. Tansu, A. Quandt, M. Kanskar, W. Mulhearn, and L. J. Mawst, Appl. Phys. Lett. **83,** 18 (2003).

10 N. Tansu, N. J. Kirsch, and L. J. Mawst, Appl. Phys. Lett. **81,** 2523 (2002).

11 F. Höhnsdorf, J. Koch, S. Leu, W. Stolz, B. Borchert, and M. Druminski, Electron. Lett. **35,** 571 (1999).

12 M. Fischer, M. Reinhardt, and A. Forchel, Electron. Lett. **36,** 1208 (2000).

13 W. Ha, V. Gambin, M. Wistey, S. Bank, K. Seongsin, and J. S. Harris, Jr., IEEE Photonics Technol. Lett. **14,** 591 (2002).

14 C. S. Peng, T. Jouhti, P. Laukkanen, E. M. Pavelescu, J. Konttinen, W. Li, and M. Pessa, IEEE Photonics Technol. Lett. **14,** 275 (2002).

15 J. A. Wei, F. N. Xia, C. Q. Li, and S. R. Forrest, IEEE Photonics Technol. Lett. **14,** 597 (2002).

16 M. Fischer, M. Reinhardt, and A. Forchel, IEEE Photonics Technol. Lett. **12,** 1313 (2000).

17 H. Riechert, A. Ramakrishnan, and G. Steinle, Semicond. Sci. Technol. **17,** 892 (2002).

18 Y. Arakawa and H. Sakaki, Appl. Phys. Lett. **40,** 939 (1982).

[19] M. Asada, M. Miyamoto, and Y. Suematsu, IEEE J. Quantum Electron. **22,** 1915 (1986).

[20] D. L. Huffaker, G. Park, Z. Zou, O. B. Shchekin, and D. G. Deppe, Appl. Phys. Lett. **73,** 2564 (1998).

[21] K. Mukai, Y. Nakata, K. Otsubo, M. Sugawara, N. Yokoyama, and H. Ishikawa, IEEE Photon. Technol. Lett. **11,** 1205 (1999).

[22] R. Sellin, C. Ribbat, M. Grundmann, N. N. Ledentsov, and D. Bimberg, Appl. Phys. Lett. **78,** 1207 (2001).

[23] N. Kirstaedter, O. G. Schmidt, N. N. Ledentsov, D. Bimberg, V. M. Ustinov, A. Y. Egorov, A. E. Zhukov, M. V. Maximov, P. S. Kop'ev, and Z. I. Alferov, Appl. Phys. Lett. **69,** 1226 (1996).

[24] O. B. Shchekin, J. Ahn, and D. G. Deppe, Electron. Lett. **38,** 712 (2002).

[25] S. Makino, T. Miyamoto, T. Kageyama, N. Nishiyama, F. Koyama, and K. Iga, J. Crystal Growth **221,** 561 (2000).

[26] M. Sopanen, H. P. Xin, and C. W. Tu, Appl. Phys. Lett. **76,** 994 (2000).

[27] K. C. Yew, S. F. Yoon, Z. Z. Sun, and S. Z. Wang, J. Crystal Growth **247,** 279 (2003).

[28] G. P. Agrawal and N. K. Dutta, *Semiconductor lasers*, 2nd Edition. (Kluwer Academic Publishers, Boston, 2000).

[29] L. A. Coldren and S. W. Corzine, *Diode Lasers and Photonic Integrated Circuits* (John Wiley & Sons, Inc., New York, 1995).

[30] H. C. Casey and M. B. Panish, *Heterostructure Lasers*, Vol. A and B (Academic Press, San Diego, 1978).

[31] H. D. Summers, J. D. Thomson, P. M. Smowton, P. Blood, and M. Hopkinson, Semicond. Sci. and Technol. **16,** 140 (2001).

[32] K. M. Groom, A. I. Tartakovskii, D. J. Mowbray, M. S. Skolnick, P. M. Smowton, M. Hopkinson, and G. Hill, Appl. Phys. Lett. **81** (2002).

[33] W.-H. Chang, T. M. Hsu, C. C. Huang, S. L. Hsu, C. Y. Lai, N. T. Yeh, T. E. Nee, and J.-I. Chyi, Phys. Rev. B **62,** 6959 (2000).

[34] P. W. Fry, I. E. Itskevich, S. R. Parnell, J. J. Finley, L. R. Wilson, K. L. Schumacher, D. J. Mowbray, M. S. Skolnick, M. Al-Khafaji, A. G. Cullis, M. Hopkinson, J. C. Clark, and G. Hill, Phys. Rev. B **62,** 16784 (2000).

[35] D. A. B. Miller, D. S. Chemla, T. C. Damen, A. C. Gossard, W. Wiegmann, T. H. Wood, and C. A. Burrus, Phys. Rev. B **32,** 1043 (1985).

[36] K. Yamanaka, T. Fukunaga, N. Tsukada, K. L. I. Kobayashi, and M. Ishij, Appl. Phys. Lett. **48,** 840 (1986).

[37] G. Bastard, E. E. Mendez, L. L. Chang, and L. Esaki, Phys. Rev. B **28,** 3241 (1983).

[38] P. W. Fry, I. E. Itskevich, D. J. Mowbray, M. S. Skolnick, J. J. Finley, J. A. Barker, E. P. O'Reilly, L. R. Wilson, I. A. Larkin, P. A. Maksym, M. Hopkinson, M. Al-Khafaji, J. P. R. David, A. G. Cullis, G. Hill, and J. C. Clark, Phys. Rev. Lett. **84,** 733 (2000).

[39] A. Passaseo, M. D. Vittorio, M. T. Todaro, I. Tarantini, M. de Giorgi, R. Cingolani, A. Taurino, M. Catalano, A. Fiore, A. Markus, J. X. Chen, C. Paranthoen, U. Oesterle, and M. Ilegems, Appl. Phys. Lett. **82,** 3632 (2003).

[40] W. Sheng and J.-P. Leburton, Phys. Rev. B **67,** 1253081 (2003).

[41] S. Raymond, J. P. Reynolds, J. L. Merz, S. Fafard, Y. Feng, and S. Charbonneau, Phys. Rev. B **58,** R13415 (1998).

[42] O. Wolst, M. Schardt, M. Kahl, S. Malzer, and G. H. Döhler, Physica E **13,** 283 (2002).

[43] W. Sheng and J.-P. Leburton, Appl. Phys. Lett. **80,** 2755 (2002).

[44] A. Vasanelli, R. Fereira, and G. Bastard, Phys. Rev. Lett. **89,** 2168041 (2002).

[45] K. Mukai, N. Ohtsuka, M. Sugawara, and S. Yamazaki, Jpn. J. Appl. Phys., Part 2 **33,** L1710 (1994).

[46] D. L. Huffaker, G. Park, Z. Zou, O. B. Shchekin, and D. G. Deppe, Appl. Phys. Lett. **73,** 2564 (1998).

[47] D. G. Deppe, D. L. Huffaker, S. Csutak, Z. Zou, G. Park, and O. B. Shchekin, IEEE J. Quantum Electron. **35,** 1238 (1999).

[48] N. Kirstaedter, N. N. Ledentsov, M. Grundmann, D. Bimberg, V. M. Ustinov, S. S. Ruvimov, M. V. Maximov, P. S. Kop'ev, Z. I. Alferov, U. Richter, P. Werner, U. Gosele, and J. Heydenreich, Electron. Lett. **30,** 1416–1418 (1994).

CHAPTER 8

Summary

This thesis has revealed many unusual properties of (In)GaAsN semiconductor alloys and successfully demonstrated the InGaAsN QD laser devices.

First, the epitaxial growth of various (In)GaAsN structures by MOCVD was systematically studied. Mass-transport limited and kinetically limited MOCVD growth regimes for GaAsN epilayers have been identified. The growth temperature and the fractional DMHy molar flow, DMHy/V, were identified as key factors controlling the N content in GaAsN. Precise control of N content in the range from 0.1% to 4.5% can be obtained by choosing an appropriate combination of growth temperature and DMHy/V. A kinetic growth model was proposed to explain the growth process of the GaAsN epilayers. It was found that growing GaAsN directly on AlGaAs has a negative effect on the crystalline quality of the GaAsN due to the direct reaction between Al and N. Insertion of three InAs monolayers in a single GaAsN/GaAs QW structure has significantly improved the PL efficiency and blueshifted the PL peak wavelength, most likely due to the strain compensation and/or In-induced reduction of N incorporation. The high quality InGaAsN QDs with a RTPL emission at 1.32 μm were successfully grown on GaAs by MOCVD.

The TRPL measurements have provided evidence that the nature of the low-temperature (10 K) radiative recombination in GaAsN systems is related to the recombination between *localised* electrons and *delocalised* holes. The optical/bandgap bowing coefficient of $GaAs_{1-x}N_x$ epilayers was found to strongly depend on the N content, x. It can be as high as ~58 eV for dilute concentrations ($x \sim 0.1\%$), and then decreases rapidly to a nearly constant value of ~15 eV for higher N concentrations ($x \geq 1.6\%$). Based on the temperature dependence of PL measurements, it was also revealed that low-temperature (10 K) PL peak emission from GaAsN epilayers is not solely due to the interband transition, but originates from a combination of several transitions involving localised defect/cluster states near the conduction band. These results also confirm a N-composition dependent conduction-band structure for GaAsN alloys. The structural studies of GaAsN epilayers have demonstrated that, when the thickness of GaAsN layers is above a critical value, microscopic cracks and dislocations begin to form on the sample's surface and at the GaAsN/GaAs interface, respectively. These structural inhomogeneities form efficient light scattering centres, resulting in random lasing emissions from the thick (≥ 500 nm) $GaAs_{0.972}N_{0.028}$ epilayers grown on GaAs.

The ion beam-induced damage buildup and amorphisation processes at LN_2 temperature were systematically studied for GaAsN epilayers of different N contents (0, 1%, and 2% N) by using 50 keV Si ions and RBS-channeling techniques. Results show that the GaAsN epilayer becomes easier to amorphise with increasing N content, presumably due to the accumulation of ion beam-induced defects in the strain field caused by N atoms. It was also demonstrated that growth temperature used in this study (550 - 630°C) and postgrowth annealing do not affect the damage buildup process, indicating grown-in defects in GaAsN epilayers do not play a major role in the amorphisation process. Unintentionally doped *p*-GaAsN epilayers grown by MOCVD with different N contents and intentionally Zn-doped *p*-GaAsN epilayers to different concentrations were used to study the formation of implant isolation for a wide range of ions. The results clearly demonstrated that the threshold fluence, F_{th}, for implant isolation in *p*-GaAsN epilayers depends close-to-linearly on the initial free hole concentration and inversely on the concentration of atomic displacements produced by the ion beams. Different to the damage buildup study, the N content does not affect the implant isolation process if GaAsN epilayers have same free carrier concentration. The isolation process was determined predominantly by the nuclear energy deposited in elastic recoils during implantation. This is evidenced by the similar activation energy for isolation obtained by H, C, and O ion implantation, and the similar thermal stability of isolation of *p*-GaAsN epilayers bombarded with different ions during post-implantation isochronal annealing. The evolution of defects created by the 2 MeV C ions with the fluence ϕ follows the steps: (i) point defects for $\phi \sim 0.25F_{th}$, (ii) defect pairs for $\phi \sim 1.1F_{th}$, and (iii) defect clusters or complexes (e.g., As_{Ga}) that are stable at 550°C for the higher ion fluences. The substrate temperature (-196–200°C) during implantation did not have any bearing on the isolation process, demonstrating that point-like defects do not contribute to the stability of implant isolation of *p*-GaAsN.

In addition to the extensive studies of GaAsN alloys, intermixing of the InGaAsN QD structure was investigated by means of deposition of thin dielectric films combined with RTA. The large thermal interdiffusion in InGaAsN QDs was effectively suppressed and controlled by deposition of thin TiO_2 layers with different thicknesses. The interdiffusion can also be enhanced by deposition of a thin SiO_2 layer combined with a high temperature (> 800 °C) rapid thermal annealing. The mechanism of the suppression effect from TiO_2 films on intermixing was proposed to be the tensile stress imposed by the TiO_2 layer on the sample during annealing. These methods have a sig-

nificant potential to realise the selective-area band-gap engineering for optoelectronic device integration.

Finally a thin *p*-cladding layer InGaAsN QD-based graded-index separate-confinement heterostructure (GRINSCH) was designed and fabricated into the ridge waveguide laser devices. The QD laser devices were characterised in detail by using absorption spectroscopy, electroluminescence spectra, and *L-I* curves. The photocurrent spectra clearly show that the dot transitions are TE-polarised. The photocurrent peaks of the wetting layer in the QD structure show a blueshift and are broader compared with those of the reference InGaAs QW structure, due to possible In segregation in the QDs and a QD-induced rougher interface between the wetting layer and the GaAs barriers, respectively. The quantum-confined Stark shift does not show a built-in electric field in the InGaAsN QD laser structure, presumably due to the presence of N which influences the strain in the QDs such that the internal field is less than that in the typical InGaAs QD structures. It is also evident that the lasing emissions at RT are from the excited states of the QDs. Comparing the absorption spectra measured by the multisection-device technique and the photocurrent, it is proposed that the photoexcited carriers in the multisection device modify the potential profile in the QDs such that the oscillator strength of the excited-state transitions increases compared with the ground-state transitions in the absorption spectrum, which also explain the fact that the InGaAsN QD laser devices lase from the excited states. The dependency of J_{th} on L at RT strongly suggests the overwhelming influence of nonradiative recombinations in the QD structure, which is also evidenced by the fact that only short QD devices lased at RT. The threshold current density of the InGaAsN QD laser devices is estimated at about 23 A/cm^2 for a 2.3 mm long device at 77 K, indicating that the InGaAsN QDs have a great potential for the long-wavelength semiconductor lasers.

The fundamental properties of GaAsN alloys and potential of InGaAsN QDs as active region in laser devices have been extensively explored in this thesis. Many novel aspects of GaAsN alloys have been elucidated or discovered, greatly expanding our knowledge of this alloy system. InGaAsN QDs have also been shown to be suitable for long-wavelength laser devices. Many intriguing features of these materials could be further investigated in view of fundamental studies and device applications. With further optimisation of the growth procedures, high-efficiency long-wavelength InGaAsN QD laser devices could be realised in the near future.

ERRATA

Page 4, 3rd paragraph, line 2: Add "**E_{CBM}+180 meV**" before "...above the conduction".

Page 6, on Fig. 1-3: "**E_+**" is the one above the red curve, and "**E_-**" is the one below the blue curve.

Page 22, section 2.3.4, line 5: Add "**of**" after "is a part...".

Page 27, on Fig. 2-7: Change "Dealy" in the centre of the diagram to "**Delay**".

Page 29, 2nd last line: Add "**it becomes**" after "is absorbed before...".

Page 35, last paragraph, line 3: Change "piezo" to "**piezoelectric transducer**".

Page 37, section (i) Photolithography, line 2: Delete "**of**" after "most important steps...".

Page 47, Fig. 3-4, caption: Add "**at 600°C**" after "GaAsN epilayers...".

Page 61, last paragraph, line 1: Add "**of**" after "the insertion...".

Page 62, section 3.5, 4th last line: Replace "than" with "**over**".

Page 66, 2nd paragraph, line 2: Change "lasers" to "**laser**".

Page 66, 2nd paragraph, last line : Add "**on**" after "then focused...".

Page 66, 4th paragraph, line 1: Change "folds" to "**fold**".

Page 73, 2nd paragraph, line 6: Add "in the work reported here" before "an enhancement ..."

Page 73, 2nd paragraph, 3rd last line: Change "on" to "**of**".

Page 73, 2nd paragraph, 2nd last line: Change "were" to "**was**".

Page 125, line 14: Replace "retain" with "**hence it retains**".

Page 134, 2nd line: Delete "**suppressed**".

Page 148, last paragraph, lines2 and 3: Swap "Fig. 7-4(a)" and "Fig. 7-4(b)".

Page 151, Fig. 7-5(b), legend: Change "El, 450 mA" to "**EL**, 450 mA".